공학박사 학위논문

Study on cavity engineered sapphire substrate for highly efficient GaN-based light-emitting diodes

고효율 GaN 기반 발광다이오드 제작을 위한 중공 구조가 제어된 사파이어 기판에 관한 연구

2018년 2월

서울대학교 대학원

재료공학부

장 정 환

Abstract

Study on cavity engineered sapphire substrate for highly efficient GaN-based light-emitting diodes

Jeonghwan Jang

Department of Materials Science and Engineering

College of Engineering

Seoul National University

The GaN-based white light-emitting diodes (LEDs) have attracted much attention as a substitute for conventional illumination such as incandescent light bulbs and fluorescence lamps because of its high efficiency and long life. However, rapid penetration of the LEDs into lighting market has been limited due to its high cost. A major drawback of epitaxial growth of the GaN layer is that native substrates are not yet available in large scale, so heteroepitaxy using sapphire substrate have been typical method for the epitaxial growth. The large differences in the lattice constant and thermal expansion coefficient between GaN and sapphire substrate cause high density of threading dislocations and severe wafer bow. In addition, total internal reflection of the emitted light due to the large difference in the refractive index between the GaN epitaxial layer and outside (air) is one of the factors that reduce light

extraction efficiency. To achieve the high efficiency and productivity for cost reduction of the GaN-based LEDs, these technical issues need to be resolved.

In this research, in order to overcome the problems, we proposed a growth scheme using cavity engineered sapphire substrate (CES) in which a two-dimensionally patterned cavities are arrayed on a sapphire substrate. Amorphous alumina film was deposited by atomic layer deposition on a photoresist patterned sapphire substrate, and subsequent high temperature annealing resulted in the formation of a cavity array surrounded by a crystallized sapphire shell by solid-phase epitaxy (SPE). It was confirmed that well-defined air-cavity array was successfully incorporated into the sapphire substrate. Also, the amorphous alumina layer was fully crystallized into single crystalline α-phase from the sapphire substrate, indicating that the CES can act as a substrate for the epitaxial growth of GaN.

In the growth scheme using the CES, the GaN layer is grown on the SPE α-Al_2O_3 layer and resultantly crystalline quality of the GaN layer could be dependent on the characteristics of the SPE α-Al_2O_3, which arouses the importance of the fundamental understanding on the SPE mechanism. Accordingly, we investigated the SPE of stripe-shaped cavity amorphous Al_2O_3 membrane structure on a sapphire substrate. TEM analysis revealed that the SPE process occurred through 2 stages of the phase transformation from amorphous to γ-Al_2O_3 and subsequently to α-Al_2O_3. During the phase transformation to γ-Al_2O_3, beside SPE at the interface between the amorphous alumina layer and sapphire substrate, nanocrystalline γ-Al_2O_3 was formed in the upper part of the membrane. However, during the SPE from γ-

to α-phase, random nucleation was not observed in our investigation condition, resulting that the whole alumina membrane was transformed into α-Al_2O_3 by SPE. During the phase transformations, volume of the alumina membrane was contracted by the density increase, which induces stresses and deflections in the Al_2O_3 membrane structure. Furthermore, the activation energies of the SPE procedure from amorphous to γ-phase and that from γ- to α-phase were obtained as 3.1 eV and 3.9 eV, respectively, by precise measurement of the SPE rate using TEM analysis.

In addition, SPE mechanism of the amorphous alumina into the intermediate γ-phase was investigated in detail by phase/orientation mapping using a scanning nanobeam diffraction technique of TEM. This evidently revealed presence of the two stacking-mismatched domains in the epitaxial γ-Al_2O_3 layer, which can be distinguishable only at the specific projecting direction. More importantly, distribution of the stacking-mismatched domains in the SPE γ-Al_2O_3 layer gives significant information for understanding the formation mechanism of the γ-Al_2O_3 domains.

The growth behavior of GaN on the CES was investigated. The GaN film was observed to fill the spaces between the cavities at the initial stage of growth and then grow laterally over the cavities, leading to a completely coalesced pit-free smooth surface. CL dark spot density was reduced from 1.9 $\times$ 10^8 cm^{-2} to 1.4 $\times$ 10^8 cm^{-2}, demonstrating that the threading dislocation density was reduced using the CES. Also, the incorporation of cavities was observed to significantly reduce the stress in the GaN film by ~30%. The output power of LED on CES at an input current of 20 mA was measured to

be 2.2 times higher than that on the planar sapphire substrate, indicating that the cavity pattern at the interface significantly enhanced the light extraction.

To suppress the undesired growth of GaN on the cavity pattern, we suggested growth of GaN layer on a partially crystallized CES (PCCES) in which only the planar region between the patterns was crystallized into single crystalline (0001) α-Al_2O_3 while the alumina shell surrounding the cavities consisted of nanocrystalline γ-Al_2O_3. Due to limited growth rate of nanocrystalline GaN islands on the nanocrystalline alumina shell, c-plane GaN from the planar region laterally overgrows the nanocrystalline GaN islands on cavity patterns without interrupting by them. By using the PCCES, threading dislocations in the GaN region above the cavity patterns was significantly reduced compared to that on the existing CES. As a result, reverse leakage current for the GaN Schottky diode on PCCES was reduced by one order of magnitude compared to that on the existing CES.

Key Words:

GaN, Solid-phase epitaxy, alumina, Sapphire substrate, Cavity, γ-Al_2O_3 domain, Metal-organic chemical vapor deposition (MOCVD), Light-emitting diodes (LEDs), Light extraction efficiency, Epitaxial lateral overgrowth, Threading dislocations, Wafer bow

Student Number: 2011-22871

Contents

List of Tables

List of Figures

Chapter 1. Introduction

1.1. GaN-based LEDs

The GaN-based white light-emitting diodes (LEDs) has attracted much attention as a substitute for conventional illumination such as incandescent light bulbs and fluorescence lamps because of its high efficiency and long life.[1, 2] However, the high cost of LEDs is still limits their rapid penetration into the lighting market. The growth of GaN-based epitaxial layers depends on the heteroepitaxy due to the unavailability of GaN substrate.[3] GaN-based epitaxial layers are typically grown on sapphire substrates. Figure 1.1 shows the schematic diagram of the conventional lateral type GaN-based LED structure on a sapphire substrate. For the LED structure, GaN-based epitaxial layers consisting of un-doped GaN, n-GaN, $In_xGa_{1-x}N$/GaN multi quantum well (MQW) structure, p-GaN were grown on a sapphire substrate. The n- and p-type GaN layers are generally doped with Si and Mg, respectively. Then, after mesa etching, metal pad and indium tin oxide layer are deposited as an electrode and transparent conductive layer on the top surface of the mesa.

In order to achieve high efficiency and cost reduction for the GaN-based LEDs, several technical issues, such as high threading dislocation density, low light extraction efficiency, and wafer bow, have to be resolved. As shown in Fig. 1.2, the large differences in the lattice constant between GaN materials and sapphire substrate cause high density of threading dislocations[4], which reduces internal quantum efficiency, the ratio of the emitted photons from the

active region to electrons injected into the LEDs. Also, the large difference in the refractive index between the GaN epitaxial layers and outside (air) is major factor reducing the light extraction efficiency (LEE).[6] The low internal quantum efficiency and light extraction efficiency reduces the external quantum efficiency of the LEDs, ratio of the number of useful light particles to the number of injected charge particles, which is defined as[7]

$$\eta_{ext} = \eta_{int}\eta_{extraction}$$

where the η_{int} and $\eta_{extraction}$ are internal quantum efficiency and light extraction efficiency, respectively. In addition, severe wafer bow makes the use of large wafer difficult, which is obstacle for the cost reduction. Therefore, for the improvement of efficiency and productivity as well as for cost reduction, such technical issues should be resolved.

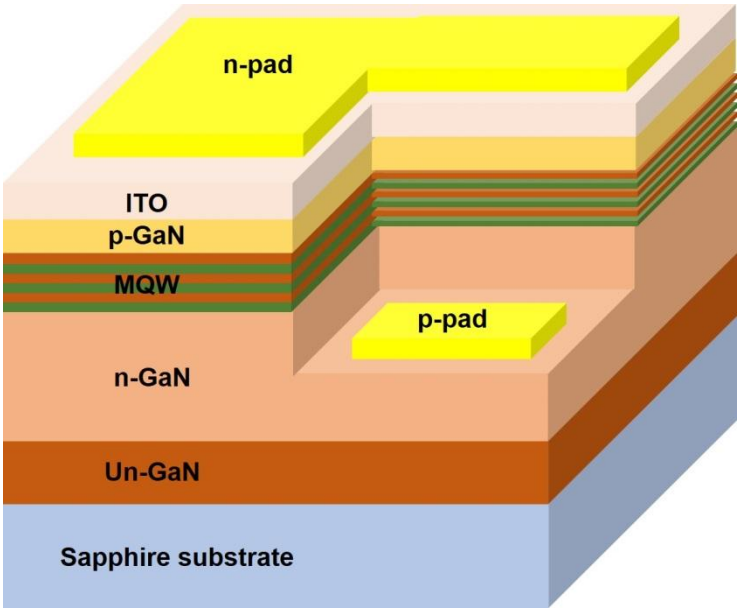

Figure 1.1 Schematic diagram of the conventional LED structure.

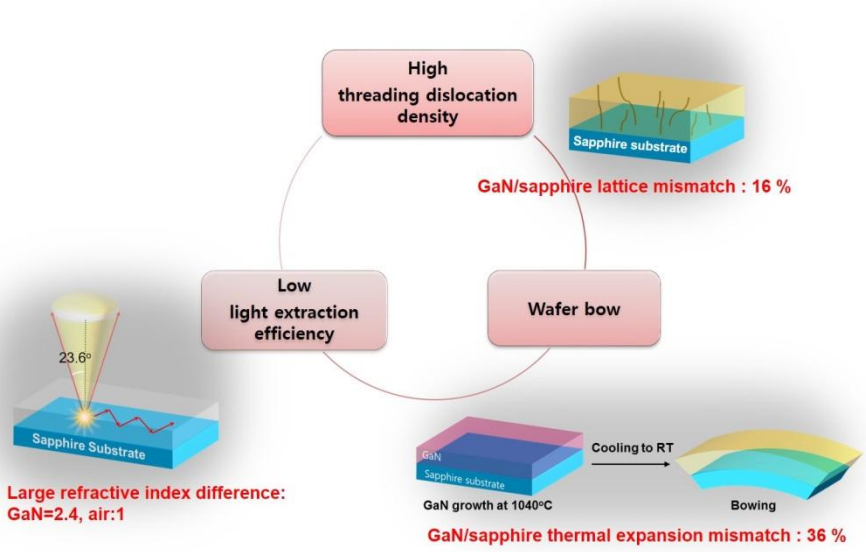

Figure 1.2 Schematic diagram of the technical issues in GaN-based LED.

1.2. Technical issues in GaN-based LEDs

1.2.1 High density of threading dislocations

As mentioned above, GaN epitaxial growth depends on a heteroepitaxy. In the heteroepitaxy, due to the lattice mismatch, the epitaxially grown layer is strained and the strain energy is accumulated until the critical thickness.[8] When the thickness of the strained layer is greater than the critical thickness, dislocations are generated leading to the relaxation of the epitaxial layer. For the GaN epitaxial layers, c-plane sapphire has been used as a substrate for the epitaxial growth and the large lattice mismatch between them generates the high density of threading dislocations in the epitaxial layer.[9] Figure 1.3 shows the epitaxial relationship between GaN and sapphire substrate when the c-plane GaN is grown on a c-plane sapphire substrate.[10] As shown in Table. 1.1, the in-plane lattice constants of the GaN and sapphire were 3.189 and 4.759 Å, respectively, resulting in the lattice mismatch of ~ 33 %. Fortunately, the GaN layer is grown on the sapphire substrate with mutual rotation by 30 ^{o} around the c-axis with epitaxial relationship of $[2\text{-}1\text{-}10]_{GaN}//[1\text{-}100]_{sapphire}$ and $[01\text{-}10]_{GaN}//[11\text{-}20]_{sapphire}$ and the lattice mismatch between the GaN and sapphire is reduced to 16 % as shown in Fig. 1.3. However, this is still large value for the epitaxial growth. Accordingly, there are numerous threading dislocations in GaN epitaxial layer on a sapphire substrate as shown in Fig. 1.4. The typical density of the threading dislocations in GaN layer is $10^{8} – 10^{10}$ cm^{-2}. The threading dislocations serve as a non-recombination center, reducing the internal quantum efficiency of the LED structure.[11] Therefore, growth of high quality GaN layer with low

threading dislocation density is required for the obtaining high efficiency LEDs.

1.2.2 Low light extraction efficiency

For the GaN-based LEDs, most of the emitted light from the active region is trapped inside the epitaxial layers due to high refractive index of the GaN materials. Light incident to the planar interface between air and the GaN experiences total internal reflection if the incident angle is larger than the critical angle as shown in the Fig. 1.5. The critical angle can be calculated as angle of the incidence when the refracted angle is 90 ^{o} by Snell's law, which is defined as

$$\frac{n_1}{n_2} = \frac{\sin\theta 2}{\sin\theta 1}$$

where n is refractive index and ϴ is measured angle from the normal of the interface in the respective medium. In the case of GaN, refractive index is 2.43 and resultant critical angle is calculated to be 24.3 ^{o}. Because the emitted light from the active layer is directionally isotropic, only a small fraction of the emitted light with the incident angle smaller than 24.3 ^{o} can be extracted out the LED structure. To calculate the fraction of extracted light, E. F. Schubert defines the escape cone using the critical angle as shown in the Fig. 1.6 (a)-(c).[6] The light incident into the cone can escape from the GaN LED

structure. Area of the escape cone was calculated by the surface area of the spherical cone with radius r as shown in the Fig 6 (b)-(c), which is given by

$$A = 2\pi r^2(1 - \cos\theta_c).$$

As a result, fraction of the light, which can be extracted, was calculated by

$$\frac{2\pi r^2(1 - \cos\theta_c)}{4\pi r^2} = \frac{1}{2}(1 - \cos\theta_c)$$

where the $4\pi r^2$ was the total surface area of the sphere with radius r. Following the equation, only 4.4 % of the generated light can be extracted out. This low light extraction efficiency (LEE) decreases the light output power of LEDs because the trapped light was reabsorbed by the substrate and the GaN epitaxial layers during the series of the total internal reflection. In order to increase the LEE, the trapped light should be redirected to be included in the escape cone.

1.2.3 Wafer bow

GaN epitaxial layers are generally grown by MOCVD at high temperature around 1000 ~ 1100 ^{o}C. During a cooling down process to room temperature after the growth, wafer bow occurs due to the large mismatch of thermal expansion coefficient between the GaN and sapphire as described in the Fig. 1.7. Because the in-plane thermal expansion coefficient of GaN is

smaller than that of the sapphire (Table. 2), the GaN film is under compression while the sapphire substrate is under tension after the cooling down. This results in a convex wafer to counteract the unbalanced elastic bending. The residual compressive stress in the thin film, σ_f, can be calculated measuring curvature of the wafer by Stoney formula[12],

$$\sigma_f = \frac{E_s h_s^2}{6(1-\nu_s)h_f}\kappa$$

where the E_s, h_s, and ν_s are elastic modulus, thickness and poison's ratio of substrate, respectively, h_f is thickness of the film, and κ is curvature of the wafer. The residual curvature is linearly proportional to the residual stress. Since the significant wafer bow after the GaN growth (which becomes even more severe for larger-area substrates), makes the subsequent chip processes such as photolithography difficult, the scale-up of substrates has been hindered. Therefore, reducing the residual compressive stress in the GaN film on sapphire substrate is essential to lower the wafer bow and consequently save the cost by using large-sized wafer.

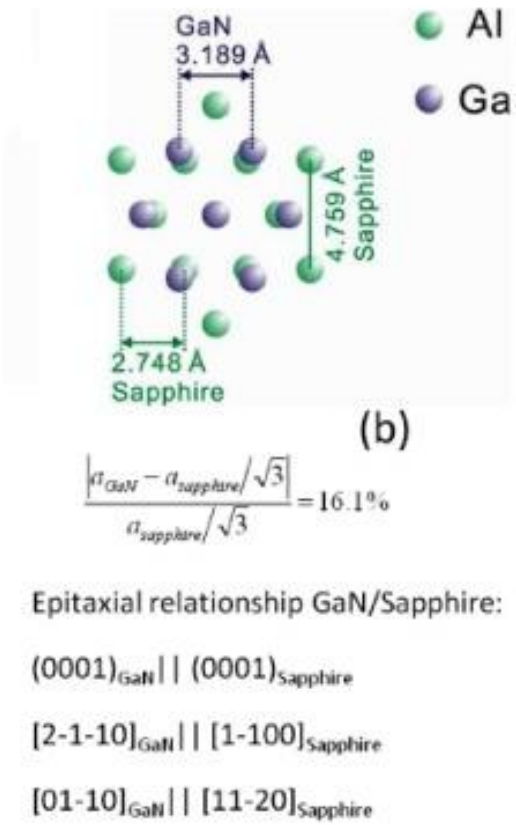

Figure 1.3 Lattice mismatch and epitaxial relationship between GaN and sapphire.[10]

Table 1.1 Lattice constant and thermal expansion coefficient of GaN and sapphire.[10]

		GaN	Sapphire
Lattice constant (Å)	a	3.19	4.76
	c	5.19	12.99
Thermal expansion coefficient (10^{-6} K^{-1})	a	5.59	7.3
	c	3.17	8.5

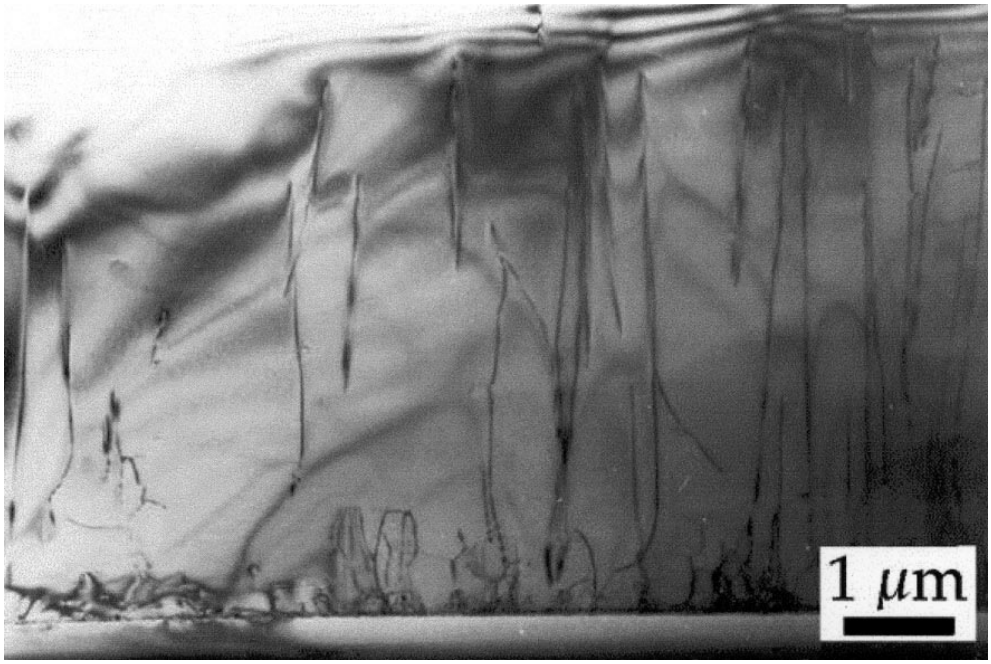

Figure 1.4 Cross-section TEM image of GaN epitaxial layer grown on a sapphire substrate by MOCVD.[11]

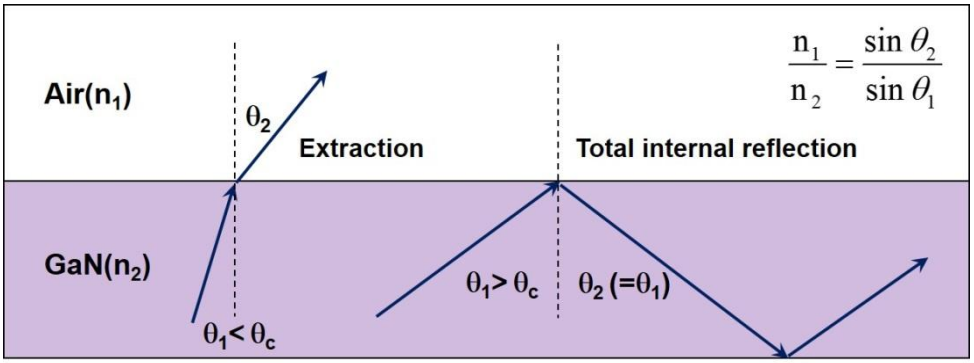

Figure 1.5 Schematic diagram of total internal reflection at the interface between GaN and sapphire.

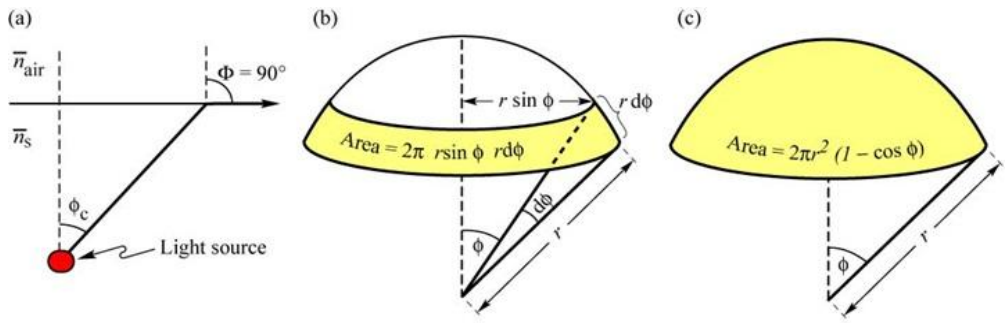

Figure 1.6 (a) Definition of the escape cone by the critical angle ϕ_c. (b) Area element dA. (c) Area of calotte-shaped section of the sphere defined by radius r and angle ϕ_c.[6]

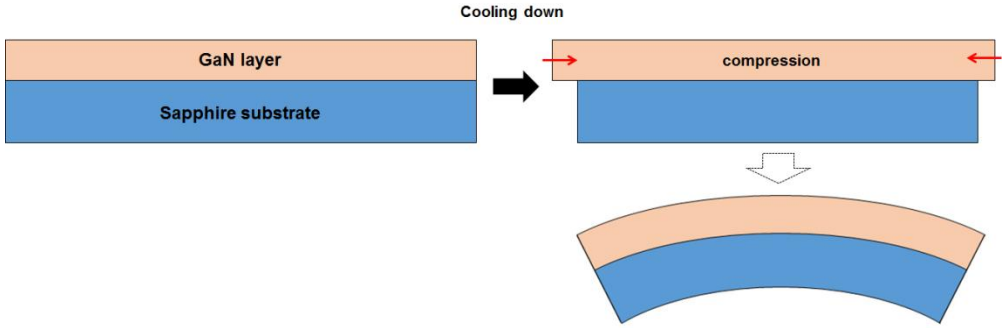

Figure 1.7 Schematic diagram of the wafer bow.

1.3. Patterned sapphire substrate

To enhance the external quantum efficiency (EQE) of GaN-based LEDs, various technical approaches have been reported: epitaxial lateral overgrowth[13, 14], patterned sapphire substrate (PSS)[15-19], photonic crystal[20, 21] surface texturing[22, 23], and embedded nano particles into GaN layers.[24, 25] Among them, growth scheme using the PSS has been an intriguing way in the LED industry for the manufacture of high-brightness LEDs due to the advantages in improving both crystal quality of the epitaxial layers and light extraction of LEDs. Figure 1.8 shows PSS with various shape of patterned sapphire such as cone, hemisphere, and pyramid.[26] For the fabrication of PSS, at first, photo resist (PR) pattern is formed on a sapphire substrate as an etching mask by a standard photolithography and subsequently reflow process is performed to modify the shape of PR pattern from cylinder to hemisphere or cone. The consequent sapphire pattern follows initial PR shape, i.e., cylindrical PR gives cylindrical shape of sapphire pattern. Since the cylinder type of pattern serves undesired growth template on the pattern surface and is disadvantageous in increasing the light extraction, the reflow process is required to make conical or hemispherical sapphire pattern. Finally, the PR patterned substrate is etched to pattern the sapphire surface. Dry etching using inductively coupled plasma reactive ion etching is common method for the PSS.

When the GaN epitaxial layer is grown on a PSS, the growth initiated selectively on a planar area between the patterns and then, the GaN from the planar area laterally overgrows the patterns, resulting in the reduction of threading dislocations[19] and resultant enhancement of internal quantum

efficiency. In addition, reflection and redirection of the emitted light at the pattern surface increases the possibility for the light to be incident within the escape cone, resulting in the enhancement of LEE. Therefore, GaN-based LEDs on PSS showed improved light output power compared to that on a planar sapphire substrate.[15-19]

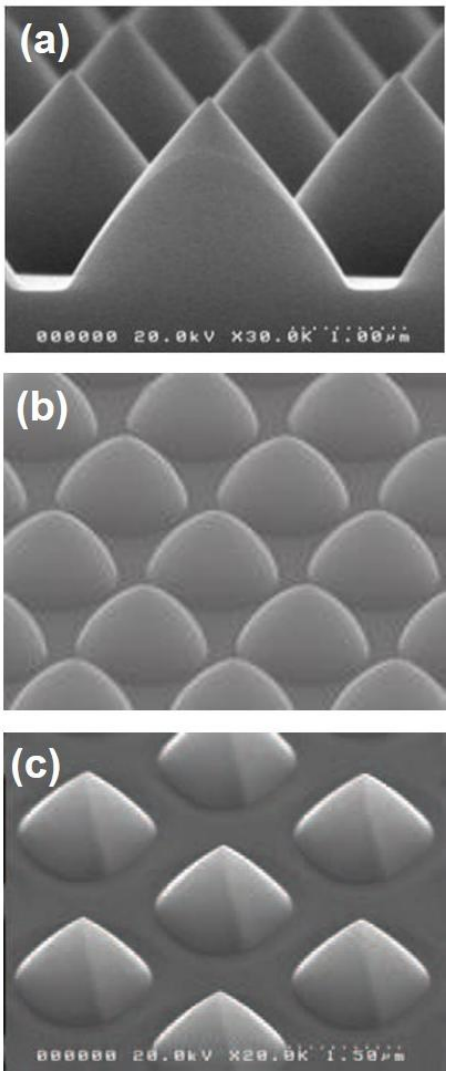

Figure 1.8 SEM images of (a) conical, (b) hemispherical, and (c) pyramidal PSS (Rubicon Technology, Inc.).

1.4. Cavity engineered sapphire substrate

For the fabrication of highly efficient LEDs, new growth scheme using a cavity engineered sapphire substrate (CES), in which a two-dimensionally patterned cavities are arrayed on a sapphire substrate, was proposed.[27, 28] Figure 1.10 (a) shows SEM image of the CES. In the growth scheme using the CES, well-defined air cavity array could be incorporated into the interface between the GaN and sapphire substrate without a regrowth step, which interrupts the growth and resultantly often leads to the degradation of the crystal quality of the GaN layer and LED characteristics. As in the case of PSS, threading dislocation density of GaN layer grown on the CES was reduced by epitaxial lateral overgrowth above the cavity patterns.[27] Also, it was demonstrated that strong diffraction of the emitted light at the high-index-contrast cavity patterns can greatly enhance the light extraction efficiency.[28] The LEDs fabricated on CES exhibited 9 % enhancement in the light output power at dominant wavelength of 462 nm compared to that on the PSS while preserving all of the electrical characteristic as shown in Fig. 1. 10 (b).[28] In addition, the existence of air voids inside the pattern was confirmed to reduce the wafer bow.[27]

To fabricate the CES, at first, PR pattern was formed on a sapphire substrate and then amorphous alumina (Al_2O_3) layer was deposited on the PR patterned substrate by atomic layer deposition. Subsequently, thermal treatment was performed to burn out the PR inside the alumina layer and crystallize the alumina layer into α-phase alumina from the sapphire substrate by solid-phase epitaxy (SPE). As shown in Fig. 1.11, the scheme includes

formation of amorphous alumina cavity structure on a sapphire substrate and subsequent crystallization of it to be served as a growth template. The crystallization is critical step in the fabrication process because the growth of GaN layer and its resultant crystalline quality could be dependent on the characteristics of the SPE α-Al_2O_3 layer. Accordingly, understanding the solid-phase transformation of the Al_2O_3 cavity structure is crucible to the quality improvement of the GaN layers. The solid-phase crystallization of the amorphous alumina cavity structure as well as fabrication process of CES and its application to LEDs are described in detail in this thesis.

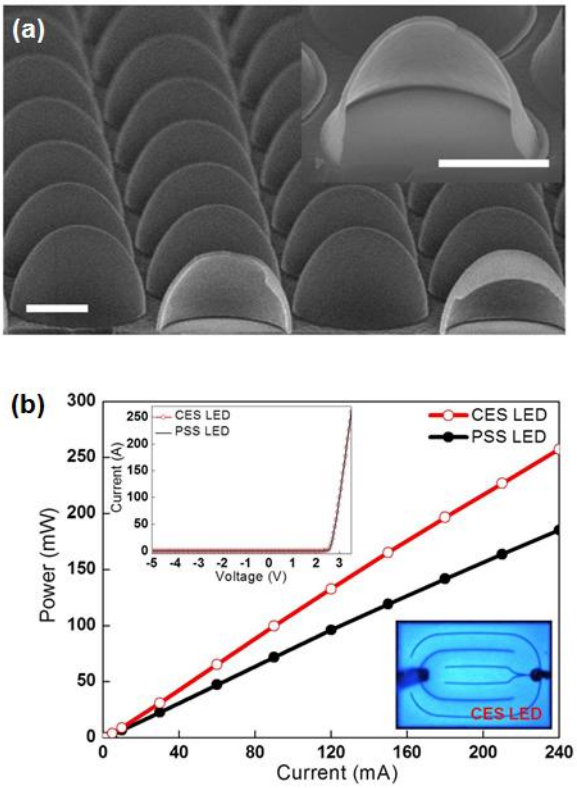

Figure 1.9 (a) SEM image of the CES. (b) Light output power of the LEDs on CES and PSS with current injection. Inset shows I-V characteristics of the LEDs.[28]

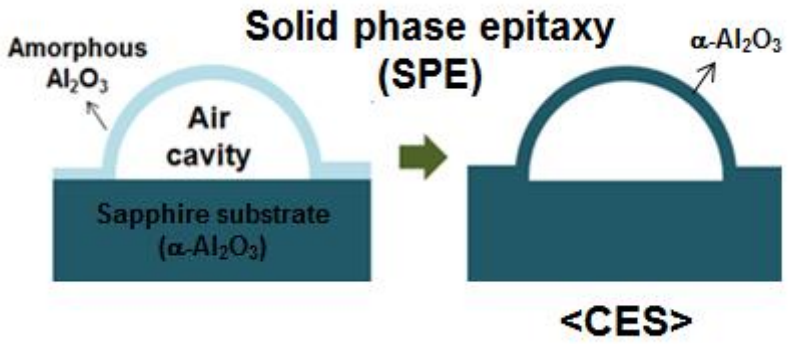

Figure 1.10 Schematic diagram for the fabrication process of the CES.

1.5. Solid-phase crystallization

1.5.1 Thermodynamics and kinetics of solid-phase crystallization

The driving force of the solid-phase crystallization (SPC) is free energy difference between the amorphous and crystalline phases. Figure 1.12 shows the free energy of amorphous Si and liquid Si relative to crystalline Si.[29] Due to the bond angle distortion required to accommodate the disordered atom rearrangement in the amorphous phase, the free energy of the crystalline phase is lower than that of the amorphous phase.[29] As a result, an amorphous solid has always driving force for rearrangement of its atomic position to the crystalline phase. Because of the free energy difference, an isolated piece of an amorphous material would eventually become crystalline phase even at room temperature. However, the kinetics determines how fast the crystallization will occur, i.e., the crystallization process become faster with raising the temperature. Kinetics of the solid-phase crystallization process is well describe by Arrhenius equation,

$$\mathrm{k} = \mathrm{A}\exp(-\frac{E_a}{kT})$$

where k is rate of a transformation, A is pre-exponential factor, and E_a is activation energy for the transformation. Activation energy means the minimum energy that must be required to start a transformation as described in Fig. 1.13(a). Thus, the activation energy is related with the rate limiting process of a transformation. When an amorphous phase transforms into a

stable phase through intermediate metastable phase, such as in the case of alumina, the SPC proceeds in several stages with different activation energies as shown in Fig. 1.13(b).

1.5.2 Random nucleation vs. solid-phase epitaxy

The SPC could be divided into two types of transformation, random nucleation and growth (RNG) and solid phase epitaxy (SPE).[29] The RNG consists of nucleation of clusters and their growth into crystallites, resulting in the formation of polycrystalline phase. Formation of an ordered cluster of atoms lowers the bulk free energy but this also accompanies generation of surface energy and strain energy, resulting in the increase of total free energy.[30] Therefore, the net free energy change of the process is given by

$$\Delta \mathrm{G} = -\mathrm{V}\Delta G_v + A\gamma + V\Delta G_s$$

where the V and A is volume and surface area of cluster, ΔG_v is Gibbs-free-energy change between the amorphous phase and crystalline phase per unit volume, γ is interface energy per unit area, and ΔG_s is strain energy per unit volume related to the phase transition.[30] During thermal fluctuation, some clusters become large enough for the bulk free energy to exceed the extra increase of free energy (surface and strain energy) when one more atom is added to them and they grow larger as described in Fig. 1.14(a).[29] This process leads to a progressive transformation of amorphous material into polycrystalline phase. The nucleation rate and growth rate are as follows,[31, 32]

$$\mathrm{N} \propto (\frac{1}{\mathrm{T}})\exp(-\frac{E_d + \Delta G^*}{kT})$$

$$v_g \propto \exp(-\frac{E_d + \frac{\Delta G}{2}}{kT})$$

where the T is annealing temperature, E_d is activation energy of self-diffusion in amorphous material, ΔG^* is the maximum free energy of a formation, and ΔG is net free energy during the growth. The nucleation rate was not a Arrhenius form where slope of the growth rate, $\frac{dln(N)}{d(\frac{1}{kT})}$, has kT term.[31] However, in the annealing temperature range of SPC, kT value varies only slightly.[31] So, for the nucleation rate, Arrhenius form could be taken to be $N_0\exp(-\frac{E_g}{kT})$ where the E_g is the slope of the Arrhenius plot for nucleation rate.

In contrast to the RNG, SPE process occurs when an amorphous thin film is direct contact with a single crystalline template, which makes the amorphous thin film be directly converted into single crystal.[29] As shown in Fig. 1.14 (b), the crystalline substrate provides a template for ordered crystallization of the amorphous thin film. The SPE process occurs by epitaxial layer-by-layer conversion of the atoms at the interface between amorphous film and crystalline substrate. Kinetics of SPE is well described by the Arrhenius equation.[29] Kinetics in the SPE process may be very similar with the growth process of RNG in which atoms are rearranged at the preceding crystallites. Rate of SPE process is much faster than that of RNG

and resultantly it is observed in lower temperature range.[29] This is because during the SPE process the atomic rearrangement at the interface will not significantly change the surface energy and strain energy, resulting in lower activation energy than the nucleation process.

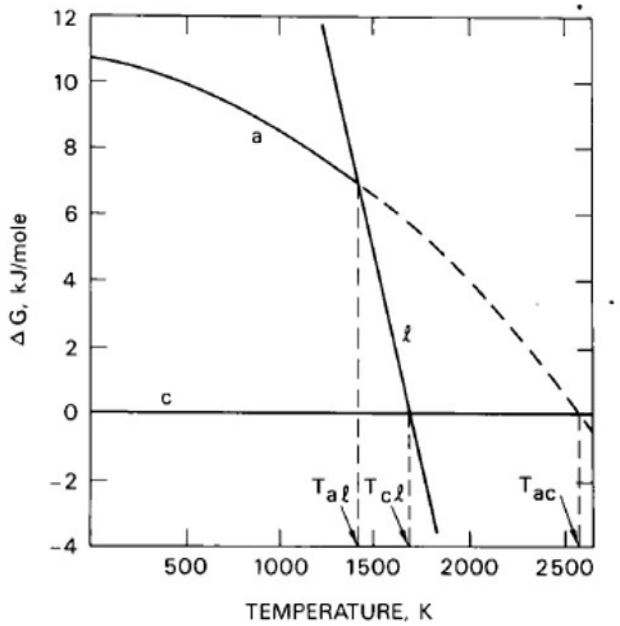

Figure 1.11 Free energy of amorphous and liquid Si relative to crystalline Si.[10]

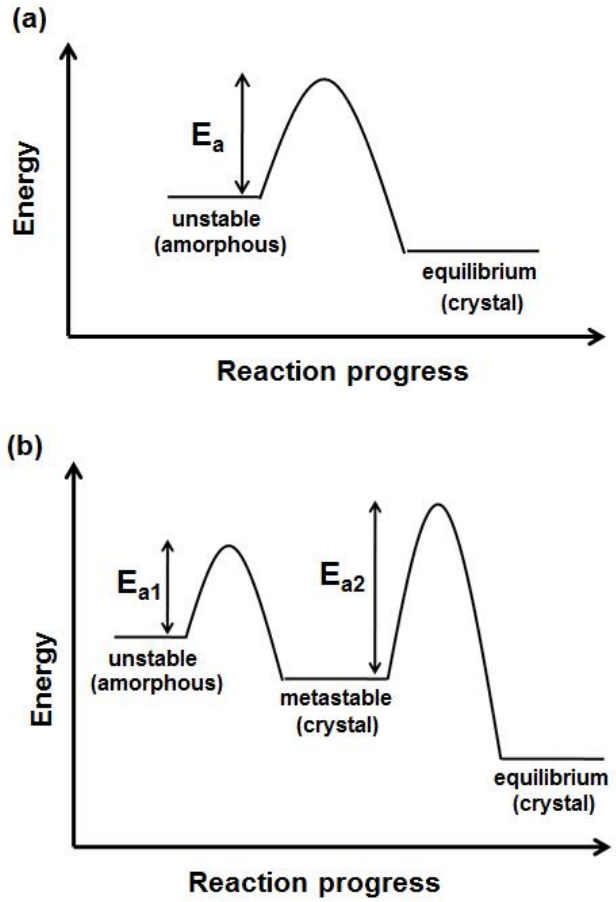

Figure 1.12 Schematic diagram of the energy state with the single reaction progress from amorphous to crystal and reaction progress with intermediate metastable phases.

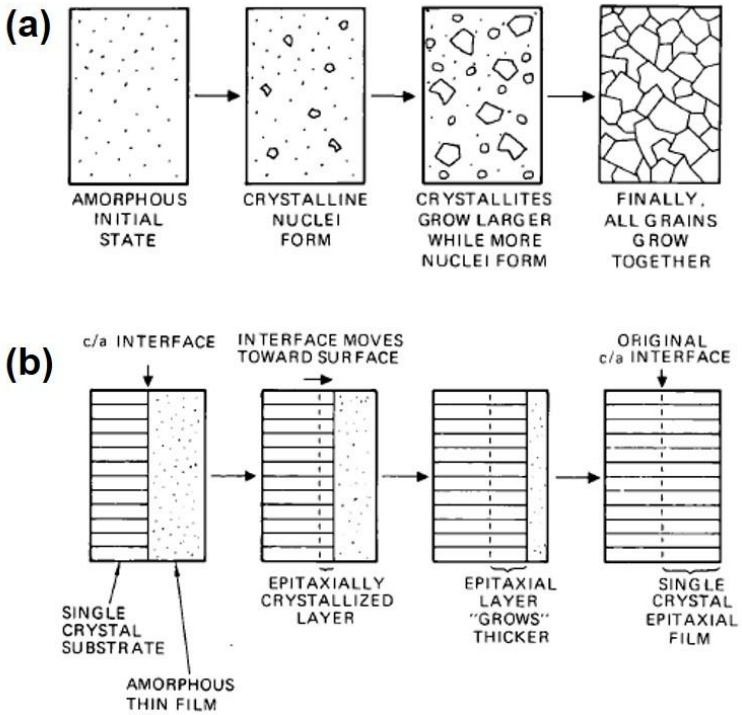

Figure 1.13 Schematic diagram of (a) the random nucleation and growth and (b) solid phase epitaxy.[10]

1.6. Sold-phase epitaxy in amorphous Al_2O_3 thin film

1.6.1 Crystal structure of α- and γ-Al_2O_3

In Al-O system, α-Al_2O_3 is the only stable form of crystalline phase as shown in Fig. 1.15.[33] Other meta-stable phase, such as γ-, δ-, θ-, κ-, χ-Al_2O_3, can be observed in the course of a crystallization. During a sufficient annealing, amorphous alumina will be finally transformed into α-Al_2O_3. It is known that the SPC of alumina proceeds in two stages from amorphous to metastable phase of γ-Al_2O_3 and then, subsequently into α-Al_2O_3.[34-42] Thus, it is necessary to understand the crystal structures of α- and γ-Al_2O_3 in order to study the SPC of amorphous alumina.

Figure 1. 16 (a) shows atomic structure of α-Al_2O_3 unit cell, which was made based on crystal structure database (ICDD-00-046-1212 (2012)). As shown in the atomic projection of the α-Al_2O_3 along $[10\text{-}10]_\alpha$ (Fig. 1.16 (b)), oxygen ions oxygen ions have ABABAB··· stacking sequences of hexagonal close-packed structure along {0006} planes while every aluminum ion occupies the octahedral positions regularly in the α-Al_2O_3 phase.[43] Figure 1.16 (c) shows occupancy of Al ions in the octahedral interstitial sites of the two adjacent close-packed oxygen layers. The 2/3 of the octahedral positions are occupied by Al ions and there are the three different kinds of possible Al positions along the $[0001]_\alpha$. According to the two kinds of oxygen stacking positions and three kinds of the Al positions, six pairs of O-Al layers constitute the one unit cell of α-Al_2O_3.

In contrast to the α-Al_2O_3, Atomic structure of the γ-Al_2O_3 is called a

defective cubic spinel structure; oxygen ions are face-centered cubic (FCC) structure as an ABCABC··· stacking sequences along {222} planes while aluminum ions partially occupy tetrahedral or octahedral positions in the oxygen framework of the cubic spinel structure satisfying the stoichiometry.[44] To fulfill stoichiometry, each unit cell contains 32 O and 64/3 Al. Figure 1.17 (a) and (b) show atomic structure of γ-Al_2O_3 unit cell and its projection along the $[110]_\gamma$, respectively, which was made based on crystal structure database (ICSD-66559). Alternately, one aluminum-ion layer is located only at the octahedral interstitial sites and the next layer is located at both the octahedral and tetrahedral interstitial sites along the (2-22) planes of oxygen ion. However, the exact locations of the Al ion are still controversial. In Fig. 1.17 (a) and (b), fraction of the darker area of the Al position indicates the occupancy.

1.6.2 SPE process in amorphous Al_2O_3 thin film

For the alumina, there have been several investigations on their SPE behavior using amorphous Al_2O_3 layer formed by ion-implantation and e-beam evaporation.[37-42] It has been reported that SPE of the amorphous Al_2O_3 layer occurs in two-step phase transformation from amorphous to metastable γ-phase and then subsequently to α-phase. Figure 1. 18 (a) shows schematic diagram for the SPE procedure in amorphous alumina thin film. Due to kinetics difference, phase transformation into γ-phase occurs first and then, subsequent phase transformation into α-phase proceeds from the interface

between the substrate and preceding γ-Al_2O_3. Figure 1.18 (b) shows results of TEM investigation on an alumina specimen in which the SPE from γ- to α-phase are partially proceeded, indicating that the growth of α-Al_2O_3 was proceeding through the γ-Al_2O_3. It was reported that during the SPE of amorphous alumina on a c-plane sapphire substrate (α-Al_2O_3), epitaxial relationship between γ- and α-Al_2O_3 was confirmed to be $\{111\}_\gamma//\{0001\}_\alpha$, $<110>_\gamma//<10\text{-}10>_\alpha$, and $<112>_\gamma//<1\text{-}210>_\alpha$.[37, 38] During the epitaxial growth of γ-Al_2O_3 on a c-plane sapphire substrate, the both oxygen ions in $\{111\}_\gamma$ and $\{0001\}_\alpha$ are close-packed but their stacking sequence along the growth planes is different from each other as shown in Fig. 1.16 and Fig. 1.17; ABABAB for α-Al_2O_3 and ABCABC for γ-Al_2O_3. The reported lattice mismatch between the γ- and α-Al_2O_3 is less than 2 %.[45, 46]

1.6.3 Kinetics of SPE in amorphous Al_2O_3 thin film

Studies on the kinetics of the SPE process in alumina has been reported for amorphous alumina thin films formed by ion-implantation and e-beam evaporation.[37-42] White et al. reported the kinetics of the γ → α phase transition for the amorphous alumina thin film, made by ion implantation, using Rutherford backscattering and transmission electron microscope (TEM).[37] For the amorphous alumina thin film formed by ion implantation, P. S. Sklad et al. investigated kinetics of the amorphous → γ phase transition using in situ TEM measurement, showing two different activation energies

for the process.[38] The kinetics of the SPE process has been also studied using time resolved reflectivity measurement for amorphous alumina film formed by ion implantation[39] and e-beam evaporation.[40-42] It was found that SPE of the amorphous Al_2O_3 layer occurs in two-step phase transformation from amorphous to metastable γ-phase (above 700 ^oC) and then subsequently to α-phase (above 800 ^oC) during high temperature annealing, due to the much faster growth rate of the phase transformation from amorphous to γ-Al_2O_3 than γ- to α- Al_2O_3.[37-42] Figure 1.19 shows Arrhenius plot for the SPE of amorphous alumina thin film formed by e-evaporation, which was reported by T. W. Simpson et al.[41] The SPE rate of the both phase transformation sequences are well described by the Arrhenius plot and the activation energies obtained by fitting from Arrhenius equation indicate that the phase transition from amorphous to γ-phase, which shows faster growth rate, has lower activation barrier than that from the γ- to α-phase transformation. However, the research groups that studied the kinetics of SPE of alumina have reported different activation energy for the SPE process as shown in Table. 1. However, the reason for their different activation energy was not revealed. The properties of amorphous alumina with deposition method as well as measurement tools for the SPE rate may influence on the activation energy value.

In addition, effect of substrate orientations and dopants on the SPE kinetics has been also reported. T. W. Simpson et al. reported that the SPE rate on the r-plane sapphire was faster than that on the c-plane and a-plane sapphire substrate as shown in Fig. 1.19. However, the SPE sequence was same for all of the difference sapphire surfaces. Also, the activation energy was not

changed with the crystallographic orientations, indicating that the rate limiting process is independent on the surface planes of sapphire substrate. They suggested that the different growth rate with orientation was due to the difference in ledge and step mobilities on the individual surfaces.[41] N. Yu et al. reported effect of doping on the kinetics of the SPE of amorphous alumina.[42] The transformation sequence of the doped sample was same with the undoped one. Also, the activation energy of the SPE from γ- to α-phase was not influenced by the presence of dopants. However, the existent of dopants affects the overall transformation rate; Fe enhances while Cr slows the growth rate relative to the undoped sample.[42]

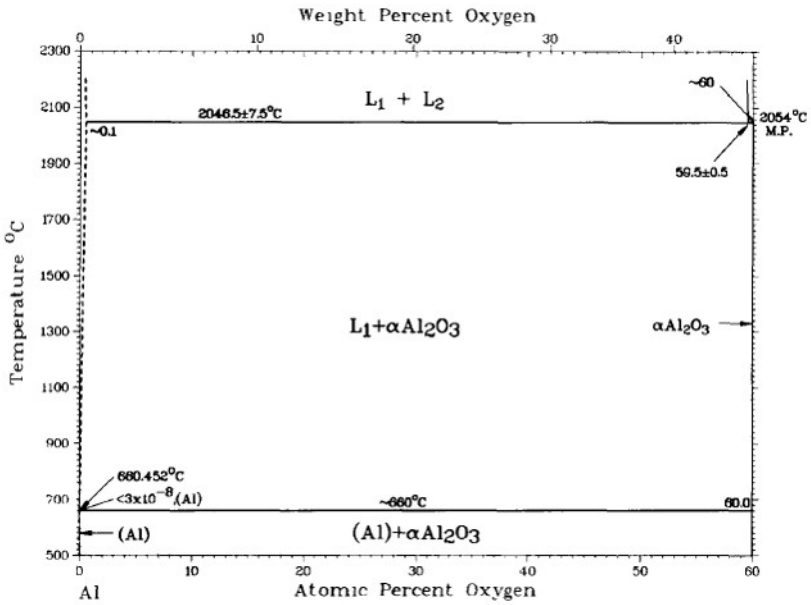

Figure 1.14 Phase diagram of the Al-O system.[15]

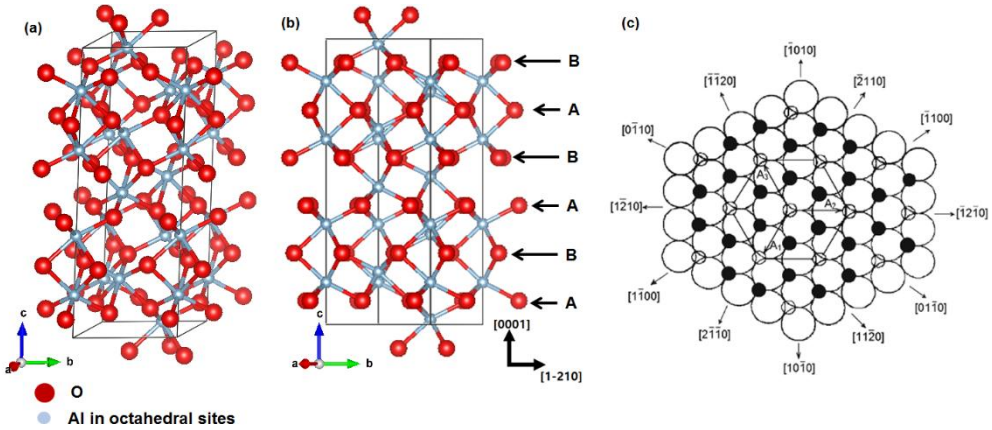

Figure 1.15 (a) Atomic structure of the α-Al_2O_3 unit cell. (b) Atomic projection of the α-Al_2O_3 along $[10\text{-}10]_\alpha$. (c) Schematic for Al ion position on the close-packed O layer in α-Al_2O_3.[ref] White large circle indicates oxygen ion and white and black small circle indicate vacant and occupied Al position, respectively.

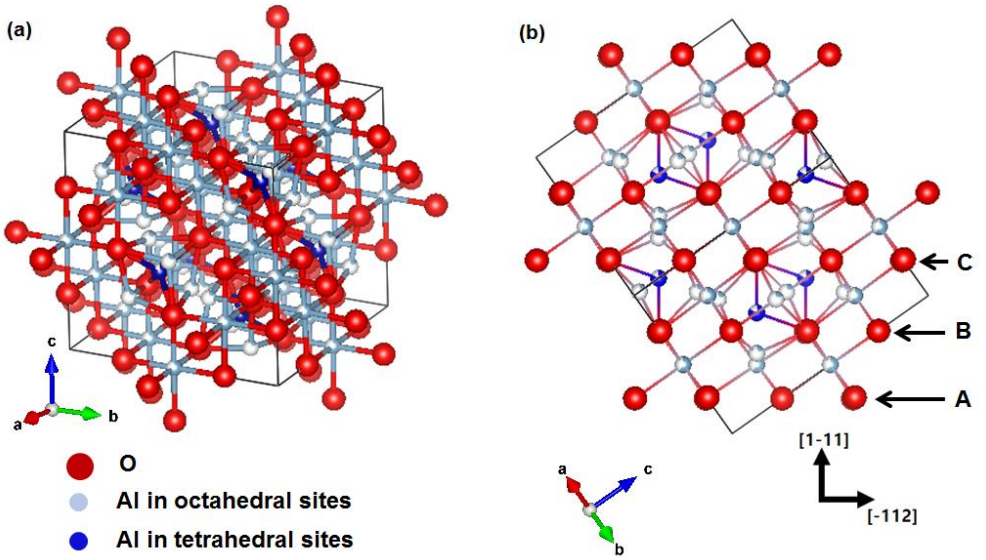

Figure 1.16 (a) Atomic structure of the γ-Al_2O_3 unit cell. (b) Atomic projection of the γ-Al_2O_3 along $[110]_\gamma$.

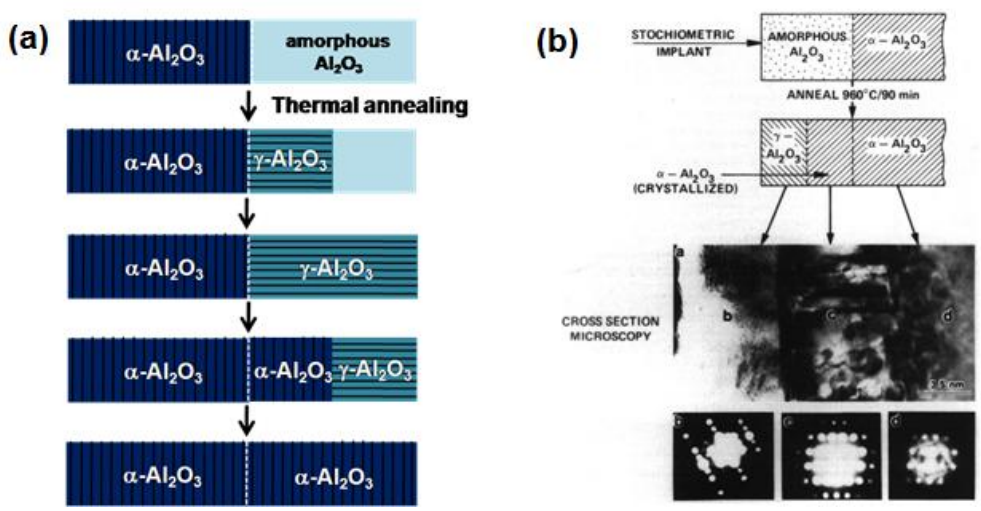

Figure 1.17 (a) Schematic diagram for the SPE procedure of alumina. (b) Result of TEM investigation on partially crystallized alumina thin film into α-phase on a sapphire substrate.

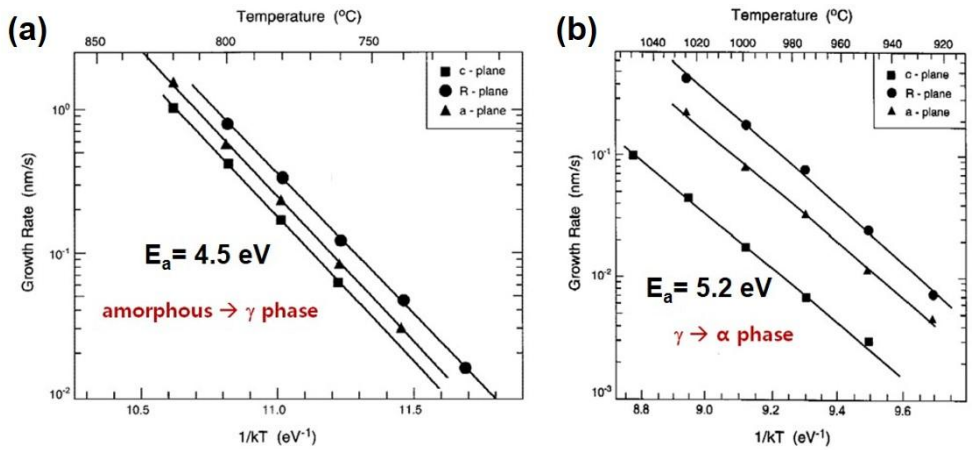

Figure 1.18 Arrhenius plot for the SPE of amorphous alumina thin film (a) from amorphous to γ-phase and (b) from γ- to α-phase.[41]

Table 1.2 Deposition method of amorphous alumina, analysis tools, and activation energies for the SPE process of amorphous alumina thin film.[37-42]

Author	Deposition method (thickness)	Analysis tool	Activation energy	year
C.W. White et al.	Ion implantion (160 nm)	TEM, RBS	E_a: 3.6 eV (g→a)	1988
P.S SKLAD et al.	Ion Implanation (170 nm)	In situ TEM	E_a: 7.8 eV, 1.6 eV (a→g)	1990
J.C Mc Callum et al.	Ion Implanation (200 nm)	TRR	E_a: 3.6 eV (a→g), 5.2±0.3 eV (g→a)	1994
Ning Yu et al.	e-beam evaporation (200 nm)	TRR	E_a: 5.0±0.2 (g→a)	1995
T. W. Simpson et al.	e-beam evaporation (400 nm)	TRR	E_a: 4.5 eV(a→g), 5.2 eV(g→a)	1998

RBS: Rutherford backscattering, TRR: Time resolved reflectivity

1.7. Thesis contents and organization

In this thesis, a new growth scheme of GaN layer using cavity engineered sapphire substrate (CES), in which cavity patterns were arrayed on a sapphire substrate, was studied for the highly efficient and less strained GaN-based LEDs. Incorporation of air-cavity patterns into interface between GaN and sapphire was achieved by growing the GaN layer on the CES. This scheme enables us to obtain enhanced light extraction efficiency, reduced threading dislocation density, and relaxed compressive stress in GaN layer. This thesis consists of the experimental results and discussions about the study on the CES and its application to GaN-based LEDs.

In chapter 2, fabrication procedure of the CES is described. Amorphous alumina film was deposited by atomic layer deposition on a photoresist patterned sapphire substrate, and subsequent high temperature annealing resulted in the formation of a cavity array surrounded by a crystallized sapphire shell. We successfully obtained well-defined alumina cavity array on a sapphire substrate.

In chapter 3, solid-phase epitaxy (SPE) of 3-dimensional alumina membrane structure, which is critical process for fabrication of the CES, is investigated in detail by TEM analysis. The unique SPE behaviors of the 3-D stripe-shaped alumina membrane, originated from its geometrical structure, are described. In addition, kinetics of the SPE procedure is investigated by precise measurement of the SPE rate in the TEM images.

In chapter 4, SPE mechanism of the amorphous alumina into the intermediate γ-phase is investigated in detail by phase/orientation mapping using a scanning nanobeam diffraction technique of TEM. This clearly

reveals presence of the two stacking-mismatched γ-Al_2O_3 domains in the SPE Al_2O_3, which can be distinguishable only at the specific projecting direction. More importantly, distribution of the stacking-mismatched domains in the SPE γ-Al_2O_3 layer gives significant information for understanding the formation mechanism of the γ-Al_2O_3 domains. Discussion on the formation mechanism of the γ-Al_2O_3 domain structure is described.

In chapter 5, GaN growth and characteristics of GaN-based LEDs on the CES is investigated. It is found that threading dislocation density and residual compressive stress was reduced in the GaN layer grown on CES compared to that on the planar sapphire substrate. Also, the output power of a LED on CES at an input current of 20 mA was measured to be 2.2 times higher than that on a planar sapphire substrate.

In chapter 6, growth of GaN layer on a partially crystallized CES (PCCES) is suggested to further improve the crystal quality of the GaN layer on the CES. Only the planar region between the patterns serves growth template of c-plane sapphire and the alumina cavity shell consists of nanocrystalline γ- Al_2O_3, resulting in the suppression of parasitic GaN growth on the pattern surface, which generates the additional threading dislocations during the merging process. Growth behavior and characteristics of the GaN layer on the PCCES is discussed in detail compared to that on the existing CES.

1.8. Bibliography

1. E. F. Schubert and J. K. Kim, Solid-State Light Sources Getting Smart, SCIENCE **308**, 1274 - 1278 (2005)

2. Siddha Pimputkar, James S. Speck, Steven P. DenBaars and Shuji Nakamura, Prospects for LED lighting, nature photonics **3**, 180-182 (2009)

3. K. Motoki, T. Okahisa, N. Matsumoto, M. Matsushima, H. Kimura, H. Kasai, K. Takemoto, K. Uematsu, T. Hirano, M. Nakayama, S. Nakahata, M. Ueno, D. Hara, Y. Kumagai, A. Koukitu, and H. Seki, Preparation of Large Freestanding GaN Substrates by Hydride Vapor Phase Epitaxy Using GaAs as a Starting Substrate, Jpn. J. Appl. Phys. **40**, L140–L143 (2001)

4. T. Sugahara, H. Sato, M. Hao, Y. Naoi, S. Kurai, S. Tottori, K. Yamashita, K. Nishino, L. T. Romano and S. Sakai, Jpn. J. Appl. Phys. **37** (1998) 398.

5. T. Kozawa, T. Kachi, H. Kano, and H. Nagase, N. Koide and K. Manabe, Thermal stress in GaN epitaxial layers grown on sapphire substrates, J. Appl. Phys. **77** (1995) 4389.

6. E. F. Schubert, Light-Emitting Diodes, Cambridge University Press, 2006, pp 91.

7. E. F. Schubert, Light-Emitting Diodes, Cambridge University Press, 2006, pp 86 - 87

8. M. Ohring, Materials science of thin films, Academic press, 2002, pp 429 - 431

9. X. J. Ning, F. R. Chien, and P. Pirouz, J. W. Yang and M. Asif Khan,

Growth defects in GaN films on sapphire: The probable origin of threading dislocations, J. Mater. Res. **11**, 580-592 (1996)

10. D. Zhu, D. J. Wallis and C. J. Humphreys, Prospects of III-nitride optoelectronics grown on Si, Rep. Prog. Phys. **76**, 106501 (2013)

11. J.S. Speck, S.J. Rosner, The role of threading dislocations in the physical properties of GaN and its alloys, Physica B **273-274**, 24-32 (1999)

12. G. Stoney, The tension of metallic films deposited by electrolysis, Proc. R. Soc. Lond. A **82**, 172 (1909)

13. T. S. Zheleva, O-H Nam, M. D. Bremser, and R. F. Davis, Appl. Phys. Lett. **71** (1997) 2472.

14.. P. Gibart, Rep. Prog. Phys. **67** (2004) 667.

15. K. Tadatomo, H. Okagawa, Y. Ohuchi, T. Tsunekawa, T. Jyouichi, Y. Imada, M. Kato, H. Kudo, T. Taguchi, High Output Power InGaN Ultraviolet Light-Emitting Diodes Fabricated on Patterned Substrates Using Metalorganic Vapor Phase Epitaxy, Phys. stat. sol. (a) **188** (2001) 121.

16. M. Yamada, T. Mitani, Y. Narukawa, S. Shioji, I. Niki, S. Sonobe, K. Degichi, M. Sano and T. Mukai, InGaN-Based Near-Ultraviolet and Blue-Light-Emitting Diodes with High External Quantum Efficiency Using a Patterned Sapphire Substrate and a Mesh Electrode, Jpn. J. Appl. Phys. **41** (2002) 1431.

17. S. J. Chang, Y. C. Lin, Y. K. Su, C. S. Chang, T. C. Wen, S. C. Shei, J. C. Ke, C. W. Kuo, S. C. Chen, C. H. Liu, Nitride-based LEDs fabricated on

patterned sapphire substrates, Solid-State Electronics **47** (2003) 1539.

18. H. Gao, F. Yan, Y. Zhang, J. Li, Y. Zeng, and G. Wang, Enhancement of the light output power of InGaN/GaN light-emitting diodes grown on pyramidal patterned sapphire substrates in the micro- and nanoscale, Journal of Applied Physics **103**, 014314 (2008)

19. J.-H. Lee, D.-Y. Lee, B.-W. Oh, and J.-H. Lee, Comparison of InGaN-Based LEDs Grown on Conventional Sapphire and Cone-Shape-Patterned Sapphire Substrate, IEEE Trans. Electron Devices **57**,157-163 (2010)

20. T. N. Oder, K. H. Kim, J. Y. Lin, and H. X. Jiang, Appl. Phys. Lett. **84** (2004) 466.

21. E. Matioli, E. Rangel, M. Iza, B. Fleury, N. Pfaff, J. Speck, E. Hu and C. Weisbuch, Appl. Phys. Lett. **96** (2010) 031108.

22. C. Huh, K-S Lee, E-J Kang and S-J Park, J. Appl. Phys. **93** (2003) 9383.

23. H-M An, J. I. Sim, K. S. Shin, Y. M. Sung and T. G. Kim, IEEE J. Quantum Electron. **48** (2012) 891.

24. K. Ueda, Y. Tsuchida, N. Hagura, F. Iskandar, K. Okuyama and Y. Endo, Appl. Phys. Lett.**92** (2008) 101101.

25. S. H. Park, J. Park, D.-J. You, K. Joo, D. Moon, J. Jang, D.-U.Kim, H. Chang, S. Moon, Y.-K.Song, G.-D. Lee, H. Jeon, J. Xu, Y. Nanishi and E. Yoon, Appl. Phys. Lett. **100**, (2012) 191116.

26. Rubicon Technology, Inc., Rubicon's large diameter patterned sapphire substrates for LED Industry (2013)

27. Jeonghwan Jang, Daeyoung Moon, Hyo-Jeong Lee, Donghyun Lee, Daehan Choi, Dukkyu Bae, Hwankuk Yuh, Youngboo Moon, Yongjo Park,

Euijoon Yoon, Incorporation of air-cavity into sapphire substrate and its effect on GaN growth and optical properties, Journal of Crystal Growth 430, 41–45 (2015)

28. Yoon-Jong Moon, Daeyoung Moon, Jeonghwan Jang, Jin-Young Na, Jung-Hwan Song, Min-Kyo Seo, Sunghee Kim, Dukkyu Bae, Eun Hyun Park, Yongjo Park, Sun-Kyung Kim, and Euijoon Yoon, Microstructured Air Cavities as High-Index Contrast Substrates with Strong Diffraction for Light-Emitting Diodes, Nano Letters 16, 3301-3308 (2016)

29. G. L. Olson and J. A. Roth, Kinetics of solid phase crystallization in amorphous silicon, Materials Science Reports **3**, 1-78 (1988)

30. D. A. Porter and K. E. Easterling, Phase transformations in metals and alloys, CRC press, p. 265 – 267 (2004)

31. R. B. Iverson and R. Reif, Recrystallization of amorphized polycrystalline silicon films on SiO_2: Temperature dependence of the crystallization parameters, J. Appl. Phys **62**, 1675-1681 (1987)

32. X.-Z. Bo, N. Yao, S. R. Shieh, T. S. Duffy, and J. C. Sturm, Large-grain polycrystalline silicon films with low intragranular defect density by low-temperature solid-phase crystallization without underlying oxide, J. Appl. Phys **91**, 2910 (2002)

33. H. A. Wriedt. The Al-O (Aluminum-Oxygen) System, Bulletin of Alloy Phase Diagrams **6**, 548-552 (1985)

34. Hannah Maret, Derek Weisberg, Helen M. Chan, and Nicholas C. Strandwitz, Seeded Solid-Phase Epitaxy of Atomic Layer Deposited Aluminum Oxide, *Cryst. Growth Des.16* **2016**, 1662–1666 (2016)

35. Afanas'ev, V. V., Stesmans, A., Mrstik, B. J., and Zhao, C., Impact of

annealing-induced compaction on electronic properties of atomic-layer-deposited Al2O3, Appl. Phys. Lett. **81**, 1678-1680 (2002)

36. L. Nistor, O. Richard, C. Zhao, H. Bender, A. Stesmans, G. Van Tendeloo, A microstructural study of the thermal stability of atomic layer deposited Al_2O_3 thin films, Institute of Physics Conference Series 180, 397-400 (2003)

37. C. W. White, L. A. Boatner, P. S. Sklad, C. J. McHargue, and M. J. Aziz, Ion implantation of crystalline oxides and ceramics, Nuclear Instruments and Methods in Physics Research B **32**, 11-22 (1988)

38. P. S. Sklad, J.C. McCallum, C.J. McHargue, and C.W. White, The amorphous-to-gamma transformation in ion implanted Al_2O_3, Nuclear Instruments and Methods in Physics Research B **46**, 102-106 (1990)

39. J. C. McCallum, T.W. Simpson, and I.V. Mitchell, Time resolved reflectivity measurements of the amorphous-to-gamma and gamma-to-alpha phase transitions in ion-implanted Al_2O_3, Nuclear Instruments and Methods in Physics Research B **91**, 60-62 (1994)

40. D. R. Clarke, Epitaxial phase transformations in aluminium oxide, phys. stat. sol. (a) **166**, 183 (1998)

41. T. W. Simpson, Qingzhe Wen, Ning Yu, and David R. Clarke, Kinetics of the amorphous $\rightarrow \gamma \rightarrow \alpha$ transformation in aluminium oxide: Effect of crystallographic orientation, Journal of American ceramics society, **81** [1] 61-66 (1998)

42. Ning Yu, Todd W. Simpson, Paul C. Mclntyre, Michael Nastasi, and Ian V. Mitchell, Doping effects on the kinetics of solid-phase epitaxial growth of amorphous alumina thin films on sapphire, Appl. Phys. Lett. **67** (7) (1995)

43. W. E. Lee and K. P. D. Lagerof, Structural and electron diffraction data for sapphire (α-Al_2O_3), Journal of electron microscopy technique 2, 247-258 (1985)

44. R.-S. Zhou and R. L. Snyder, Structures and transformation mechanisms of the η, γ, and θ transition aluminas, Acta Cryst. B47, 617-630 (1991)

45. S. Cao, A. J. Pedraza, D. H. Lowndes, and L. F. Allard, γ-Al2O3 formation from pulsed-laser irradiated sapphire, Appl. Phys. Lett. 65, 2940 (1994)

46. Ning Yu, Paul C. McIntyre, Michael Nastasi, and Kurt E. Sickafus, High-quality epitaxial growth of γ-alumina films on α-alumina sapphire induced by ion-beam bombardment, Phys. Rev. B 52, 17518 (1994)

Chapter 2. Fabrication of cavity engineered sapphire substrate

2.1. Introduction

As discussed in the **chapter 1**, technical issues in GaN-based LEDs, such as high density of threading dislocations, low light extraction efficiency, and wafer bow, should be resolved to improve the efficiency and productivity. In this research, we proposed new growth scheme using a cavity engineered sapphire substrate (CES) in which cavity patterns are arrayed on a sapphire substrate for the high efficient and less bowed LEDs.[1,2] A two-dimensionally patterned cavity array could be incorporated into the interface between the GaN and sapphire substrate by growing the GaN layer on the CES. Threading dislocation density can be reduced during an ELO process on the CES and the pattern at the interface is expected to enhance the light extraction efficiency, improving the LED chip efficiency. In addition, the existence of air voids inside the pattern is expected to reduce the wafer bow. Moreover, this method is expected to enable us to control the shape, size, and distribution of the void pattern more easily, implying that we can further optimize the pattern parameters as well as the growth conditions for the improvement of the LED efficiency and the reduction of the wafer bow. In this chapter, details on the fabrication procedure of the CES and microstructure of the annealed alumina cavity structure will be discussed.

2.2. Experimental details

Figure 1 shows a schematic diagram of the fabrication of CES. Photoresist (PR) patterning was performed on a c-plane sapphire substrate by standard photolithography. After the PR patterning, a thermal reflow process was performed to modify the shape of the PR pattern, for example, to change a cylindrical pattern to a hemispherical pattern. An amorphous alumina (Al_2O_3) layer was then deposited on the PR patterned sapphire substrate by atomic layer deposition (ALD), NCD LUCIDA D100. H_2O and trimethylaluminum were used as oxygen and aluminum sources, respectively. Thermal treatment was then performed in an air ambient furnace. The increasing rate of the temperature was 5 ^oC/min. During the thermal treatment, PR was burned, leaving a cavity and alumina shell remaining on the substrate surface. At the same time, the amorphous alumina layer was crystallized into metastable γ-phase, and then subsequently into α-phase, a phase of the sapphire substrate, by solid phase epitaxy (SPE).[3-7] The crystallization process is critical because CES acts as a substrate for the subsequent growth of the GaN layer.

The surface morphology and the cross-section view of the samples were observed by a Hitachi S-4800 field emission scanning electron microscope (FESEM) operated at 15 kV. Thickness uniformity of the ALD machine was confirmed by the ellipsometer, RUDOLPH/FE-VIID**.** Phase of the ALD alumina layer was investigated by electron backscattering diffraction (EBSD), TSL EBSD. The surface morphology of the alumina layer was measured by the atomic force microscope (AFM), Park Systems XE-100. The microstructure was investigated by transmission electron microscope (TEM),

JEM-2100F operated at 200 kV. The TEM samples were made using a focused ion beam (FIB). During the FIB process, carbon and Pt metal were used as protective layers, which prevented surface damages from the Ga beam. X-ray reflectivity (XRR) curves were measured by a PANalytical X'pert Pro XRD operated at 30 kV. Thermal decomposition of the PR was investigated by thermal gravimetric analyzer (TGA), TA Instruments Q-5000 IR.

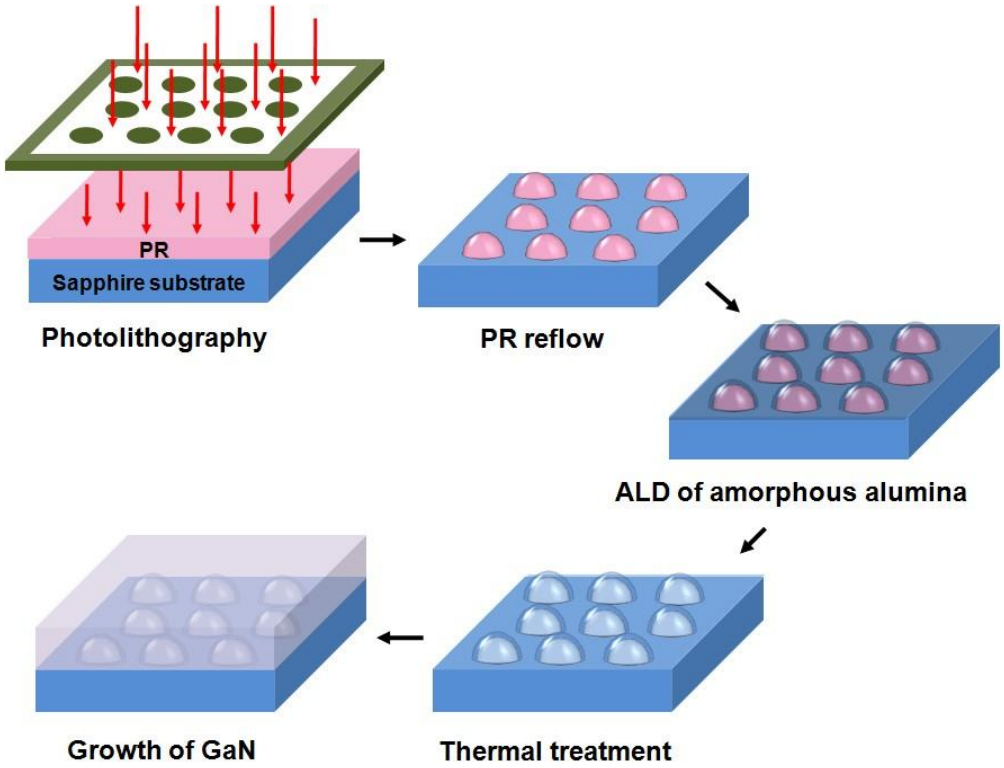

Figure 2.1 Schematic diagram of the fabrication of CES and growth of GaN on it.

2.3. PR patterning and thermal reflow

Cylindrical PR pattern was formed on a 2 inch c-plane sapphire substrate. Figure 2.2 shows cross-section and plane-view SEM images of the PR patterned substrate. Width, spacing, and height of the used PR pattern were 2 μm, 1 μm, and 2.3 μm, respectively. It is clearly shown that the patterned PR were uniform in size. After that, thermal reflow process was performed to modify the PR as hemispherical shape. It is well known that cylindrical shape of pattern is less effective on the light extraction, compared to the hemispherical, or conical type of patterns.[8] In addition, planar top area of the cylindrical pattern gives undesired growth template[9], which could disrupt the coalescence of GaN layers. This will be described in detail in **chapter 6**. Figure 2.3 shows the cross-section SEM image of PR pattern before and after the thermal reflow. As shown in Fig. 2.3 (b), the PR was modified to hemispherical shape after thermal reflow at 150 ^{o}C for 40 min in a dry oven. At higher temperature of 160 ^{o}C, the thermal reflow was excessively proceeded, resulting in the attachment of the PR patterns each other as shown in Fig. 2.3 (c). Therefore, reflow for the fabrication of CES was performed at 150 ^{o}C. Subsequently, PR ashing process was performed to remove the residues on the bare sapphire surface between the patterns. When the residues remain on the bare sapphire surface after the photolithography process, the alumina layer was detached from the sapphire surface during subsequent thermal decomposition of the PR and resultantly surface peeling of the alumina layer occurs as shown in Fig. 2.4.

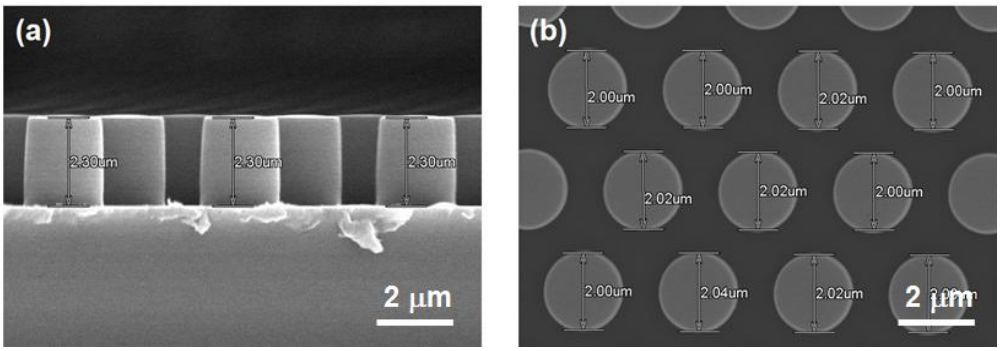

Figure 2.2 (a) Cross-section and (b) plane-view SEM images of the PR patterned sapphire substrate.

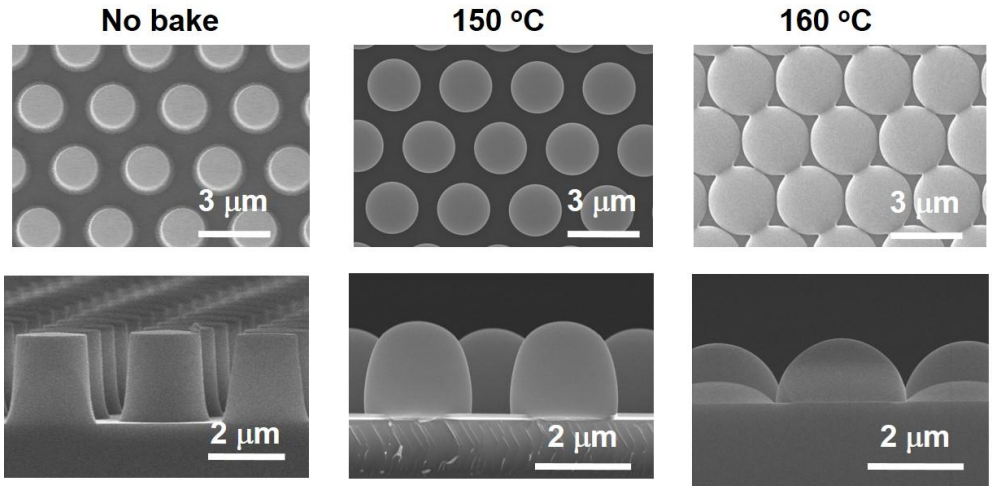

Figure 2.3 Cross-section and plane-view SEM image of the PR patterned sapphire substrate

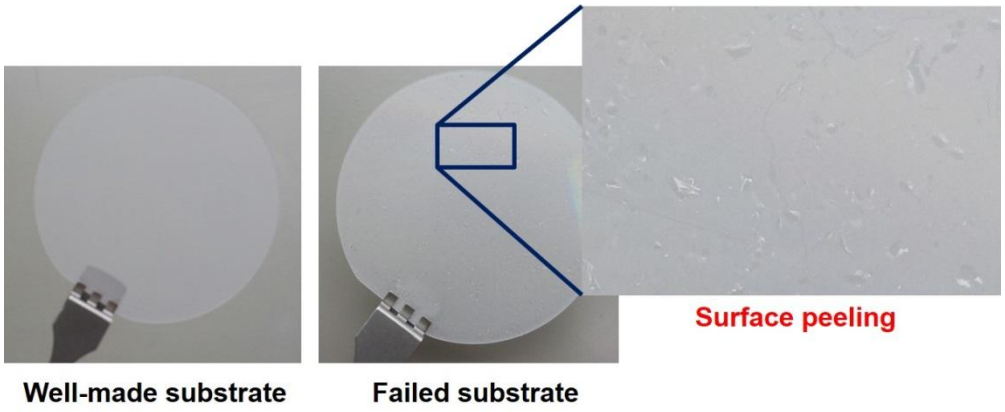

Figure 2.4 Photograph of the well-made CES and failed CES due to surface peeling.

2.4. Atomic layer deposition of amorphous Al_2O_3 layer

2.4.1 Optimization of the ALD process for the fabrication of CES

After the PR patterning process, alumina layer was deposited on the PR patterned sapphire substrate. Because ALD process gives excellent step coverage[10], the alumina layer could be uniformly deposited on not only PR patterns but also planar area between the patterns. Table 2.1 shows one ALD cycle of alumina layer, involving two self-limiting reactions of the TMA and H_2O. This results in layer by layer deposition of the aluminum and oxygen atoms. For the CES, the ALD process was carried out at a low temperature (110 ^oC) to keep the shape of the PR pattern during ALD. Figure 2.5 shows the cross-section SEM images of the PR pattern before and after the ALD of 1000 cycles. It is found that the shape of PR pattern was not deformed during the ALD process.

The number of deposition cycles was determined considering the mechanical collapse of the cavity pattern during the subsequent thermal treatment process. For the sample with ALD of 200 cycles, the cavity pattern collapsed down after the subsequent thermal treatment as shown in Fig. 2.6 (a). It is speculated that the inside PR may be in a liquid state at high annealing temperature and the cavity structure could not mechanically withstand capillary force between the alumina shell and the inside liquid PR. For the sample with ALD of 800 cycles, most of the patterns survived but some patterns shrank or detached out of the substrate as shown in Fig. 2.6 (b). The thicker alumina layer better withstood the mechanical collapse during the thermal treatment. The well-defined cavity pattern was maintained when the

number of ALD cycles were larger than 1000 as shown in Fig. 2.6 (c). For the fabrication of the CES with hemispherical patterns, the ALD was performed by 1000 cycles.

2.4.2 Properties of the ALD Al_2O_3 layer

To confirm the properties of the ALD alumina layer in the optimized condition for the CES, EBSD, AFM, TEM, and XRR analysis were performed for the alumina layer deposited at 110 ^{o}C for 1000 cycles on a planar substrates. The ALD alumina layer was revealed to be amorphous by the EBSD analysis as shown in Fig. 2.7 (a). In Fig. 2. 7 (b), AFM image shows smooth surface of the amorphous alumina layer with root-mean-square roughness of 0.366 nm (over an area of 5 $\times$ 5 μm^2). To measure the thickness of the amorphous layer, TEM measurement was performed as shown in the Fig. 2.8. The 1000 cycles of ALD corresponds to the 80 nm thick alumina layer. In addition, the TEM image revealed amorphous phase of the alumina layer corresponding to the EBSD result. In order to quantify stoichiometry of the ALD alumina, XPS analysis was performed for the sapphire substrate and amorphous alumina deposited on a sapphire substrate by ALD at 110 ^{o}C for 1000 cycles as shown in Fig. 2.9. From the areas of the XPS spectra for the Al2p and O1s core levels, atom % of the oxygen and aluminum ions in the sapphire substrate and ALD alumina was calculated. The O/Al ratio of the ALD alumina was calculated to be 1.53 which is comparable to the sapphire substrate (O/Al: 1.5). The density of the amorphous alumina layer was measured using XRR analysis. The density of

the amorphous alumina layer is very important parameter because the 3-D alumina cavity structure experiences severe volume contraction due to the density increase during the subsequent crystallization process. This subject will be discussed in detail in **Chapter 4**. It was reported that the densities of amorphous alumina was varied from 2.1 to 3.5 g/cm^3 depending on the deposition technique and conditions.[11] Figure 2.10 shows the measured and fitted scans for the amorphous alumina layer deposited on a Si substrate by ALD at 110 ^{o}C for 1000 cycles. To assure accuracy of the measurement, the amorphous layer was deposited on a Si substrate, which shows relatively lager refractive index difference with the alumina layer than the sapphire substrate. From the fitting, the calculated density was 2.81 g/cm^3, which is much smaller value compared to that of the γ-Al_2O_3 (3.61 ~ 3.67 g/cm^3) and α-Al_2O_3 (3.99 g/cm^3), intermediate and final phase of the alumina after the subsequent thermal treatment, respectively.[11-14]

Table. 2.1 ALD cycle of the Al_2O_3

Step	1	2	3	4
Process	TMA pulse	TMA purge	H_2O pulse	H_2O purge
Time	0.2 s	10 s	0.2 s	10 s

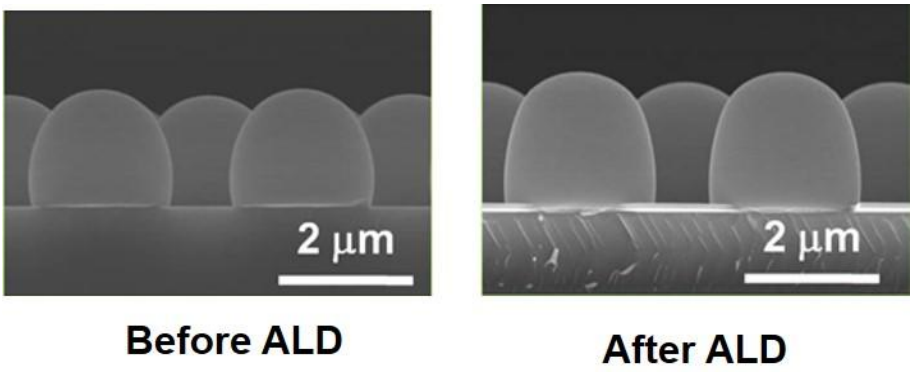

Figure 2.5 Cross-section SEM images of the PR pattern before and after ALD of 1000 cycles.

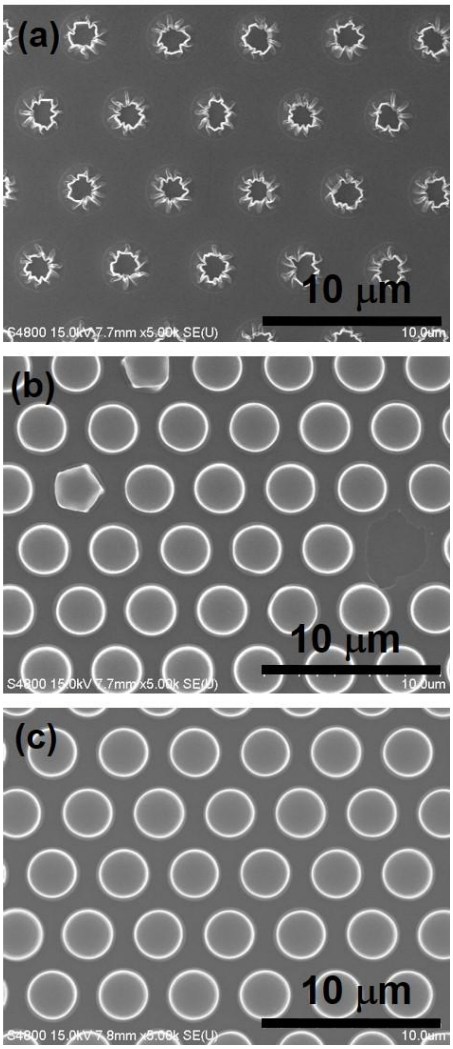

Figure 2.6 Plane-view SEM image of the alumina layers on the PR patterned substrate after the subsequent thermal treatment. For the samples, the ALD was performed by (a) 200 cycles, (b) 800 cycles, and (c) 1000 cycles, respectively.

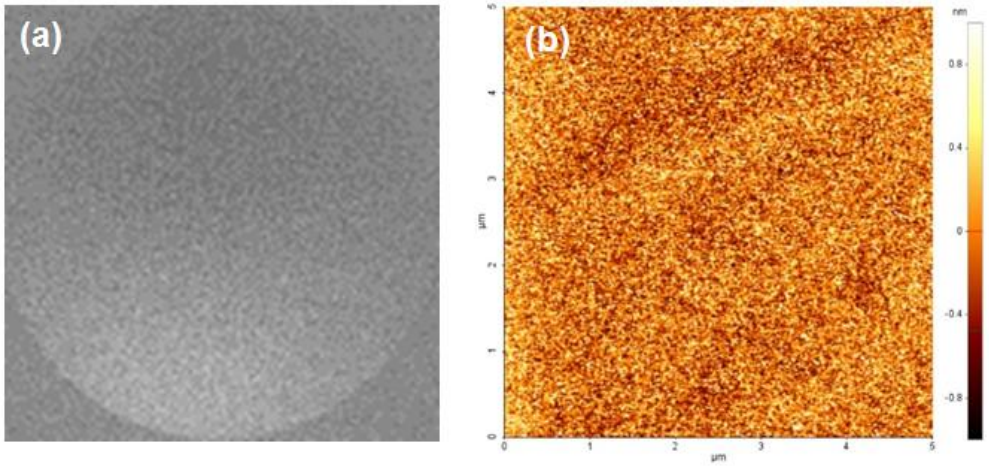

Figure 2.7 (a) EBSD and (b) AFM image of the amorphous layer deposited on a planar sapphire substrate by ALD at 110 ^{o}C for 1000 cycles.

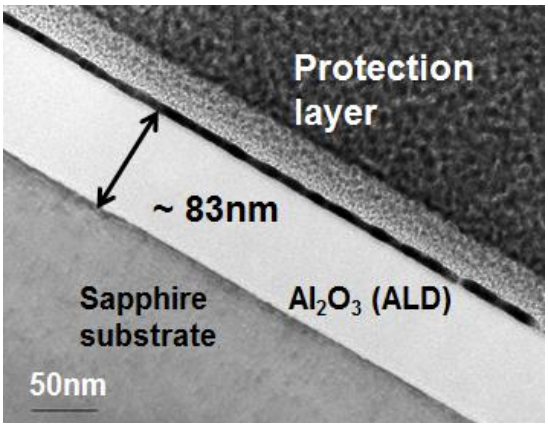

Figure 2.8 TEM image of the amorphous alumina layer on a sapphire substrate by 1000 cycles at 110 ^{o}C.

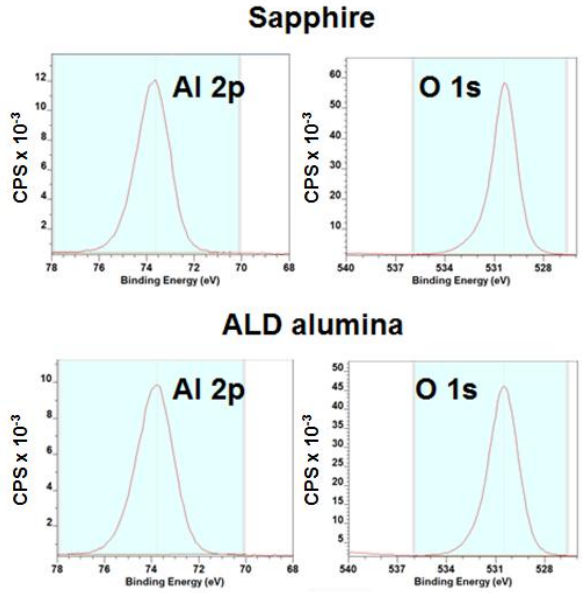

	O atom %	Al atom %
Sapphire substrate	60.0	40.0
ALD alumina	60.5	39.5

Figure 2.9 Results of XPS analysis on the bare sapphire substrate and amorphous alumina layer deposited on a sapphire substrate by ALD at 110 ^{o}C for 1000 cycles. XPS spectra of the Al2p and O1s core levels for the sapphire substrate and ALD alumina are shown. The table shows atom % of the oxygen and aluminum for the sapphire substrate and ALD alumina.

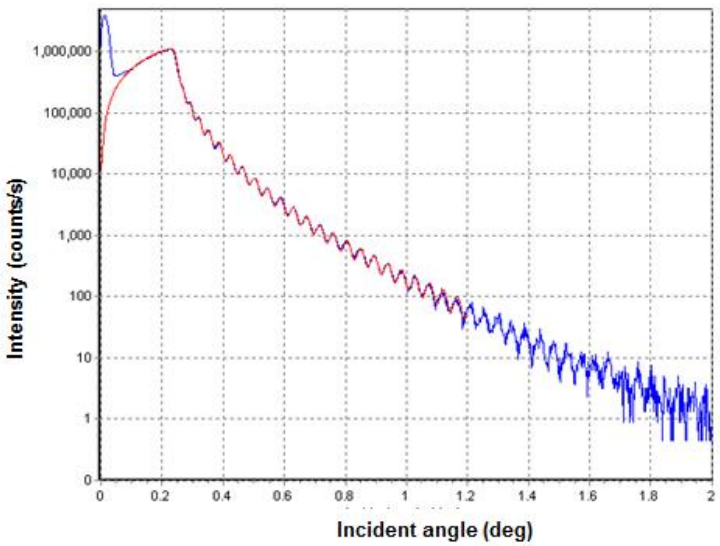

Figure 2.10 XRR intensity with incident angle for the amorphous alumina layer deposited on a Si substrate by ALD at 110 ^{o}C for 1000 cycles.

2.5. Thermal treatment for fabrication of the CES

2.5.1 Annealing condition for fabrication of the CES

After the ALD process, thermal treatment was performed in an air ambient furnace for the thermal decomposition of the PR and crystallization of the amorphous alumina layer. The temperature required for thermal decomposition of the PR is relatively lower than that for the crystallization. Generally, PR is composed of a polymer and solvent, which are easily decomposed by thermal treatment in air ambient. To find out the decomposition temperature of the used PR, GXR 601, thermogravimetric analysis (TGA) was performed in air ambient as shown in the Fig. 2.11 (a). The TGA was carried out for a specimen in which a drop of PR was prepared on a piece of Si substrate without the deposition of amorphous alumina layer because the amount of PR in the actual CES fabrication process is so small that TGA analysis is impossible. As the temperature increases, weight of the sample was decreased by thermal decomposition and finally the decrease was saturated in the temperature over 650 ^{o}C, indicating that the PR was completely decomposed. Figure 2.11 (b) shows schematic diagram of a formation of the amorphous alumina cavity structure after burning out of the PR. It is speculated that CO_2 or H_2O, products for the oxidation of the PR, diffuses out through the porous amorphous alumina layer, leaving a cavity and alumina shell remaining on the substrate surface.

In addition to the decomposition of PR, SPE of the alumina layer should be considered to determine the annealing condition. It was known that during high temperature annealing, SPE of amorphous alumina on a sapphire

substrate proceeds in two-step phase transformation from amorphous to metastable γ-phase and then subsequently to α-phase as shown in the Fig. 1.18. It was reported that the phase transformation of Al_2O_3 thin films from amorphous to γ-phase was observed in the temperature range above 700 ^oC and that from γ- to α-phase was observed in the higher temperature range than 800 ^oC since it required higher activation energy.[3-7]

Figure 1. 12 shows schematic diagram of the thermal treatment sequence for the fabrication of CES. To prevent collapse of the cavity structure by abrupt oxidation process of the PR, firstly, the PR was burned out at a low temperature slowly. The thermal treatment was performed at 450 ^oC for 2 hrs and then subsequently at 600 ^oC for 2 hrs. This setting temperature was roughly determined based on the TGA result, which showed two temperature range with different slope around ~ 450 ^oC and ~ 600 ^oC. In order to optimize the thermal treatment conditions, TGA analysis of the PR pattern covered with the alumina layer in the actual CES process will be required. Then, the temperature was increased to crystallize the amorphous alumina layer by SPE. The thermal treatment for SPE was performed in two step; at 850 ^oC for 1 hr for the phase transformation from amorphous to γ-phase and at 1150 ^oC for 2 hrs for that from γ- to α-phase. This is because an one step thermal treatment at high temperature result in the random nucleation of γ-Al_2O_3 rather than the SPE in the planar region between the patterns, in which GaN will be grown, which could reduce crystal quality of the subseqeuntly grown α-Al_2O_3. Accordingly, the alumina layer was crystallized into γ-phase by SPE at a

lower temperature in advance and then the temperature was increased for the SPE into α-phase. The detailed crystallization procedure will be discussed **in Chapter 3**. The phase and microstructure of the alumina layer annealed at 850 ^{o}C and 1150 ^{o}C will be discussed in the following section.

2.5.2 Microstructure and crystalline quality of the annealed Al_2O_3 layer

In order to investigate the phase and microstructure of the annealed alumina layer, TEM analysis was performed. Figure 2.13 (a) shows TEM image of the alumina cavity structure annealed at 850 ^{o}C for 1 hr, which was recorded at the [1-100] zone axis of the sapphire substrate. Oxide residues inside the alumina shell were generated and accumulated within the alumina shell during the FIB process. The well-defined air cavities surrounded by crystallized alumina shell was observed. Figure 2.13 (b) shows more magnified TEM image at the marked region by red square in Fig. 2.12 (a). It was found that the planar area between the cavity patterns was epitaxial γ-Al_2O_3 transformed from the sapphire substrate by SPE. The inset in Fig. 2.13 (b) shows selected area diffraction pattern (SADP) of the SPE γ-Al_2O_3. Actually, the SPE γ-Al_2O_3 consisted of two kinds of twin-related domains with epitaxial relationship of $\{111\}_{\gamma}//\{0001\}_{\alpha}$ (this will be discussed in detail in **Chapter 4)**. Thus, overlap of the diffraction patterns from the each domain results in the large number of diffraction spots in the SADP of the SPE γ-Al_2O_3 layer while the $<111>_{\gamma}$ direction parallels to the $<0001>_{\alpha}$ c-direction of

the α-Al_2O_3 substrate. However, the upper cavity shell was observed to be nanocrystalline γ-Al_2O_3 as shown in Fig. 2.13 (b). The interface between SPE γ-Al_2O_3 and nanocrystalline γ-Al_2O_3 was observed at the cavity shell as indicated by dotted line in the figure. This implies that the progress of SPE into γ-Al_2O_3, initiated from the surface of sapphire substrate, was blocked by the onset of random nucleation in the alumina shell. The TEM investigation revealed that during the annealing at 850 ^oC for 1hr, the planar alumina layer between the cavity patterns, which will be served as a template for growth of GaN, was epitaxially transformed into γ-phase by SPE while the remaining upper cavity shell was transformed into nanocrystalline γ-phase by random nucleation.

Figure 2.14 (a) shows TEM image of the alumina cavity structure annealed at 850 ^oC for 1 hr and then subsequently at 1150 ^oC for 2hrs, which was recorded at the [1-100] zone axis of the sapphire substrate. The inset in Fig. 2.14 (a) shows SADP of the sapphire substrate. The dotted white line indicates initial surface of the sapphire substrate. The well-defined alumina cavity structure was maintained after the high temperature annealing at 1150 ^oC. Figure 2.14 (b) shows more magnified TEM image at the planar region between the cavity patterns. It was found that the nanocrystalline γ-Al_2O_3 in the cavity shell as well as the epitaxial γ-Al_2O_3 in the planar region was epitaxially transformed into α-phase by SPE. In this annealing condition, the random nucleation of the α-Al_2O_3 was not observed. The inset in Fig. 2.14 (b) shows SADP obtained at the top area of the cavity shell as marked by red circle in Fig. 2.14 (a). The SADP at the top area corresponds to that of the sapphire substrate (inset in Fig. 2.14 (a)), indicating that the whole alumina

cavity structure was completely transformed into single crystalline α-phase by SPE from the sapphire substrate. Therefore, the epitaxially grown planar α-Al_2O_3 layer between the cavity patterns can provide c-plane α-Al_2O_3 surface for the subsequent epitaxial growth of GaN.

Figure 2.15 shows cross-section scanning transmission electron microcopy (STEM) image of the α-Al_2O_3 cavity structure. It was found that nanopores (darker contrast in the STEM image) are formed in the SPE α-Al_2O_3 layer. The nanopore was not observed in the γ-Al_2O_3 layer. The formation of nanopores in α-Al_2O_3 might be due to the volume reduction of the alumina by density increase during the phase transformation from γ- to α-phase.[15] The formation of nanopores during the SPE can cause atomic disorder in the crystallized α-Al_2O_3. Note that the number of nanopores was much less in the planar region which was transformed from epitaxial γ-Al_2O_3 compared to that in the cavity shell which was transformed from nanocrystalline γ-Al_2O_3. This result suggests that the microstructure of pre-existing γ-Al_2O_3 greatly affect the formation of nanopores in α-Al_2O_3. Therefore, to obtain high quality α-Al_2O_3 with less nanopores, fine structure of the intermediate γ-Al_2O_3 should be precisely controlled.

In order to evaluate the crystal quality of the SPE α-Al_2O_3, reciprocal space map (RSM) in X-ray diffraction for asymmetrical (11-23) reflection of the SPE α-Al_2O_3 on a planar sapphire substrate was recorded compared to the bare sapphire substrate as shown in Fig. 2.16 (a) and (b), respectively. The thermal treatment for the SPE α-Al_2O_3 proceeded in the same procedure for the fabrication of CES as shown in Fig. 2.12. The distribution of X-ray diffraction intensity for the SPE α-Al_2O_3 on a sapphire substrate was larger

than that of the bare sapphire substrate, indicating lower crystal quality of the SPE α-Al_2O_3 compared to that of sapphire substrate. This is because structural defects and nanopores are generated in the epitaxial layers during the SPE procedure. Accordingly, to further improve the crystal quality of the GaN layer and resultant LED performances on the CES, the crystal quality of the SPE α-Al_2O_3 need to be improved by precise control of the epitaxial layers during the SPE procedure.

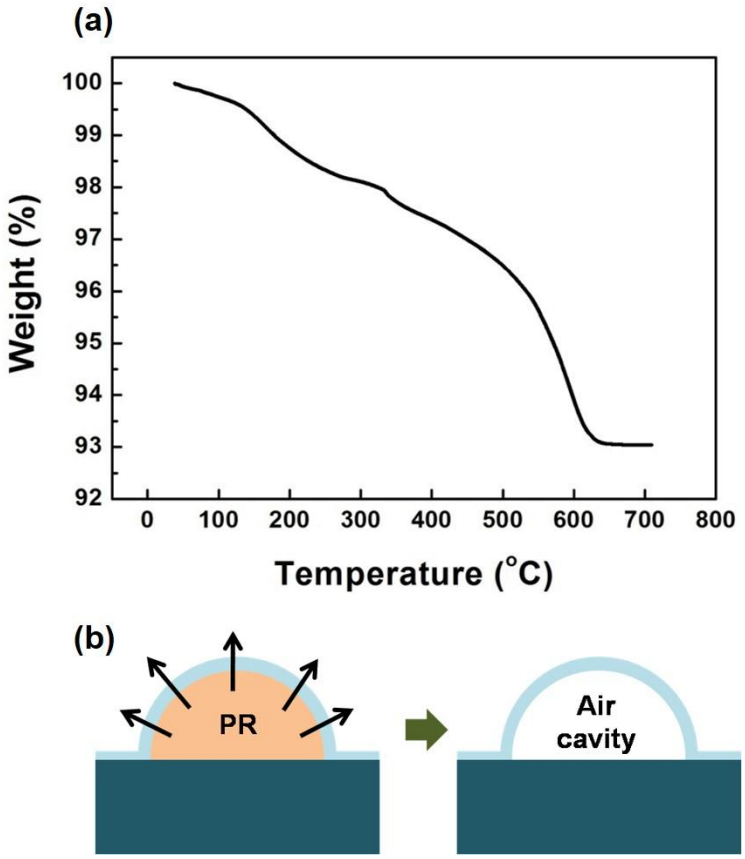

Figure 2.11 (a) Thermogravimetric analysis of the used PR. (b) Schematic diagram for burning out of the PR and formation of the amorphous alumina cavity structure.

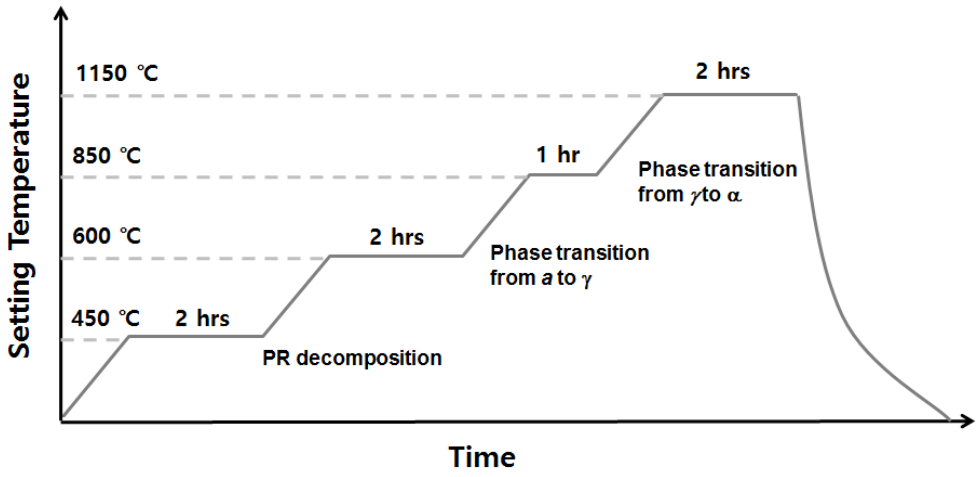

Figure 2.12 Schematic diagram of thermal treatment sequence for the fabrication of CES.

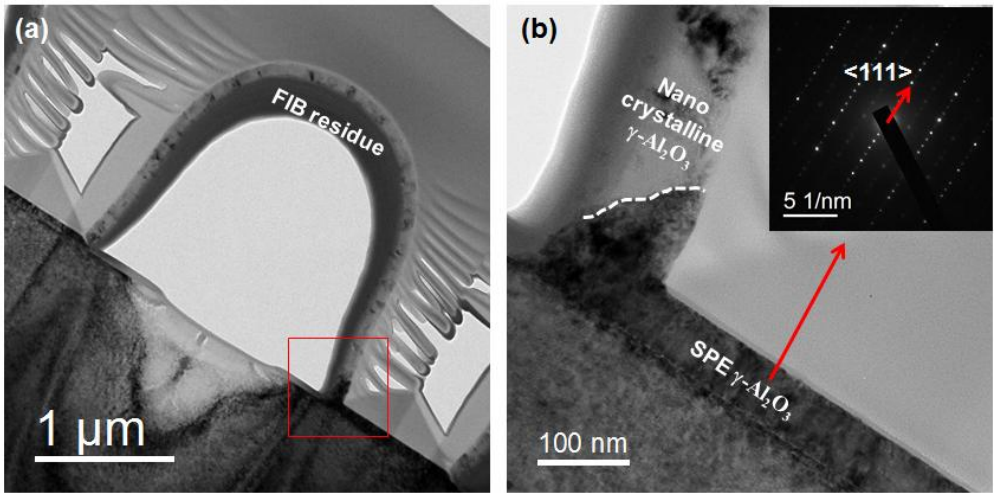

Figure 2.13 (a) Cross-section bright field TEM image of the alumina cavity structure annealed at 850 ^{o}C for 1hr. (b) More magnified TEM image at the marked region by red square in Fig. 2.12 (a). The inset in Fig. 2.12 (b) shows SADP at the SPE γ-Al_2O_3 layer.

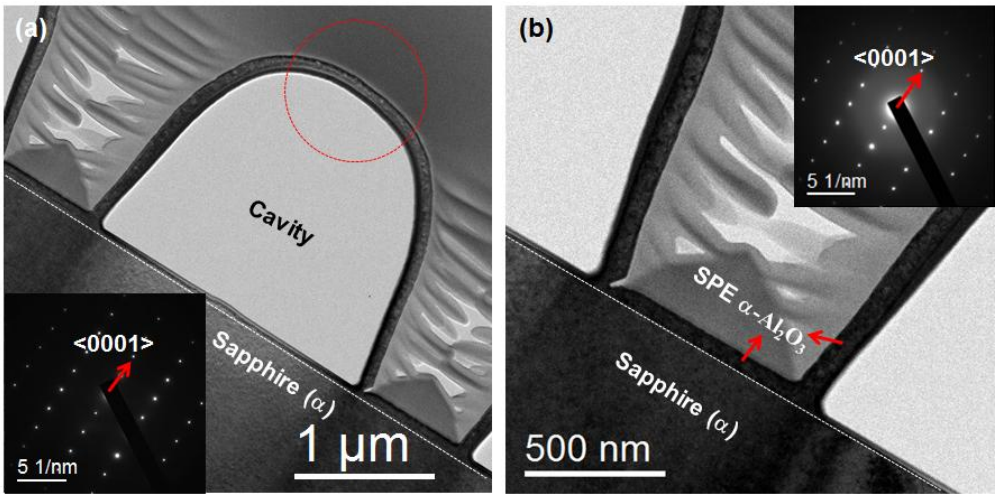

Figure 2.14 (a) Cross-section bright field TEM image of the alumina cavity structure annealed at 850 ^{o}C for 1hr and subsequently at 1150 ^{o}C for 2 hrs. The inset in Fig. 2.13 (a) shows SADP at the sapphire substrate. (b) More magnified TEM image at the planar region between the cavity patterns. The inset in Fig. 2.13 (b) shows SADP at the top area of the cavity shell as marked by red circle in Fig. 2.13 (a).

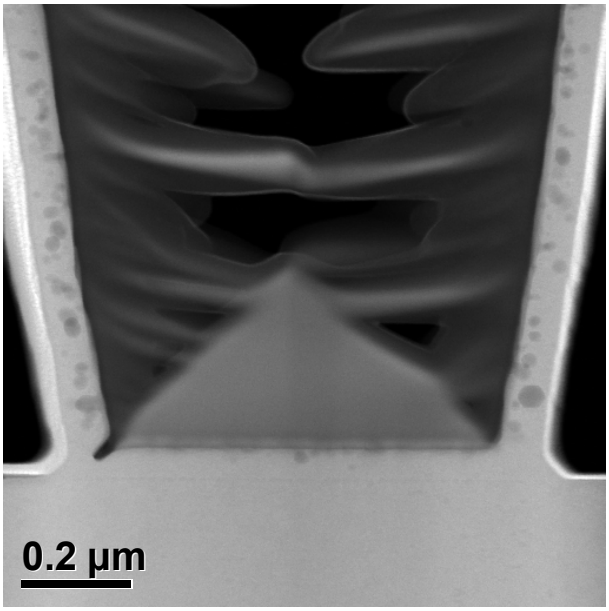

Figure 2.15 Cross-section STEM image of the α-Al_2O_3 cavity structure obtained at the planar region between the cavity patterns.

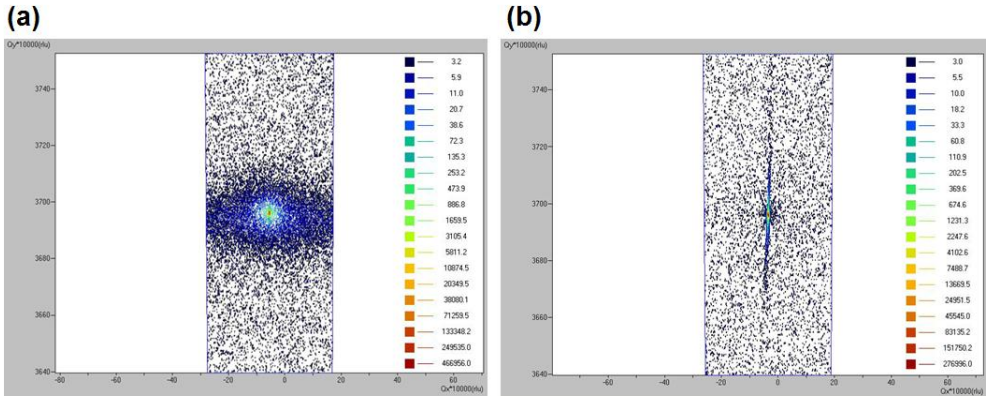

Figure 2.16 Reciprocal space maps in X-ray diffraction for (11-23) reflection of (a) bare sapphire substrate and (b) SPE α-Al_2O_3 layer on a sapphire substrate. The unit rlu is defined as $\lambda/2d$.

2.6 CES with various cavity shape

Figure 2. 17 shows plane-view and cross-section SEM images of the samples in the fabrication procedure of the CES. After the thermal treatment, the well-defined hexagonal array of the hemispherical pattern was formed on a sapphire substrate following the initial PR shape. The cross-section view of the cavity after thermal treatment illustrates that the ALD alumina layer was deposited conformally not only on the PR pattern but also on the surface of the substrate, as indicated by the arrows. Since the shape, size, and distribution of the cavity structure follow those of the PR pattern as shown in Fig. 2. 17, it is possible to easily fabricate CES with various pattern shapes such as a hemisphere, cylinder, cone and square in different sizes and distributions. Figure 2.18 (a)-(d) shows CESs with various shape and size of cavity pattern. Therefore, this scheme enable us to control the shape, size, and distribution of the void pattern more easily, implying that we can further optimize the pattern parameters as well as the growth conditions for the improvement of the LED efficiency and the reduction of the wafer bow. Furthermore, for the stripe CES shown in Fig. 2.18 (d), the planar top layer of the alumina shell, which is parallel to the c-plane of sapphire substrate, provide c-plane α-Al_2O_3 surface since the alumina shell was fully crystallized into single crystalline α-phase from the sapphire substrate by SPE. Thus, the GaN epitaxial layer could be grown on the thin α-Al_2O_3 membrane.[16] The ultra-thin α-Al_2O_3 nanomembrane can be used as a compliant substrate for the growth of high quality GaN.[16] Thus, due to the flexibility in shaping of the cavity pattern, the CES scheme can be applied to various research for high efficiency GaN-based LEDs.

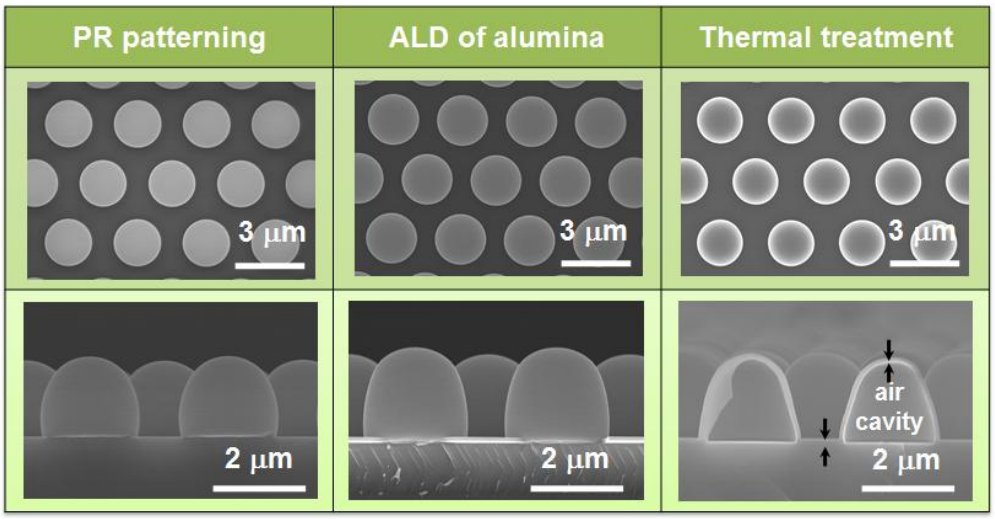

Figure 2.17 Plane-view and cross-section SEM images of the samples after the PR patterning, ALD of alumina, and thermal treatment.

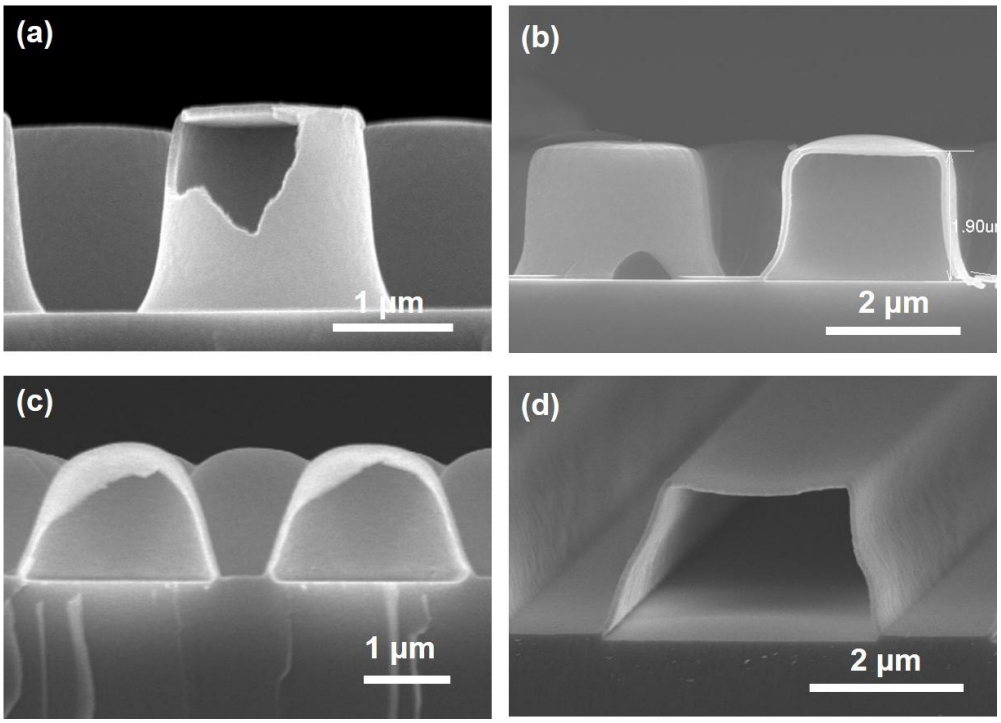

Figure 2.18 Cross-section SEM images of the CESs with various pattern shape of cavity pattern. (a) Cylindrical shape with diameter of 2 μm. (b) Cylindrical shape with diameter of 3 μm. (c) Hemispherical shape with diameter of 2.5 μm. (d) Stripe with width of 3 μm.

2.7 Summary

For the high efficiency GaN-based LEDs, we suggested a new substrate, a cavity engineered sapphire substrate (CES), in which a patterned cavity array was formed on the sapphire surface. Amorphous alumina film was deposited by atomic layer deposition on a photoresist patterned sapphire substrate, and subsequent high temperature annealing resulted in the formation of a cavity array surrounded by a crystallized sapphire shell. The SEM images show that the well-defined hexagonal array of the hemispherical cavity pattern was formed on a sapphire substrate following the initial PR shape after the thermal treatment. In addition, the TEM analysis revealed that the amorphous alumina layer was epitaxially crystallized into single crystalline α-phase from the sapphire substrate by SPE, indicating that the planar SPE α-Al_2O_3 layer between the cavity patters can be served as a growth seed for GaN. However, nanopores were found in the SPE α-Al_2O_3 layer and RSM analysis confirmed that crystal quality of the SPE α-Al_2O_3 layer was not as good as that of sapphire substrate. In order to further improve the crystal quality of the GaN layer and resultant LED performances on the CES, crystal quality of the SPE α-Al_2O_3 need to be improved by precise control of the SPE procedure. In this new growth scheme, it is possible to fabricate CES with various pattern shapes such as a hemisphere, cylinder, cone and square in different sizes and distributions. Therefore, we expect that this scheme is more flexible than conventional approaches in the optimization of a cavity structure for the improvement of LED efficiency and the reduction of the wafer bow.

2.8 Bibliography

1. Jeonghwan Jang, Daeyoung Moon, Hyo-Jeong Lee, Donghyun Lee, Daehan Choi, Dukkyu Bae, Hwankuk Yuh, Youngboo Moon, Yongjo Park, Euijoon Yoon, Incorporation of air-cavity into sapphire substrate and its effect on GaN growth and optical properties, Journal of Crystal Growth **430**, 41–45 (2015)

2. Yoon-Jong Moon, Daeyoung Moon, Jeonghwan Jang, Jin-Young Na, Jung-Hwan Song, Min-Kyo Seo, Sunghee Kim, Dukkyu Bae, Eun Hyun Park, Yongjo Park, Sun-Kyung Kim, and Euijoon Yoon, Microstructured Air Cavities as High-Index Contrast Substrates with Strong Diffraction for Light-Emitting Diodes, Nano Letters **16**, 3301-3308 (2016)

3. C.W. White et al., Ion implantation of crystalline oxides and ceramics, Nuclear Instruments and Methods in Physics Research B **32**, 11-22 (1988)

4. P.S. Sklad, J.C. McCallum, C.J. McHargue, and C.W. White, The amorphous-to-gamma transformation in ion implanted Al_2O_3, Nuclear Instruments and Methods in Physics Research B **46**, 102-106 (1990)

5. J.C. McCallum, T.W. Simpson, and I.V. Mitchell, Time resolved reflectivity measurements of the amorphous-to-gamma and gamma-to-alpha phase transitions in ion-implanted Al_2O_3, Nuclear Instruments and Methods in Physics Research B **91**, 60-62 (1994)

6. D.R. Clarke, Epitaxial phase transformations in aluminium oxide, phys. stat. sol. (a) **166**, 183 (1998)

7. Todd W. Simpson, Qingzhe Wen, Ning Yu, and David R. Clarke, Kinetics of the amorphous → g → a transformation in aluminium oxide: Effect of crystallographic orientation, Journal of American ceramics society, **81**, 61-66 (1998)

8. Ho Ju Kang, Sang Uk Cho, Eung Soo Kim, Chang-Seok Kim, and Myung Yung Jeong, Improving light-emitting diode performance through sapphire substrate double-side patterning, Optical Engineering **52**, 023002 (2013)

9. Hung-Cheng Lin, Hsueh-Hsing Liu, Geng-Yen Lee, Jen-Inn Chyi, Chang-Ming Lu, Chih-Wei Chao, Te-Chung Wang, Chun-Jong Chang and Solomon W. S. Chi, Effects of Lens Shape on GaN Grown on Microlens Patterned Sapphire Substrates by Metallorganic Chemical Vapor Deposition, Journal of The Electrochemical Society **157**, H304-H307 (2010)

10. Hyungjun Kim, Han-Bo-Ram Lee, W.-J. Maeng, Applications of atomic layer deposition to nanofabrication and emerging nanodevices, Thin Solid Films **517**, 2563–2580 (2009)

11. Raquel Liz´arraga, Erik Holmstr¨om, Stephen C. Parker, and Corinne Arrouvel, Structural characterization of amorphous alumina and its polymorphs from first-principles XPS and NMR calculations, Phys. Rev. B **83**, 094201 (2011)

12. Tania M. H. Costa, Márcia R. Gallas, Edilson V. Benvenutti, and João A. H. da Jornada, Study of Nanocrystalline γ-Al_2O_3 Produced by High-Pressure Compaction, J. Phys. Chem. B **103**, 4278–4284 (1999)

13. F. W. Dynys and J. W. Halloran, Alpha Alumina Formation in Alum-Derived Gamma Alumina, *J. Am. Ceram. Soc.* ***65****, 442–448 (1982)*

14. International Centre for Diffraction Data, PDF Number: 00-046-1212 (2012)

15. Ning Uu, Qingzhe Wen and David R. Clark, Paul C. Mclntyre, Harriet Kung, Michael Nastasi, Todd W. Simpson, Ian V. Mitchell, and DeQuan Li, Formation of iron or chromium doped epitaxial sapphire thin films on sapphire substrates, J. Appl. Phys. 78, 5412 (1995)

16. Daeyoung Moon, Jeonghwan Jang, Daehan Choi, In-Su Shin, Donghyun Lee, Dukkyu Bae, Yongjo Park, and Euijoon Yoon, An ultra-thin compliant sapphire membrane for the growth of less strained, less defective GaN, Journal of Crystal Growth **441**, 52-57 (2016)

Chapter 3. Investigation on SPE of 3-dimensional amorphous alumina nanomembrane structure on c-plane sapphire substrate

3.1 Introduction

We have demonstrated that the CES scheme, incorporation of an α-Al_2O_3 nanomembrane cavity structure on a sapphire substrate (α-Al_2O_3), was an effective way to enhance the efficiency of GaN-based LEDs.[1-3] As discussed in **Chapter 2**, this scheme involved a formation of an amorphous alumina (Al_2O_3) nanomembrane structure and its solid phase epitaxial transformation into the α-phase. It was found that the wall-plug efficiency of LEDs deposited on the CES with hexagonally arrayed hemispherical cavities was improved by 9 % at a wavelength of 462 nm compared to that on a patterned sapphire substrate.[2] In addition, by using the CES with stripe-shaped cavity structure, GaN layer can be grown on a planar top layer of the stripe α-Al_2O_3 nanomembrane structure because the top layer parallel to c-plane of sapphire substrate provides c-plane α-Al_2O_3 surface. The ultra-thin α-Al_2O_3 nanomembrane can be acted as a compliant substrate and resultantly the GaN layer grown on the α-Al_2O_3 nanomembrane showed 28 % reduction of misfit dislocation density compared to that on a planar sapphire substrate.[3]

In the growth scheme using the CES, GaN layer is grown on a α-Al_2O_3 layer formed by solid-phase epitaxy (SPE) and resultantly crystalline quality of the GaN layer could be dependent on the characteristics of the SPE α-

Al_2O_3. Therefore, understanding the phase transformation of the 3-D alumina membrane structure is crucible to the quality improvement of the GaN layers on CES.

SPE of an amorphous alumina has been studied on an only thin film form to investigate the transition mechanism, kinetics, and doping effect.[4-9] The phase transformation of Al_2O_3 thin films from amorphous to γ-phase was observed in the temperature range above 700 ^oC and that from γ-phase to α-phase was observed in the higher temperature range than 800 ^oC since it required higher activation energy.[4-9] Thus, it was reported that during high temperature annealing SPE of amorphous Al_2O_3 on a sapphire substrate was preceded through two steps of amorphous to metastable γ-phase and then subsequently into α-phase.

In this research, we fabricated a stripe-shaped cavity amorphous Al_2O_3 nanomembrane structure on a sapphire substrate by ALD and performed thermal treatment to crystallize it into the single crystalline α-phase by SPE. The unique SPE behaviors of the long Al_2O_3 membrane forming a cavity, originated from its geometrical structure, were investigated in detail by TEM analysis. Furthermore, kinetics of SPE in ALD amorphous alumina layer was investigated by precisely measuring thickness of the epitaxially grown γ- and α-Al_2O_3 layer in TEM images.

3.2. Experimental details

For the investigation on the SPE of 3-D Al_2O_3 membrane structure, stripe-shaped amorphous Al_2O_3 membrane structure was fabricated on a sapphire substrate as shown in Fig. 4.8. An amorphous Al_2O_3 layer of an 104 nm thickness was deposited on sapphire substrates with a photoresist (PR) pattern of a stripe shape by ALD at 110 ^oC. Then the inside PR was removed by dipping the substrate in acetone, resulting in a stripe-shaped amorphous Al_2O_3 membrane structure on a sapphire substrate. For the crystallization of the amorphous Al_2O_3 membrane structure, the substrate was annealed in a furnace with ambient air in the temperature range from 747 to 1063 ^oC. The temperature was measured by a thermocouple located a few centimeters above the sample stage.

The phase transition of the Al_2O_3 membrane was investigated by TEM using JEM-2100F operated at 200 kV. The TEM specimens were prepared using a focused ion beam (FIB) system. Before the FIB process, carbon and Pt metal were deposited as a protective layer to prevent the surface damage from the incident Ga beam. X-ray reflectivity (XRR) curve was used to measure the density of amorphous Al_2O_3 layer by a PANalytical X'pert Pro XRD operated at 30 kV. In order to investigate the stress distribution in the Al_2O_3 membrane structure, finite element simulation was performed using a commercial software, ABAQUS.[10]

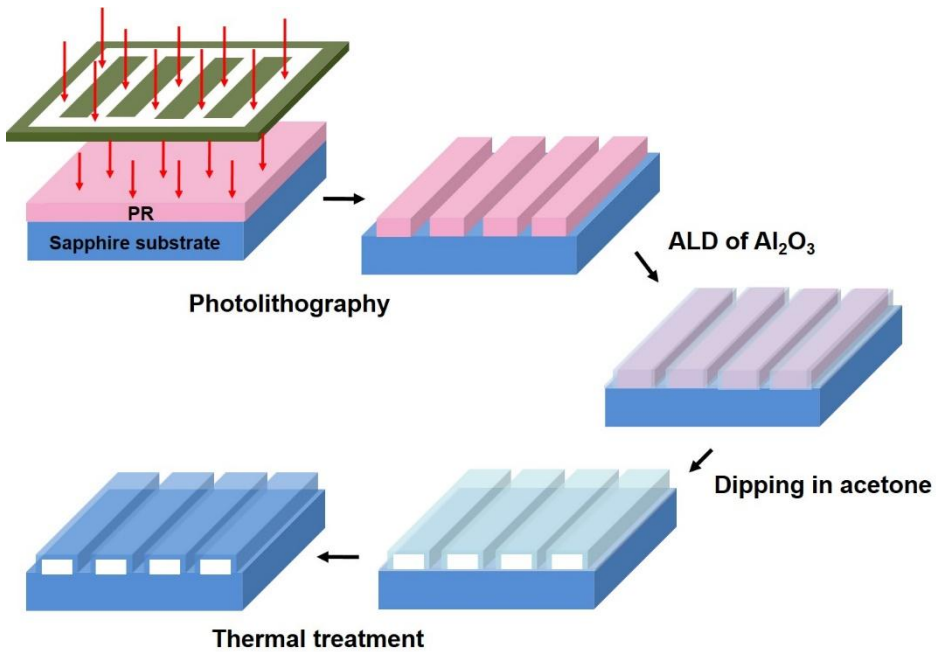

Figure 3.1 Schematic diagram for the fabrication of stripe-shaped amorphous Al_2O_3 membrane structure and subsequent its crystallization

3.3 Crystallization procedure of 3-D alumina nanomembrane structure

3.3.1 Phase transformation from amorphous to α-phase

Figure 3.2(a) and (b) show planar- and cross-sectional view SEM images of the amorphous Al_2O_3 layer consisting of the stripe-shaped cavity patterns of membrane and planar regions between the patterns after the PR removal. The stripe patterns were formed along the [11-20] direction of the sapphire substrate. The width, spacing, and height of the Al_2O_3 membrane pattern were 4 μm, 2 μm and 2 μm, respectively. The thickness of the Al_2O_3 membrane was 104 nm. TEM analysis confirmed that the phase of the Al_2O_3 layer was amorphous.

TEM analysis was performed for the Al_2O_3 membrane annealed at 777 ^oC to investigate the SPE from amorphous to γ-phase. Figure 3.3 shows the TEM image of the Al_2O_3 membrane, obtained at the [11-20] zone axis of the sapphire substrate, after annealing for 1 hr. It was found that oxide residues generated during the FIB process were accumulated inside the Al_2O_3 shell. While the shell membrane was remained as amorphous Al_2O_3 the phase transformation to γ-Al_2O_3 was observed to originate from the sapphire substrate as indicated by dotted line in the figure. In order to confirm the epitaxial relationship between the substrate (α-Al_2O_3) and γ-Al_2O_3, HRTEM image of the γ/α interface and fast Fourier transform (FFT) images of each

phase were obtained as shown in the inset of Fig. 3.3. The FFT image at the transformed layer corresponds to the electron diffraction pattern on the [11-2] zone axis of γ-Al_2O_3, presenting electron diffraction spots of the {311}, {440}, {220}, and {222} planes.[11] The FFT image of the sapphire substrate corresponds to the diffraction pattern of α-Al_2O_3 collected at the [11-20] zone axis.[12] [111] direction of the γ-Al_2O_3 obtained from the electron diffraction spot of (222) plane was parallel to the [0001] direction of the α-Al_2O_3 from the electron diffraction spot of (0006) plane, indicating the epitaxial phase transformation of the amorphous Al_2O_3 on the sapphire substrate to γ-Al_2O_3.[4]

To investigate the transformation procedure of γ-Al_2O_3, the annealing time was increased up to 4 hours. Figure 3.4(a) - (c) show the left corner region of the Al_2O_3 membrane after annealing for 1, 2 and 4 hrs, respectively. After 1 hr annealing, the thickness of the single crystalline γ- Al_2O_3 was 54 nm as shown in the Fig. 3.4(a). After 2 hrs annealing, as shown in Fig. 3.4(b), the α/γ interface was observed to move upward into the membrane with the complete phase transformation of the planar area between the patterns. It is worth noting that the nuclei of γ phase were observed in surface region of the remaining amorphous Al_2O_3 membrane as marked with arrows in the Fig. 3.4(b). This indicates that the nucleation process started after an annealing between 1 and 2 hrs because the nucleation process includes certain period of time, called incubation time, until a large cluster exceeding critical nucleus size forms.[13] The thickness of the γ-Al_2O_3 on the planar region was measured

to be 82 nm, which is 21 % thinner compared to 104 nm for the original amorphous layer. This reduction of the thickness could be attributed to the density increase of the Al_2O_3 layer during the phase transition for amorphous into γ crystalline phase. The impact of the density reduction during the phase transformation will be discussed later.

After 4 hrs annealing, it was confirmed that the whole ALD Al_2O_3 layer was completely transformed into γ phase. It consisted of the epitaxial area on top of the sapphire substrate and the polycrystalline γ-Al_2O_3 in the membrane shell, as shown in Fig. 3.4(c). The final interface between the epitaxial single crystalline γ-Al_2O_3 and the polycrystaline γ-Al_2O_3 was shown by the dash line. It is observed that the advancement of SPE γ-Al_2O_3 was not proceeded along the whole membrane shell but blocked by the formation of polycrystalline γ-Al_2O_3. The dash line indicates that the SPE γ-Al_2O_3 advanced less at the surface region of the membrane shell where the nuclei of γ phase formed firstly, compared to the center region of the membrane shell. G. L. Olson et al. reported that once polycrystalline phase having excess free energy caused by grain boundaries was formed, its transition to single crystalline phase could not be observed due to the exceedingly slow kinetic rate of the process.[13] It was also found that the progress of SPE γ-Al_2O_3 annealed for 4 hrs was almost the same as that annealed for 2 hrs as shown in Fig. 3.4(b) and (c). This indicates that the whole membrane shell was transformed into the polycrystalline phase at high speed as soon as the nuclei can be formed on the

free surface after the incubation time. This is because the thin (~100 nm) membrane structure has a high surface area and shortens the growth distance of nuclei formed at the surface. Figure 3.5 shows a selected area diffraction pattern (SADP) at the polycrystalline part of the Al_2O_3 membrane. The lattice plane spacings measured from the electron diffraction patterns were 1.12, 1.37, 1.95, and 2.26 Å, corresponding to the {444}, {440}, {400}, and {222} planes of γ-Al_2O_3, respectively.[11]

3.3.2 Phase transformation from γ- to α-phase

The γ to α phase transformation of the Al_2O_3 membrane was investigated in the higher annealing temperature range from 920 to 1063 ^oC. Figure 3.6(a) and (b) shows the corner area of the Al_2O_3 membrane where it was fixed to the sapphire substrate after annealing for 2 hrs at 920 and 970 ^oC, respectively. They show more favorable phase transformation to α-phase as a form of protrusion on the sapphire substrate, marked by the dash line in Fig. 3.6(a) and (b), in the corner area than other regions which was remained as γ-phase. FFT electron diffraction patterns from the transformed area, shown in the inset in Fig. 3.6(b), correspond to the diffraction spots of single crystalline α-Al_2O_3. It illustrated the same c-direction as the sapphire substrate, i.e., epitaxial phase transformation into the α-Al_2O_3 by SPE. The remaining

alumina layers had been completely transformed into γ-phase (SPE γ-Al_2O_3 for the planar region and polycrystalline γ-Al_2O_3 for the membrane region), indicating sufficiently fast transformation rate into the γ-phase in this annealing condition.

Figure 3.6(c) shows that the phase transformation preceded in the planar region and along the membrane wall after annealing at 1010 ^oC for 2 hrs. Advancement of the three different α/γ interfaces were indicated by the arrows. It is clear that the phase transformation was dominant from the corner area both in the lateral and the vertical directions compared to a significantly slow rate in the vertical direction in the planar region.

For the lateral SPE in the planar region, the stable facets with low surface energy such as {0001}, {11-20}, {1-102}, and {11-23} planes could be formed on a growing surface of Al_2O_3 layer [14]. Among them, the {1-102} r-planes, which is only a plane inclined along the <1-100> direction, the lateral direction in the planar region, was expected to appear on the SPE surface. In fact, by measuring its angle of ~57 ^{o} with respect to (0001) c-plane, the lateral γ/α interface was identified as {1-102} r-planes. It was reported that the SPE rate of Al_2O_3 was slower on the {0001} c-plane than that on the {11-20} a- and {1-102} r-planes.[8] This consistent with the result in Fig. 3.6(c) of the fast moving {1-102} r-planes and the somewhat small advancement of the {0001} c-plane.

In addition, it was observed that nanocrystalline γ-Al_2O_3 was formed on the surface of planar alumina layer between the patterns. This indicates that

in this annealing temperature, the nucleation rate of the γ-Al_2O_3 was sufficiently fast and therefore, the nucleation occurs on the surface before the planar region was epitaxially transformed into γ-Al_2O_3 by SPE. The formation polycrystalline intermediate γ-Al_2O_3 in the planar region may reduce the crystal quality of the subsequent α-Al_2O_3 layer. As discussed in **Chapter 2.5.2**, the number of nanopores was much higher in the cavity shell which was transformed from nanocrystalline γ-Al_2O_3 than in the planar region which was transformed from epitaxial γ-Al_2O_3. Accordingly, when fabricating the CES in which subsequent GaN epitaxial layer is grown on the planar region between the cavity patterns, the whole planar region should be epitaxially transformed into the intermediate γ-phase at a low temperature range, where the nucleation on the surface cannot occur, before the subsequent phase transformation into α-phase.

For the vertical SPE in the corner area, its much faster growth rate than that in the planar region could be attributed to the stresses induced by the structural contraction of the membrane structure during the crystallization. As shown in Fig. 3.7, a TEM image showing the whole membrane after annealing at 1010 ^oC for 2 hrs, the side walls were tilted inward and the roof was deflected in the middle, resulting in the contraction of the cavity, compared to Fig. 3.3. Table 1 shows the phases and dimensions of the Al_2O_3 membrane measured in the TEM images after the annealing at different conditions. Before annealing, the membrane wall was slightly tilted inward

due to the trapezoid-like initial PR shape. After the phase transition to γ, the inclined angles, defined as an angle between the sapphire surface normal and the membrane wall, were increased by 5 ^{o}, indicating a further inward bending. Compared to the initial amorphous Al_2O_3 membrane, the length of the membrane wall and the width of membrane roof was reduced by 9.1 % and 5.8 %, respectively. We believe that this reduction of the size was due to the density increase of the Al_2O_3 membrane during the phase transformation. It was reported that the densities of γ-, and α-Al_2O_3 were 3.61 ~ 3.67 and 3.99 g/cm^3, respectively[12, 14-16], and the density of amorphous Al_2O_3 was varied from 2.1 to 3.5 g/cm^3 depending on the deposition technique and condition.[17] The density of the amorphous Al_2O_3 deposited in this experiment was measured to be 2.81 g/cm^3 by X-ray reflectivity measurement. We speculate that the inward tilting of the side wall induced the compressive stress in the corner area on which it was fixed to the sapphire substrate as illustrated in Fig. 3.8. It was reported that for a SPE accompanying the volume contraction along the growth direction, compressive stress exerted in the growth direction enhanced the SPE rate.[18-20] Figure 3.9, plot for the SPE rate of amorphous Si vs. applied stress along the SPE direction, shows exponential increase of the SPE rate with the applied compressive stress along the SPE direction.[20] Because the phase transition from γ- to α-Al_2O_3 is also a volume reduction transition, the compressive stress along the vertical SPE direction induced after the phase transition from amorphous to γ-Al_2O_3 is expected to accelerate the subsequent phase transition to α-Al_2O_3 at the

corner region.

3.3.3 Fully crystallized α-Al_2O_3 nanomembrane structure by SPE

Figure 3.10(a) and (b) show the Al_2O_3 membranes annealed at 1063 ^oC for 1.5 and 2.5 hrs. With increasing the annealing time, the interface was observed to advance upward and then, laterally along the membrane roof as shown in Fig. 3.10(a). The inset in Fig. 3.10(a) is a TEM image of the interface at higher magnification revealing the clear contrast difference between α- and γ-Al_2O_3. Fig. 3.10(b) shows that the whole Al_2O_3 membrane was successfully transformed into single crystalline α-phase after 2.5 hrs of the annealing. It should be noted that, unlike the crystallization of γ-Al_2O_3 shown in Fig. 3.4, the SPE process into α-phase proceeded along the whole membrane structure without being interrupted by the random nucleation and growth of α-Al_2O_3 in the investigated annealing condition. This implies that for the phase transition from γ- to α-phase the energy barrier for the nucleation is much higher than that for the SPE. The higher activation energy of the random nucleation than the SPE is due to increase of surface energy after the phase transformation, which is negligible for the SPE.[22] Accordingly, the high energy barrier for the nucleation of α-Al_2O_3 could be attributed to high surface energy of the α-Al_2O_3, which is even higher than that of the γ-

Al_2O_3 although the α-Al_2O_3 is thermodynamically stable phase.[23-24] The increase in surface energy for the transition from γ- to α-Al_2O_3 increases maximum free energy of formation, an energy barrier term of the nucleation[22, 25], at the free surface of membrane, which is favorable site for the random nucleation as shown in Fig. 3.4(c). As a result, the absence of nucleation of α-Al_2O_3 in the annealing condition facilitates the fabrication of single crystalline α-Al_2O_3 nanomembrane structure on a sapphire substrate.

As shown in Table 1, after the complete phase transition from γ-phase to single crystalline α, the width of the membrane roof was reduced by ~9 % and the inclined angle was increased by 4.6 ^{o}. During the lateral SPE, the membrane roof is gradually contracted, thereby leading to the inward bending of the membrane wall and consequent downward deflection of the roof as observed in Fig. 3.10(a) and (b). It is worth noting that the more the wall was tilted inward, the more the roof was deflected downward, maintaining the angle between the membrane wall and the roof as indicated in Fig. 3.10(b). This could be because keeping the roof flat by increasing the angle required much more force than the deflection. As shown in the insets in Fig. 3.10(b) the FFT electron diffraction patterns revealed that c-direction of the roof area was rotated inward by ~ 4 ^{o} with respect to the sapphire substrate as a result of the deflection rather than step-wise surface keeping the c-direction in parallel to that of the substrate everywhere.

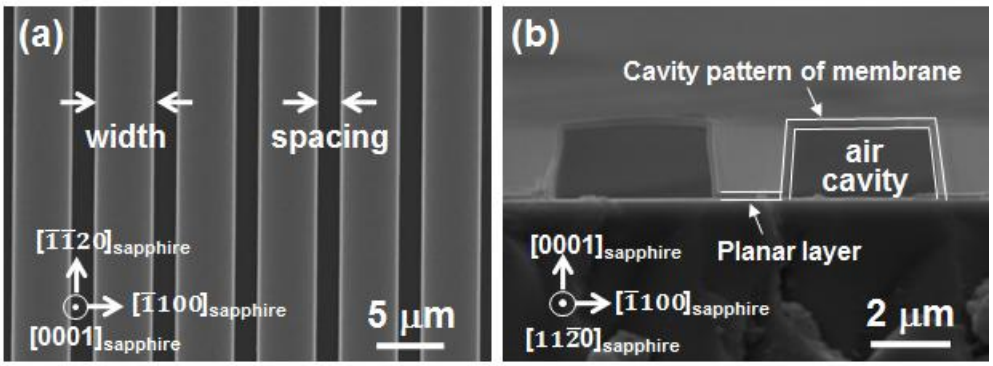

Figure 3.2 Plan-view (a) and cross-section (b) SEM images of the amorphous Al_2O_3 membrane.

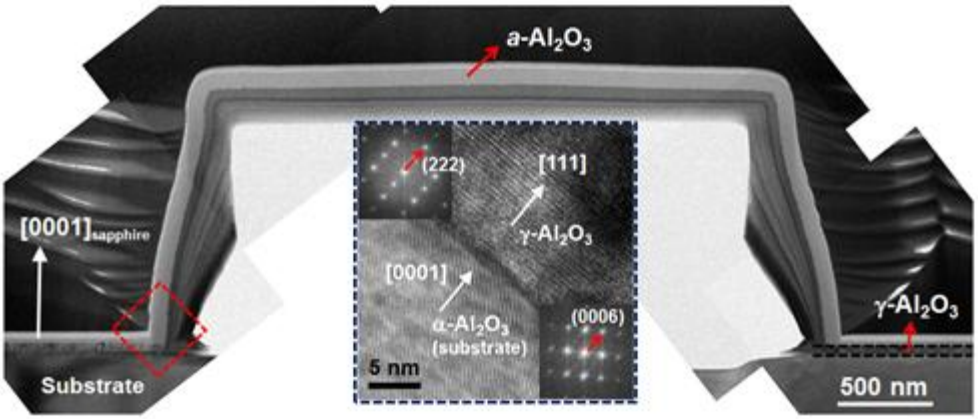

Figure 3.3 Cross-section TEM image of the Al_2O_3 membrane annealed at 776 ^oC for 1 hour. The inset on the left shows HR TEM image at the amorphous part of the membrane and its FFT image. The inset on the right shows HR TEM image at the interface between the substrate and γ-Al_2O_3 and their FFT images.

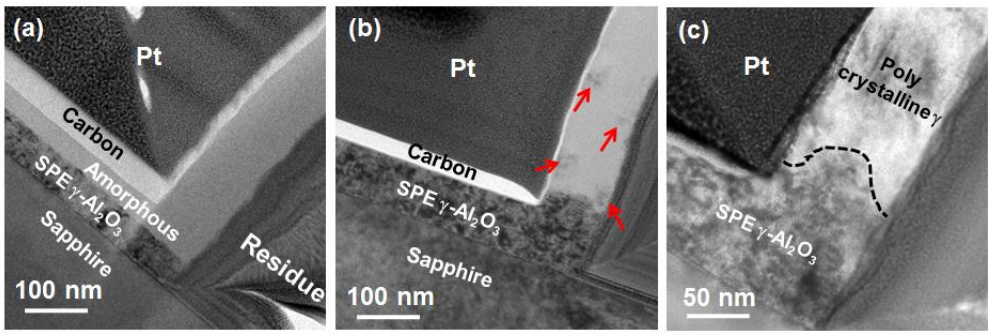

Figure 3.4 Left corner region of the Al_2O_3 membrane annealed at 776 ^oC for (a) 1 hour, (b) 2 hours, and (c) 4 hours.

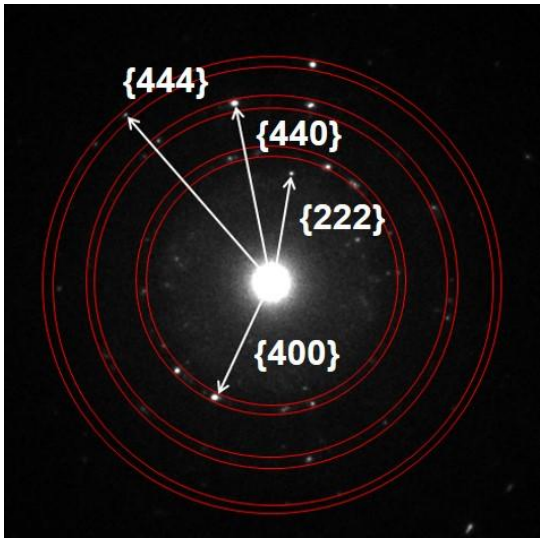

Figure 3.5 SADP at the nanocrystalline part of the Al_2O_3 membranes.

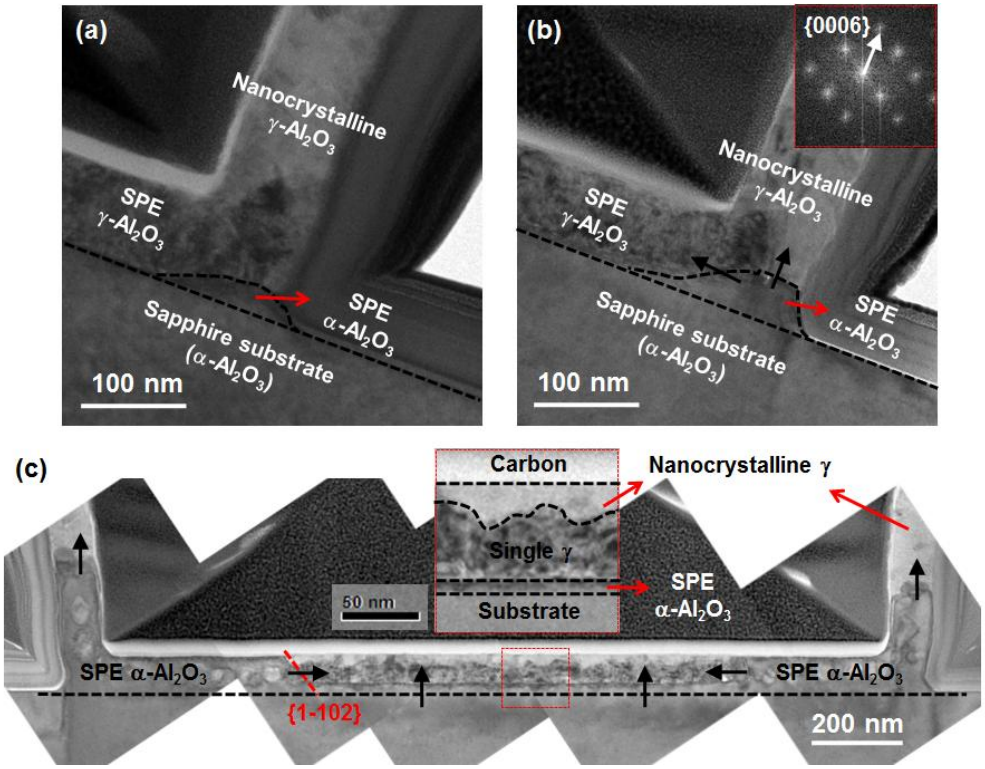

Figure 3.6 TEM images at the left corner region of the Al_2O_3 membrane annealed at (a) 920 ^oC and (b) 970 ^oC for 2 hrs. The inset in Fig. 3.6 (b) shows the FFT electron diffraction pattern of HR TEM image at the α-Al_2O_3 protrusion. (c) A TEM image at the planar area between the patterns for the Al_2O_3 membrane structure annealed at 1010 ^oC for 2 hrs.

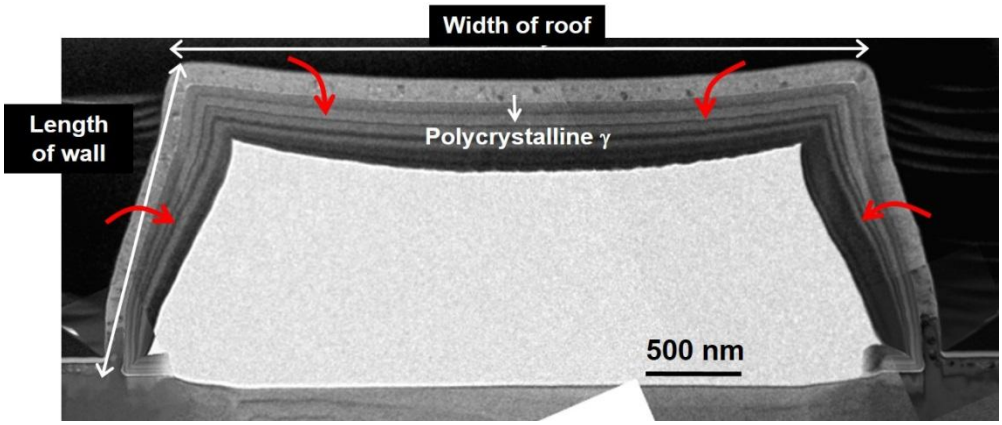

Figure 3.7 A cross-section TEM image of the whole Al_2O_3 membrane structure annealed at 1010 ^{o}C for 2 hrs.

Table 3.1 Phase and dimension of the Al_2O_3 membranes at varied annealing conditions. The inclined angle is defined as an angle between the surface normal to the substrate and the left membrane wall.

	Before annealing	776 °C 4 hrs	1063 °C 2.5 hrs
Phase of membrane shell	Amorphous	Polycrystalline γ	Single crystalline α
Width of membrane roof (μm)	3.94	3.71	3.45
Height of membrane wall (μm)	1.97	1.79	1.66
Inclined angle (°)	9.7	12.8	17.4

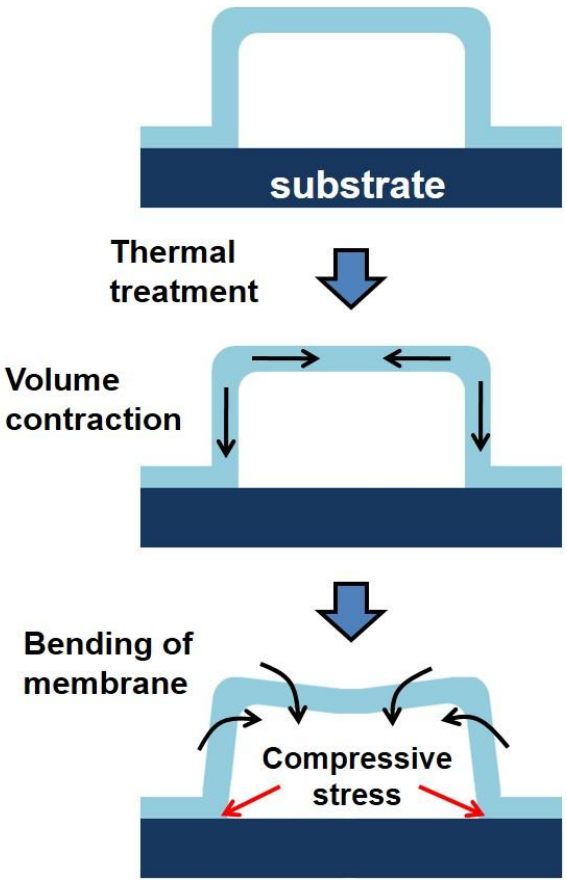

Figure 3.8 Schematic diagram of the volume-contraction induced bending of the Al_2O_3 membrane and consequently induced stresses and deflection.

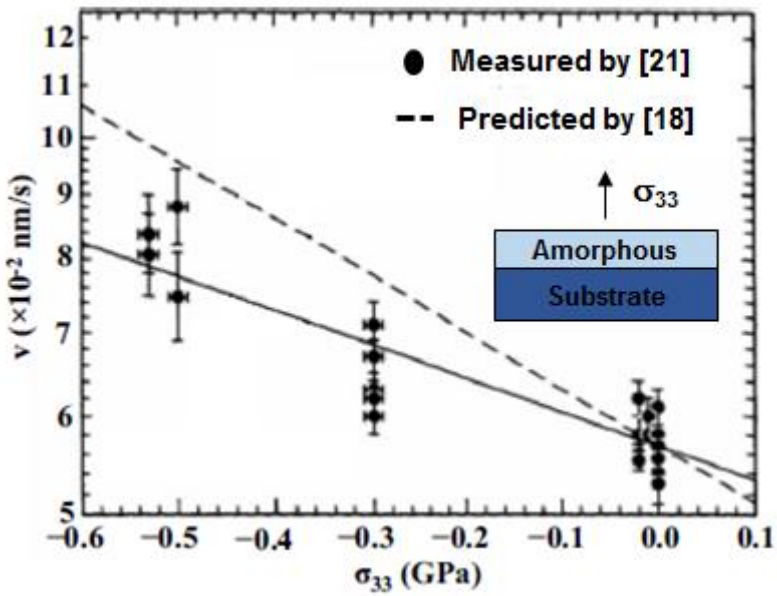

Figure 3.9 Plot for SPE rate of amorphous Si with applied stress along the SPE direction.[20]

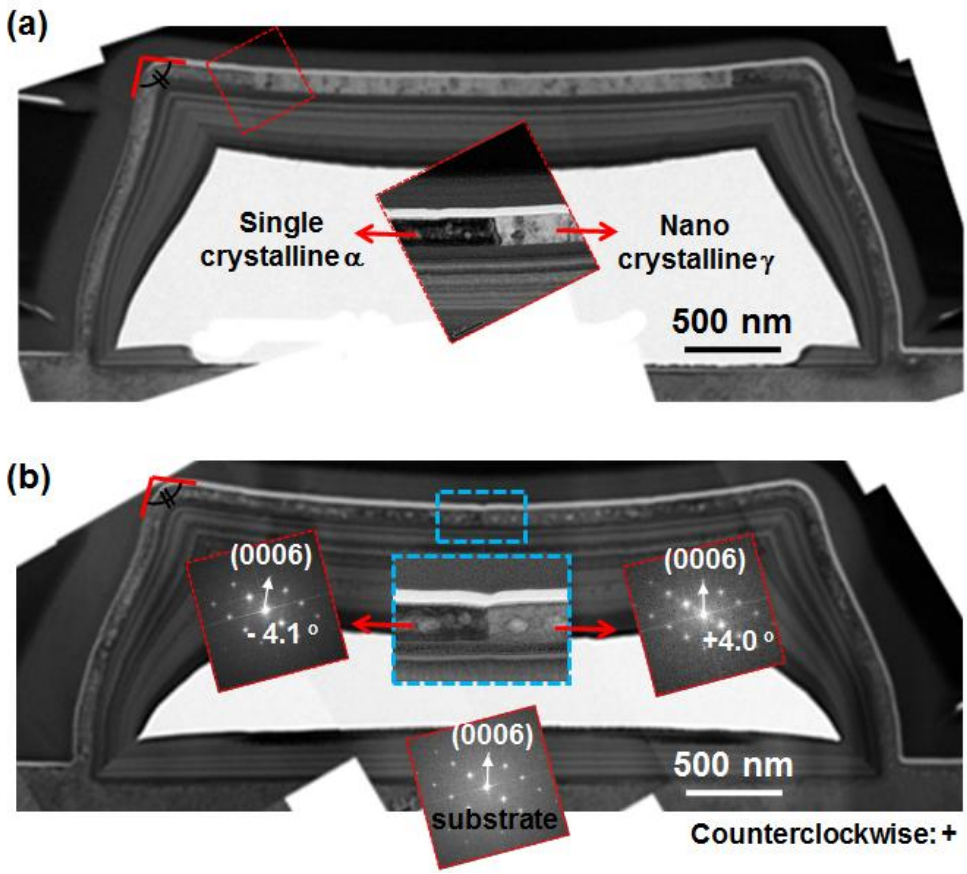

Figure 3.10 Cross-section TEM images of the whole Al_2O_3 membrane structure annealed at 1063 ^oC for 1.5 hours (a) and 2.5 hours (b). The inset in Fig. 3.10 (a) shows the magnified image at the interface between the single crystalline α-Al_2O_3 and the nanocrystalline γ-Al_2O_3 indicated by the red square. The insets in Fig. 3.10(b) are the magnified image at the center of the membrane roof and FFT electron diffraction patterns of α-Al_2O_3 at the membrane roof and substrate.

3.4 Finite element simulation for calculation of stress induced in 3-D alumina nanomembrane structure

In order to investigate the stresses induced by the volume contraction of the Al_2O_3 layer during the annealing, 2D finite element simulation was performed. For simplicity, the simulated structure was constructed assuming the volume contraction during the phase transformation from amorphous to γ phase. Dimension of the simulation structure was determined using the measured parameters of the amorphous Al_2O_3 membrane in Table 1. Mechanical properties of the membrane structure were obtained using the data for the amorphous Al_2O_3.[26] For the planar Al_2O_3 layer, anisotropic volume contraction of 21 % along the y-axis was assumed based on the thickness measurement of the SPE γ-Al_2O_3 layer shown in Fig. 3.4(b). This reduction corresponds to the density change from the our ALD amorphous Al_2O_3 (2.81 g/cm^3) to γ-Al_2O_3 (3.61 ~ 3.67 g/cm^3).[14-16] For the membrane shell, which experiences transformation into nanocrystalline phase, isotropic volume contraction was assumed to be 14 %. This value was estimated by 2D contraction corresponding to the 3D volume contraction of 21 %.

Figure 3.11 shows distribution of stress component along the y-axis, direction of the SPE, at the corner area in the Al_2O_3 membrane. The inset shows simulation model of the membrane structure before and after the volume contraction. It is found that the membrane wall bended inward after the volume contraction. It is clear that compressive stress was induced at bottom of the wall due to the pulling force applied to it as a result of the

volume contraction in the membrane roof. This induced compressive stress was expected to cause the favorable phase transformation in the y-direction into α-phase as shown in Fig. 3.6(a). Although the much higher stress is applied at the upper necking region, crystallization into α-phase is not favorable at that region because there is no crystalline seed.

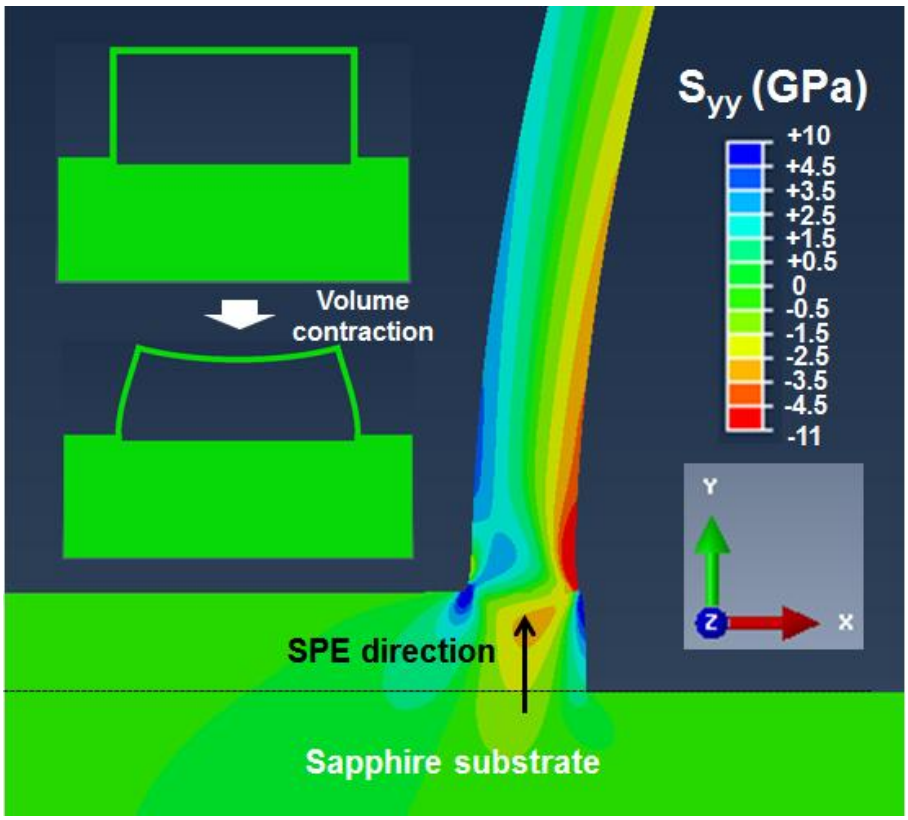

Figure 3.11 Stress component along the y-axis at the corner region of the simulation model. The insets in the figure show simulation model of the membrane structure before and after the volume contraction.

3.5 Kinetics in SPE of amorphous alumina layer

Figure 3.12 and 3.13 show the Arrhenius plot of the SPE rate from amorphous- to γ-Al_2O_3 and that from γ- to α-Al_2O_3, respectively, in the planar layer between patterns. In order to obtain the SPE rate, thickness of the SPE γ- and α-Al_2O_3 layers was measured in TEM images and divided by annealing time. For the γ-Al_2O_3 layer, thickness from the interface with sapphire substrate to the surface of γ-Al_2O_3 was measured in the surface normal direction of the substrate. For accurate measurement, the thickness at the planar region was measured at 10 nm interval. For the α-Al_2O_3 layer, the thickness from the extension line of the initial sapphire surface (as marked by dotted line in Fig. 3.6(c)) to the α/γ growth front was measured in the same manner. In fact, variations in the thickness of the γ- and α-Al_2O_3 was found, indicating that the SPE rate varied with location. When determining the SPE rate to α-phase, the time for phase transformation to γ-phase was neglected because the SPE rate from amorphous to γ-phase is much faster than that from γ- to α-phase (more than 3 order of magnitude as inferred from Fig. 3.12 and 3.13) in the temperature range where the γ to α SPE can occur. Therefore, the γ-Al_2O_3 would be already formed at the growth front when the SPE into α-Al_2O_3 begins. From the fitted line using the Arrhenius equation, v

= $v_0 \exp(-E_a/kT)$, activation energies for the SPE from amorphous to γ-phase and that from γ- to α-phase were calculated to be 3.1 eV and 3.9 eV, respectively, showing that the activation energy for the SPE from γ- to α-phase is higher than that from amorphous to γ-phase. The previously reported results of the SPE rate and the activation energies in amorphous Al_2O_3 thin films formed by ion implantation and e-beam evaporation are also shown in Fig. 3.12 and Fig. 3.13. The activation energies were different from the values reported by other researchers and the reported values were also different from each other.[4-9] The reason for the variations in the SPE rate and activation energy is not clear but it is speculated that different structural properties and impurities of the amorphous alumina layers attribute to the variations. Structural properties of Al_2O_3, such as atomic bond length and coordination number of atoms, have different values as the density of Al_2O_3[17], which is varied depending on the formation method and condition.[17, 27-29] The difference in structural properties presumably could affect energy barrier for the atomic migration of Al and O ions in alumina layer. It was noted that the variations in SPE rate is much higher for the phase transformation from amorphous to γ-phase than that from γ- to α-phase as shown in Fig. 3.12 and Fig. 3.13. This may implies that the effect of structural properties on the SPE is expected to be higher in the phase transformation from amorphous to γ-phase because the crystal structure of γ-phase is identical regardless of the initial structural properties of amorphous Al_2O_3. For the SPE from γ- to α-

phase shown in Fig. 3.13, activation energy of 3.9 eV obtained in this experiment is more comparable to that reported by White et al, in which the SPE rate was calculated by TEM measurement. In comparison, the results from reported by McCallum et al. and Simpson et al., in which the SPE rate was measured by time-resolved reflectivity show similar activation energy value of ~ 5.2 eV. This indicates that the SPE rate may vary depending on the measurement methods. The TEM analysis has the advantage that it can precisely measure thickness of the transformed layer by SPE while observing in image. Thus, site specific analysis is possible in the TEM measurement and resultantly the variation of SPE rate depending on the position could be considered by averaging the data. However, variations in the SPE rate cannot be accounted for in the reflectivity measurement.

It was also found that for the ALD Al_2O_3 used in this experiment, the SPE rate for both transition from amorphous- to γ-phase and from γ- to α-phase was slower compared to the amorphous Al_2O_3 layers formed by e-beam evaporation and ion-implantation. It was known that the non-dopant impurities, such as hydrogen, nitrogen, and carbon, retard the SPE rate by interfering the atomic migrations at the SPE interface.[20, 30] In the case of ALD, the hydrogen impurity can be introduced in the Al_2O_3 layer due to the incomplete reaction of Al-OH surface species groups with trimethylaluminum precursors[31], whereas for the Al_2O_3 layers formed by e-beam evaporation or ion implantation, the hydrogen could be only introduced by the residuals from background in high vacuum chamber.[32] The concentration of hydrogen impurity in the ALD Al_2O_3 is known to be increased with decreasing the deposition temperature.[31] In this experiment, the ALD was performed at a low temperature of 110 ^{o}C and it was reported

that high concentration of hydrogen impurities greater than 10 at. % was incorporated in the Al_2O_3 layers at this deposition temperature.[31] It is speculated that this high concentration of hydrogen impurity in the ALD Al_2O_3 may reduce the SPE rate.

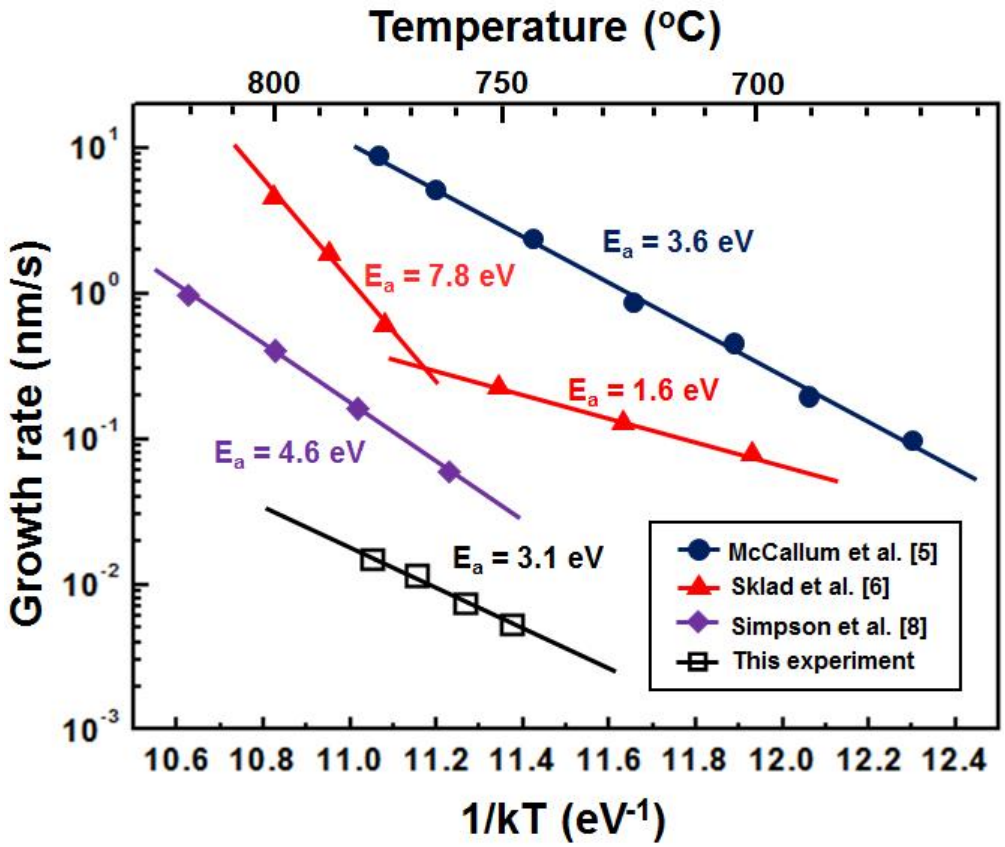

Figure 3.12 Arrhenius plot of the SPE rate from amorphous to γ-phase in the planar region between patterns. For comparison, the kinetics results reported by other researchers are also shown in the figure.

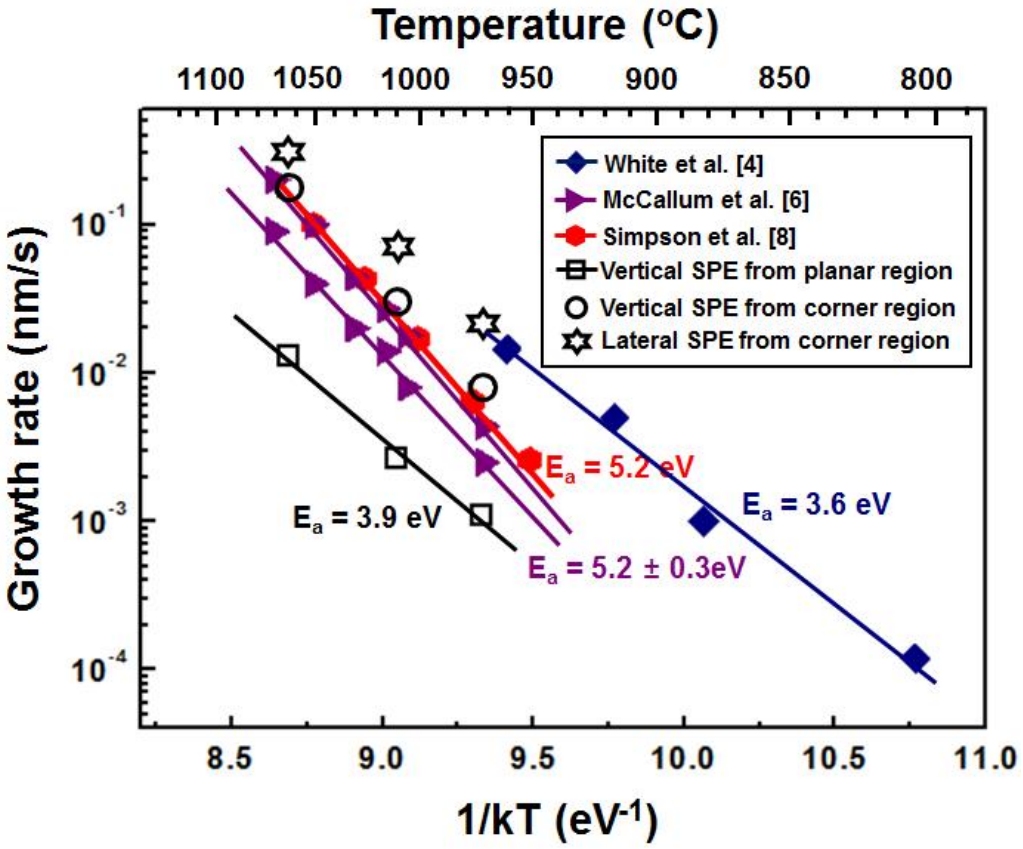

Figure 3.13 Arrhenius plot of the SPE rate from γ-phase to α-phase in the planar region between the patterns. The rates for the vertical and lateral SPE from the corner region are also presented. For comparison, the kinetics results reported by other researchers are also shown in the figure.

3.6 Summary

SPE behavior of a cavity-shaped amorphous Al_2O_3 membrane on a sapphire substrate was investigated using transmission electron microscope analysis. The SPE process occurred through 2 stages of the phase transformation from amorphous to γ-Al_2O_3 and subsequently to α-Al_2O_3. At 777 ^oC SPE of γ-Al_2O_3 was initiated from the interface between amorphous Al_2O_3 and sapphire substrate with a relationship of $[0001]_{sub}//[111]_{\gamma\text{-}Al2O3}$. Beside SPE, it was observed that nanocrystalline γ-Al_2O_3 were formed in the upper part of the membrane. The ensuing phase transition of the Al_2O_3 membrane from γ to α was observed at a higher temperature range above 920 ^oC. The SPE of α-Al_2O_3 begins at the corner region of the membrane and proceeds along the whole membrane. During the SPE from γ- to α-phase, random nucleation was not observed in our investigation condition. As a result, after annealing at 1063 ^oC for 2.5 hours, the whole Al_2O_3 membrane was successfully transformed into single crystalline α-Al_2O_3. During the amorphous to crystalline phase transformations, volume of the Al_2O_3 membrane was contracted by the density increase, which induces stresses and deflections in the Al_2O_3 membrane structure. These result in the enhanced SPE at the corner region of the membrane structure and rotation of c-axis in the top layer of the membrane structure with respect to the sapphire substrate. Furthermore, the activation energies for the SPE procedure from amorphous

to γ-phase and that from γ- to α-phase were obtained as 3.1 eV and 3.9 eV, respectively, by precise measurement of the SPE rate using TEM measurement.

3.7 Bibliography

1. Jeonghwan Jang, Daeyoung Moon, Hyo-Jeong Lee, Donghyun Lee, Daehan Choi, Dukkyu Bae, Hwankuk Yuh, Youngboo Moon, Yongjo Park, Euijoon Yoon, Incorporation of air-cavity into sapphire substrate and its effect on GaN growth and optical properties, Journal of Crystal Growth **430**, 41–45 (2015)

2. Yoon-Jong Moon, Daeyoung Moon, Jeonghwan Jang, Jin-Young Na, Jung-Hwan Song, Min-Kyo Seo, Sunghee Kim, Dukkyu Bae, Eun Hyun Park, Yongjo Park, Sun-Kyung Kim, and Euijoon Yoon, Microstructured Air Cavities as High-Index Contrast Substrates with Strong Diffraction for Light-Emitting Diodes, Nano Letters (2016)

3. Daeyoung Moon, Jeonghwan Jang, Daehan Choi, In-Su Shin, Donghyun Lee, Dukkyu Bae, Yongjo Park, and Euijoon Yoon, An ultra-thin compliant sapphire membrane for the growth of less strained, less defective GaN, Journal of Crystal Growth **441**, 52-57 (2016)

4. C.W. White, L. A. Boatner, P. S. Sklad, C. J. McHargue, and M. J. Aziz, Ion implantation of crystalline oxides and ceramics, Nuclear Instruments and Methods in Physics Research B **32**, 11-22 (1988)

5. P.S. Sklad, J.C. McCallum, C.J. McHargue, and C.W. White, The amorphous-to-gamma transformation in ion implanted Al_2O_3, Nuclear Instruments and Methods in Physics Research B **46**, 102-106 (1990)

6. J.C. McCallum, T.W. Simpson, and I.V. Mitchell, Time resolved reflectivity measurements of the amorphous-to-gamma and gamma-to-alpha phase transitions in ion-implanted Al_2O_3, Nuclear Instruments and Methods

in Physics Research B **91**, 60-62 (1994)

7. D.R. Clarke, Epitaxial phase transformations in aluminium oxide, phys. stat. sol. (a) **166**, 183 (1998)

8. Todd W. Simpson, Qingzhe Wen, Ning Yu, and David R. Clarke, Kinetics of the amorphous → γ → α transformation in aluminium oxide: Effect of crystallographic orientation, Journal of American ceramics society, **81** [1] 61-66 (1998)

9. Ning Yu, Todd W. Simpson, Paul C. Mclntyre, Michael Nastasi, and Ian V. Mitchell, Doping effects on the kinetics of solid-phase epitaxial growth of amorphous alumina thin films on sapphire, Appl. Phys. Lett. **67** (7) (1995)

10. H. D. Hibbitt, ABAQUS/EPGEN- A general purpose finite element code with emphasis on nonlinear applications. Nucl. Eng. Des **77**, 271–297 (1984)

11. International Centre for Diffraction Data, PDF Number: 00-056-0457 (2014)

12. International Centre for Diffraction Data, PDF Number: 00-046-1212 (2012)

13. G. L. Olson and J. A. Roth, Kinetics of solid phase crystallization in amorphous silicon, Materials Science Reports **3**, 1-78 (1988)

14. Raquel Lizárraga, Erik Holmström, Stephen C. Parker, and Corinne Arrouvel, Structural characterization of amorphous alumina and its polymorphs from first-principles XPS and NMR calculations, *Phys. Rev. B **83**, 094201 (2011)*

15. Tania M. H. Costa, Márcia R. Gallas, Edilson V. Benvenutti, and João A. H. da Jornada, Study of Nanocrystalline γ-Al_2O_3 Produced by High-Pressure Compaction, J. Phys. Chem. B **103**, 4278–4284 (1999)

16. F. W. Dynys and J. W. Halloran, Alpha Alumina Formation in Alum-Derived Gamma Alumina, *J. Am. Ceram. Soc.* ***65****, 442–448 (1982)*

17. Raquel Liz´arraga, Erik Holmstr¨om, Stephen C. Parker, and Corinne Arrouvel, Structural characterization of amorphous alumina and its polymorphs from first-principles XPS and NMR calculations, Phys. Rev. B **83**, 094201 (2011)

18 Michael J. Aziz, Paul C. Sabin, and Guo-Quan Lu, The activation strain tensor: Nonhydrostatic stress effects on crystal-growth kinetics, Phys. Rev. B **44** (18), 9812-9816 (1991)

19. N. G. Rudawski, K. N. Siebein, and K. S. Jones, Effect of uniaxial stress on solid phase epitaxy in patterned Si wafers, Appl. Phys. Lett. **89**, 082107 (2006)

20. N.G. Rudawski, K.S. Jones, and R. Gwilliam, Stressed solid-phase epitaxial growth of ion-implanted amorphous silicon, Materials Science and Engineering R 61, 40–58 (2008)

21. W. Barvosa-Carter, PhD Thesis (1997)

22. R. B. Iverson and R. Reif, Recrystallization of amorphized polycrystalline silicon films on SiO_2: Temperature dependence of the crystallization parameters, J. Appl. Phys **62**, 1675-1681 (1987)

23. J. M. McHale, A. Auroux, A. J. Perrotta, A. Navrotsky, Surface Energies and Thermodynamic Phase Stability in Nanocrystalline Aluminas, Science **277**, 788-791 (1997)

24. Amir H. Tavakoli, Pardha Saradhi Maram, Scarlett J. Widgeon, Jorgen Rufner, Klaus van Benthem, Sergey Ushakov, Sabyasachi Sen, and Alexandra Navrotsky, Amorphous Alumina Nanoparticles: Structure, Surface Energy,

and Thermodynamic Phase Stability, J. Phys. Chem. C **117**, 17123−17130 (2013)

25. D. A. Porter and K. E. Easterling, Phase transformations in Metals and alloys, CRC press, p. 265-278 (2004)

26. Marie K. Tripp, Christoph Stampfer, David C. Miller, Thomas Helbling, Cari F. Herrmann, Christofer Hierold, Ken Gall, Steven M. George, Victor M. Bright, The mechanical properties of atomic layer deposited alumina for use in micro- and nano-electromechanical systems, Sensors and Actuators **A 130–131**, 419–429 (2006)

27. C. S. Bhatia, G. Guthmiller, and A. M. Spool, Alumina films by sputter deposition with Ar/O_2: Preparation and characterization, J. Vac. Sci. Technol. A **7**, 1298-1302 (1989).

28. Kari Koski, Jorma Holsa, and Pierre Juliet, Properties of alumina oxide thin films deposited by reactive magnetron sputtering, Thin Solid Films **339**, 240-248 (1999).

29. M. D. Groner, F. H. Fabreguette, J. W. Elam, and S. M. George, Low-temperature Al2O3 atomic layer deposition, Chem. Mater. **16**, 639-645 (2004)

30. B.C.Johnson, P.Caradonna, D.J.Pyke, J.C.McCallum, and P.Gortmaker, Hydrogen in amorphous Si and Ge during solid phase epitaxy, Thin solid films. **518**, 2317-2322 (2010)

31. M. D. Groner, F. H. Fabreguette, J. W. Elam, and S. M. George, Low-Temperature Al_2O_3 Atomic Layer Deposition*Chem. Mater.* ***16****, 639-645 (2004)*

32. V. Cimalla, M. Baeumler, L. Kirste, M. Prescher, B. Christian, T. Passow, F. Benkhelifa, F. Bernhardt, G. Eichapfel, M. Himmerlich, S. Krischok, J. Pezoldt, Densification of Thin Aluminum Oxide Films by Thermal

Treatments, Materials Sciences and Applications 5, 628-638 (2014)

Chapter 4. Investigation on stacking-mismatched domain structure of γ-Al_2O_3 layer formed on c-plane sapphire substrate by solid-phase epitaxy

4.1 Introduction

Solid-phase epitaxy (SPE) is solid-state phase transition of a metastable amorphous material to a crystalline phase, of which the fine structure is dominated by crystal structure and orientation of an underlying single crystalline substrate template.[1] The SPE has been considered as an important technique especially in Si-based device fabrications, for realization of silicon-on-insulator structures[2-3] and electrical activation for dopants in as-deposited layer.[4] For the CES scheme, the SPE method facilitated incorporation of air cavities between a conventional c-plane sapphire substrate and the overlying three-dimensional SPE α-Al_2O_3 nanomembrane that acted as the seed for GaN epitaxial layer grown on it, which contributed to the significant improvement of light output power of GaN-based LED.[5-6] Given a direct correlation between the crystalline quality of the epitaxial layer and its underlying seed layer, the LED performance can be even further enhanced by the better quality of the SPE α-Al_2O_3 nanomembrane layer, which arouses the importance of the fundamental understanding on the SPE mechanism. In addition, a previous report stated the dependence of fracture strength of the SPE α-Al_2O_3 layer on nanopores inside also supports that the SPE

mechanism should be profoundly understood for precise control of the epitaxial layers during the SPE procedure.[7]

As previously discussed in **Chapter 1.6** and **Chapter 3**, it was found that SPE of the amorphous Al_2O_3 layer occurs in two-step phase transformation from amorphous to metastable γ-phase (above 700 ^oC) and then subsequently to α-phase (above 800 ^oC) [8-13], the only thermodynamically stable phase of Al_2O_3[14], during high temperature annealing, due to the much faster growth rate of the phase transformation from amorphous to γ-Al_2O_3 than γ- to α-Al_2O_3. Accordingly, it is important to comprehend the formation mechanism of the intermediate γ-Al_2O_3 phase for the better crystalline quality of the following α-Al_2O_3 phase. In a previous paper, the existence of stacking-mismatched domains, i.e. mirror symmetric grains grown on the substrate resulted from two different atomic stacking sequences of a specific phase of materials (e.g. ABCABC··· and ACBACB··· stacking sequences), was reported in the SPE γ-Al_2O_3 layer on a (0001) sapphire substrate, which was demonstrated by two different nano-beam electron diffraction (NBD) patterns.[9] The formation of the stacking-mismatched domains of the γ-Al_2O_3 layer during the SPE procedure may include lots of information on the SPE mechanism, however, a mere detection of the two different electron diffraction patterns was insufficient to further interpret the epitaxial growth mechanism.

In this study, we investigated the formation of the intermediate γ-Al_2O_3

layer, epitaxially grown by SPE from amorphous Al_2O_3 layer on a $(0001)_\alpha$ sapphire substrate, by transmission electron microscopy (TEM) and computational calculations based on density functional theory (DFT) to deeply understand the SPE mechanism of Al_2O_3 material. By applying an advanced scanning NBD technique of TEM, we clearly visualized the phase/orientation relationship of the SPE γ-Al_2O_3 layer and the sapphire substrate. The stacking-mismatched domains of γ-Al_2O_3 were evidently revealed, however, distinguishable only at the particular projecting direction; it provides cautions for the analysis of the γ-Al_2O_3 layer, stacking-mismatched domains in particular. More importantly, the distribution the double-positioning domains in the SPE γ-Al_2O_3 layer helped to understand how the SPE growth occurs. We found that the nucleation and the stacking of the SPE γ-Al_2O_3 layers are strongly influenced by at least two stacking steps of oxygen-ion layers of the sapphire substrate near the interface, which corrects the misunderstanding on the SPE growth dynamics of the Al_2O_3 material.[9] This fundamental but significant information on the SPE growth dynamics may provide insights into the improvement direction for achieving greater properties of the SPE grown materials.

4.2 Experimental details

Amorphous alumina (Al_2O_3) layer was formed on a c-plane sapphire substrate by atomic layer deposition (ALD). Trimethylaluminum and H_2O were used as aluminum and oxygen sources, respectively. The ALD process was performed at 110 ^oC for 1000 cycles, corresponding to ~80 nm thick alumina film. For the phase transition from amorphous to γ-phase, thermal treatment was performed in an air ambient furnace at 850 ^oC for 1 hr. The samples were loaded at room temperature and then the temperature was increased with a rate of 5 ^oC/min. The TEM specimens were prepared using a focused ion beam (FIB) system. The phase/orientation mapping was performed by scanning nanobeam precession electron diffraction (NPED) technique, which was programmed by ASTAR device (NanoMEGAS) equipped with a TEM instrument (JEM-2100F, JEOL, 200kV). The scanning NPED patterns were obtained at the electron beam size below 1 nm and the scanning step size of 1 nm. A kinematical electron diffraction pattern simulation was conducted by JEMS code.

4.3 TEM analysis on the SPE γ-Al_2O_3 layer

4.3.1 Phase/orientation mapping of SPE γ-Al_2O_3 layer

To understand the SPE mechanism, we performed phase/orientation mapping for the intermediate state of the SPE Al_2O_3 layer, i.e. γ-Al_2O_3, on an $(0001)_\alpha$ sapphire substrate (α-Al_2O_3), which was annealed at 850 ^oC for 1 hr. Figure 4.1(a) shows a cross-sectional virtual bright-field image of the Al_2O_3 layer in the intermediate state viewed at $<10\text{-}10>_\alpha$ projection of the sapphire substrate. The virtual bright-field image was produced from transmitted beam intensity of scanned NPED patterns, which was obtained by the ASTAR device. It clearly shows the flat surface of the annealed Al_2O_3 with thickness of ~63 nm. Fig. 4.1(b), (d) – (f) show color-coded crystallographic phase/orientation maps of the area corresponding to Fig. 4.1(a), which were also derived from the scanned NPED patterns. The phase map in Fig. 4.1(b) confirms the γ- phase of the annealed Al_2O_3 layer on the sapphire substrate. A few points indexed as α-Al_2O_3 in the γ-Al_2O_3 layer are indexing errors, attributed to the overlap of two different NPED patterns at domain boundaries, which will be discussed below. Crystal orientation maps in Fig. 4.1(d) – (f) show the orientation of lattice planes normal to *x*-, *y*-, and *z*-axes, respectively. The axes are indicated in each figure and the color codes are described in Fig. 4.1(c). As shown with a uniform green color in Fig. 4.1(f), the SPE γ-Al_2O_3 layer is aligned along $<110>_\gamma$ projection at $<10\text{-}10>_\alpha$

projecting direction of the sapphire substrate, which makes the γ-Al_2O_3 layer seem single-crystalline. However, interestingly, it was revealed that the SPE γ-Al_2O_3 consists of two species of domains mostly repeated at ~100 nm intervals, as separated into two colors and labeled as I/II in the crystallographic orientation maps along the *x*- and *y*-axes (Fig. 1(d) and (e)), the so-called double-positioning domains observed in certain epitaxially grown cubic materials, e.g. Au, GaN, 3C-SiC, etc.[15-17]

The detailed orientation relationship between two domains can be explained from NPED patterns as shown in Fig. 4.1(g) – (i). Figure 4.1(i) shows the conventional diffraction pattern of the sapphire substrate where $(0001)_\alpha$ planes are aligned along the out of plane (vertical) direction. Fig. 4.1(g) and (h) present the NPED patterns from Domains I and II of the γ-Al_2O_3 layer, respectively, which are indicated in Fig. 4.1(d) and (e). As shown in the figures, the two NPED patterns are in a symmetrical relationship with the virtual vertical line as the symmetry axis, which implies that Domains I and II form twin structure. The NPED pattern of Domain I (Fig. 4.1(g)) is arrayed along $[110]_\gamma$ projection, whereas $[-1-10]_\gamma$ projection for Domain II (Fig. 4.1(h)). The twin structure of two Domains can be well recognized by the mirror symmetry of representative diffraction spots marked in the NPED patterns, e.g. diffraction spots from (4-44), (2-2-4), (4-40), (00-4) planes. The diffraction spots of (00-4) and (4-40) planes from Domain II (Fig. 4.1 (h)) are positioned on the *x*- and *y*-axes of the crystal orientation maps (Fig. 4.1(d) and (e)), respectively; it explains the origin of red and green

colors of Domain II in the crystal orientation maps (Fig. 4.1(d) and (e)), which represent $<001>_{\gamma}$ and $<110>_{\gamma}$, each. According to the twin relationship, (-442) and (2-28) diffraction spots are on the *x*- and *y*-axes in Domain I, which therefore result in different colors of Domain I and II in the crystal orientation maps. On the other hand, two Domains share same planes along horizontal and vertical axes, e.g. (4-44) and (2-2-4) planes, due to the twin symmetry as marked in the NPED patterns of Fig. 1(g) and (h). Accordingly, the crystal orientation maps for the horizontal and the vertical axes would show the uniform single colors in the γ-Al_2O_3 layer like Fig. 4.1(f); they cannot distinguish the Domains I and II. It shows the importance of the axes setting in the crystal orientation maps for discerning the double-positioning domains.

In addition, we obtained the color-coded crystallographic orientation maps for the SPE γ-Al_2O_3 at an $<1\text{-}210>_{\alpha}$ projection ($<112>_{\gamma}$ projection) as shown in Fig. 4.2(a) – (c), which are corresponding to side views of Fig. 4.1(g) – (i). Notably, the orientation maps along the *x*-, *y*-, and *z*-axes showed uniform single orientation of the SPE γ-Al_2O_3 because all of the NPED patterns were identical in the whole SPE γ-Al_2O_3 layer, implying that the domains cannot be distinguished in this projection. From the indexed orientations of the γ- and α-Al_2O_3 along the x-, y-, and z-axes, epitaxial relationship between them was confirmed to be $\{111\}_{\gamma}//\{0001\}_{\alpha}$, $<110>_{\gamma}//<10\text{-}10>_{\alpha}$, and $<112>_{\gamma}//<1\text{-}210>_{\alpha}$. This is consistent with the previously reported results from ion-

implanted and e-beam evaporated amorphous Al_2O_3 layer.[8-12] The TEM orientation mapping results indicate that the intermediate SPE γ-Al_2O_3 layer is formed with the epitaxial relationship but with several twin symmetric domains, which can be only distinguished at specific directions as shown in Fig. 4.1(d) and (e).

4.3.2 Selected area diffraction pattern and dark field image analysis

Figure 4.3 shows the electron diffraction patterns originating from the stacking-mismatched domains of γ-Al_2O_3 layer. An experimental selected area electron diffraction (SAED) pattern obtained from $<110>_\gamma$, i.e. the projecting direction in Fig. 4.1, and a corresponding simulated SAED pattern are shown in Fig. 4.3(a) and (b), respectively. Mixture of two γ-Al_2O_3 twin crystal models was used for the kinematical SAED pattern simulation (Fig. 4.3(b)). As shown in Fig. 4.3(b), various additional diffraction spots were created by double diffractions from two mixed crystals. The excellent fit between the experimental and the simulated SAED patterns confirms the formation of plentiful double-positioning γ-Al_2O_3 domains during SPE procedure. The electron diffraction spots from (-442)/(2-28) planes of Domain I and (00-4)/(4-40) planes of Domain II in Fig. 4.1 are marked in the simulated pattern (Fig. 4.3(b)) to describe relations between the NPED (Fig.

4.1 (g) and (h)) and the SAED (Fig. 4.3(a)) patterns. It also confirms that $(-442)_I/(00-4)_{II}$ and $(2-28)_I/(4-40)_{II}$ diffraction spots are located in the same directions from the transmitted center beam, i.e. *x*- and *y*-axes for crystal orientation maps in Fig. 4.1.

On the other hand, fewer diffraction spots are observed in the SAED pattern of Fig. 4.3(c) because the stacking-mismatched domains are indistinguishable at the $<112>_\gamma$ projection as already shown in the crystal orientation maps in Fig. 4.2. Diffraction planes indicated in the simulated SAED pattern (Fig. 4.3(d)) show the perfect overlaps of family planes from Domains I and II. The orientation maps and SAED patterns from different projecting directions imply that the projecting direction should be properly chosen to examine the existence of double-positioning domains, which can be easily neglected.

The stacking-mismatched domains of SPE γ-Al_2O_3 layer was also confirmed by dark-field (DF) image analysis. Figure 4.4(a) shows bright-field TEM image of the SPE γ-Al_2O_3 layer, presenting the image contrast in the epitaxial layer due to diffraction from the mixture of two kinds of domains. In order to confirm the existence of domains in image, DF images corresponding to the {004} diffractions from Domain I and Domain II in the SADP of the epitaxial layer (Fig. 4.4(b)) were obtained. Fig. 4.4(c) and (d) show the DF images of the area corresponding to Fig. 4.4(a) for the Domain I and Domain II, respectively. It evidently shows that the dark and bright regions in the γ-Al_2O_3 layer appeared reversely with respect to each other, indicating that the γ-Al_2O_3 consisted of the two different domains.

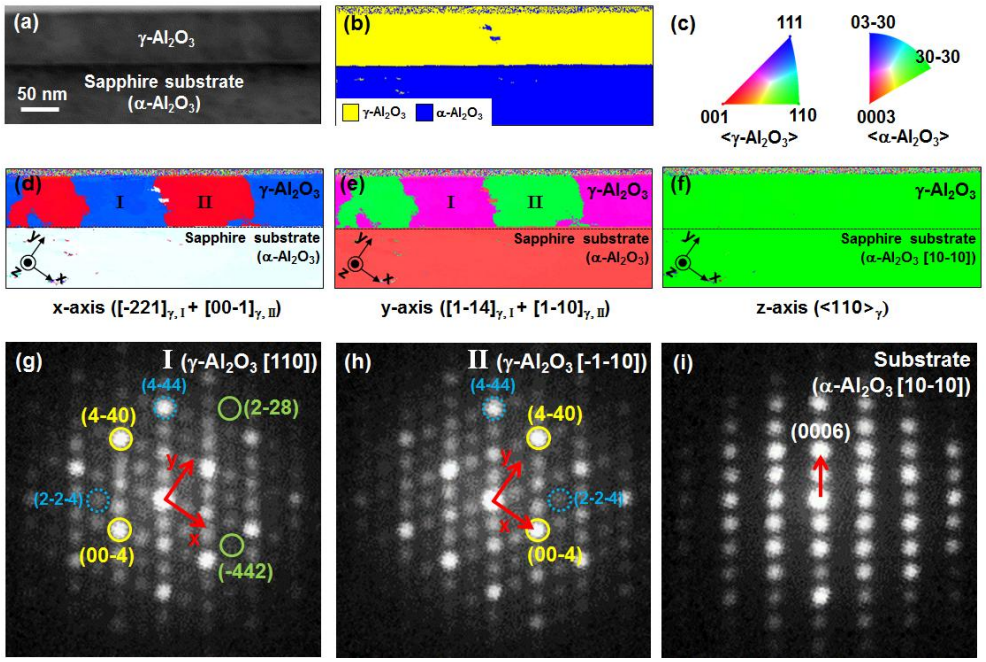

Figure 4.1 TEM orientation imaging results for γ-Al_2O_3 grown on a sapphire substrate, obtained by ASTAR device (NanoMEGAS). (a) Cross-section virtual bright-field image produced from scanning nanobeam precession electron diffraction (NPED) patterns. (b) A phase map of the region corresponding to (a). (c) Color codes for the standard stereographic triangle notation of the γ- and α-Al_2O_3. (d–f) Color-coded crystallographic orientation maps of the region (a), indicating the orientation of lattice planes normal to the (d) *x*-, (e) *y*-, and (f) *z*-axes. Directions of the *x*-, *y*-, and *z*-axes are defined in each figure. NPED patterns from the (g) Domain I, (h) Domain II, and (i) sapphire substrate. The Domains I and II are identified in (d) and (e).

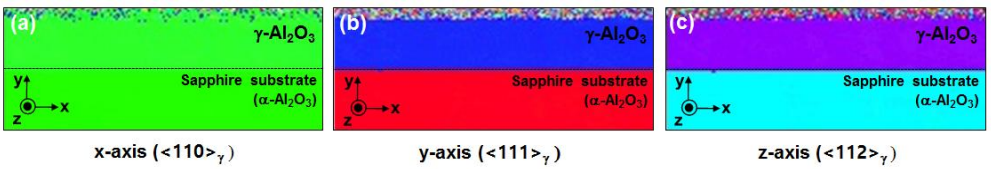

Figure 4.2 TEM orientation imaging results for γ-Al_2O_3 grown on a sapphire substrate viewed at the <1-210>$_\alpha$ projection of sapphire substrate. (a–c) Color-coded crystallographic orientation maps indicating the orientation of lattice planes normal to the (d) *x*-, (e) *y*-, and (f) *z*-axes. Directions of the *x*-, *y*-, and *z*-axes are defined in each figure. Color codes for the standard stereographic triangle notation of the γ- and α-Al_2O_3 is the same as that of Fig. 4.1(c).

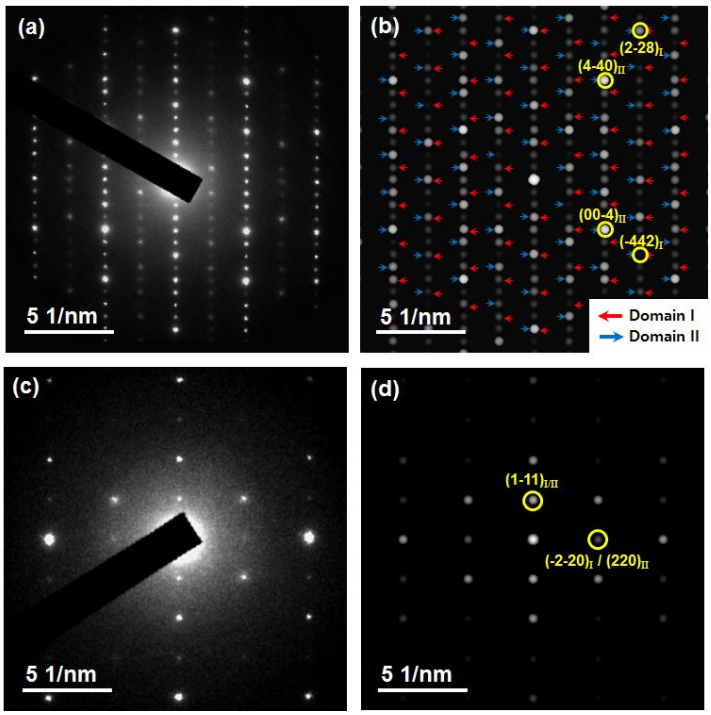

Figure 4.3 Selected area electron diffraction (SAED) patterns of γ-Al_2O_3 layer obtained from different projecting directions, i.e. (a) $<110>_\gamma$ and (c) $<112>_\gamma$, respectively. (b, d) Simulated SAED patterns corresponding to the experimental patterns shown in (a) and (c), respectively. (b) Diffraction spots from Domains I and II in Fig. 1 (c) and (d) are indicated with arrows. The other diffraction spots came from double diffractions between Domains I and II. JEMS code was used for the simulation.

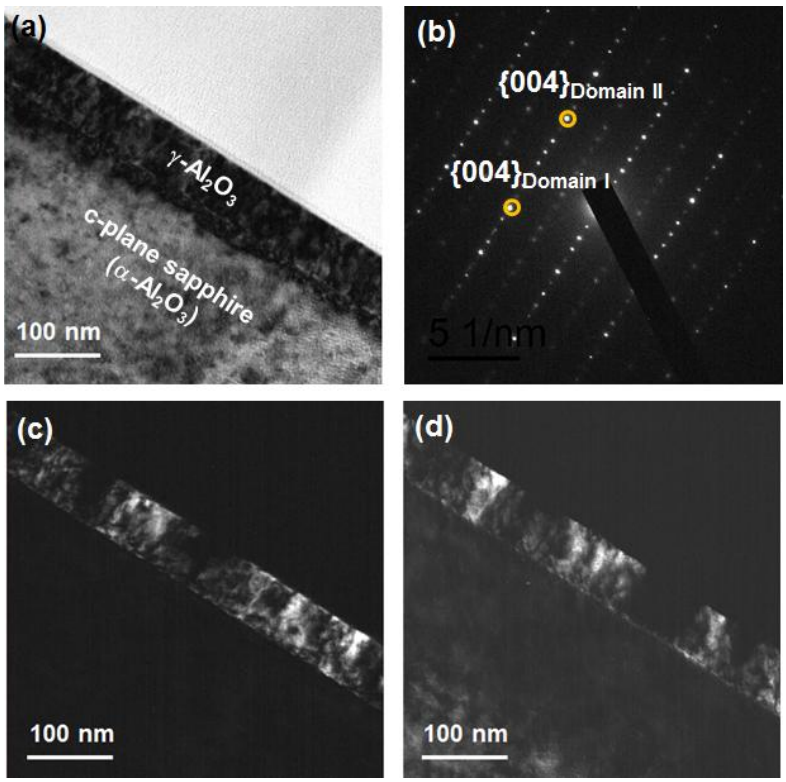

Figure 4.4 (a) Bright-field TEM image of SPE g-Al2O3 layer on a c-plane sapphire substrate. (b) SADP obtained at the SPE g-Al2O3 layer. DF images corresponding to the $\{004\}_{\gamma}$ diffractions from the (c) Domain I and (d) Domain II.

4.4 Discussion on SPE mechanism of γ-Al_2O_3 domain structure

Figure 4.5(a-e) show atomic projections of the γ-Al_2O_3 corresponding to the Domain I and II viewed at the projecting directions for the orientation mappings. The atomic structural model of the γ-Al_2O_3 was made based on crystal structure database (ICSD-66559). As discussed in **Chapter 1.6.1**, atomic structure of the γ-Al_2O_3 is called a defective cubic spinel structure; oxygen ions are face-centered cubic (FCC) structure as an ABCABC··· stacking sequences along {222} planes while aluminum ions partially occupy tetrahedral or octahedral positions in the oxygen framework of the cubic spinel structure satisfying the stoichiometry.[18] Fig. 4.5(a) and (b) show atomic projections of the γ-Al_2O_3 corresponding to the Domain I and II, respectively, viewed at the $<110>_\gamma$ projections, same with Fig. 4.1; $[110]_\gamma$ for Domain I and $[-1-10]_\gamma$ for Domain II. It is found that atomic projections of the domains are in a twin relationship, which makes corresponding atomic planes of the each domain have mirror symmetry such as (2-2-2) planes presented in the figures. This atomic configuration relationship between the domains resulted in their twin-related NPED patterns shown in Fig. 4.1(g) and (h). Figure 4.4(c) shows magnified images of the marked regions with dashed rectangles in Fig. 4.4(a) and (b), which present the stacking sequences of the oxygen ions in (2-22) planes for the Domain I and II, respectively. The positions of close-packed atomic positions of oxygens in FCC structure are indicated by A, B, and C, respectively, showing ABCABC··· stacking

sequences for the Domain I and ACBACB··· stacking sequences for the Domain II. This indicates that the two γ-Al_2O_3 domains were grown on the α-Al_2O_3 with difference stacking sequences. Fig. 4.4(d) and (e), respectively, show the atomic projections of the Domain I and II, viewed at the $<112>_\gamma$ projections, which correspond to the viewing direction of Fig. 4.2; $[-112]_\gamma$ for Domain I and $[1\text{-}1\text{-}2]_\gamma$ for Domain II as shown in the direction notation in Fig. 4.4(a) and (b). In the $<112>_\gamma$ atomic projections, there is no difference recognized on the stacking sequence of aluminum and oxygen ions. Therefore, the two domains cannot be distinguished by the electron diffraction patterns along the $<112>_\gamma$ projection as shown in the Fig. 4.2.

Fig. 4(f) shows atomic projections of the α-Al_2O_3 viewed at the $[10\text{-}10]_\alpha$, which parallels to the $<110>_\gamma$ projecting direction of the epitaxially grown γ-Al_2O_3. In contrast to the γ-Al_2O_3, oxygen ions have ABABAB··· stacking sequences of hexagonal close-packed structure along {0006} planes while every aluminum ion occupies the octahedral positions regularly in the α-Al_2O_3 phase as discussed in **Chapter 1.6.1**.[19] The A and B positions, the atomic positions of oxygen ions labeled on the basis of their stacking sequence along {0006} planes in the α-Al_2O_3 phase, correspond to the A and B positions in the ABCABC··· stacking sequence of oxygen ions along {222} planes in the γ-Al_2O_3 phase, except for slight mismatch of atomic spacing. This similarity of oxygen-ion stacking between α- and γ-Al_2O_3 phases might

be a significant factor for the epitaxial growth of γ-Al_2O_3 {111} on the α-Al_2O_3 {0001} substrate.

The orientation maps of SPE γ-Al_2O_3 shown in Fig. 4.1(d) and (e), which clearly show the distribution of the domains in images, give important information for understanding the formation mechanism of the two kinds of γ-Al_2O_3 domains with different stacking sequences. The each domain structure was found to extend from the interface with sapphire substrate to the surface of SPE γ-Al_2O_3 layer, which is evidence for the successive layer by layer conversion of the amorphous Al_2O_3 layer from the interface with sapphire substrate. Also, it should be noted that all of the domains are originated from the surface of sapphire substrate, i.e., there is no additionally produced domains in the middle of the annealed Al_2O_3 layer. This indicates that both the two different stacking sequences of γ-Al_2O_3 can be possible on the surface of sapphire substrate and their initial stacking sequences are maintained during the vertical growth. Accordingly, surface structure of the {0001} α-Al_2O_3 and favorable stacking positions of γ-Al_2O_3 on the {0001} α-Al_2O_3 surface should be considered to understand the formation of domain structures. Another notable point is that the domain boundary is not straight line along the vertical growth direction, which shows lateral movement of the boundary during the growth. This implies that vertical growth rate of the SPE via layer by layer growth was not the same for all of the interface region. It is speculated that atomistic growth procedure of the one monolayer includes nucleation of crystalline island and its lateral growth in the growing

interface.[20] The rate of nucleation and lateral growth of a nuclei on the interface may differ with location. Thus, the vertical growth rate would be varied with the domains and the SPE process presumably proceeded by competitive growth of the each domain including some lateral growth near the boundary region.

The formation of stacking mismatched γ-Al_2O_3 domains during the SPE were previously introduced by P. S. Sklad et al., based on the observation of two different nano-beam electron diffraction (NBD) patterns from γ-Al_2O_3 layers formed by annealing of ion-implanted amorphous Al_2O_3 on a c-plane sapphire substrate without showing the distribution of two domains in images.[9] They attributed the formation of the stacking mismatched domains to two equally favorable sites for oxygen atoms on the α-Al_2O_3, i.e. B and C on A positions of {111} planes in FCC materials. In that approach, a lot of twin boundaries should be created along the stacking layers, i.e. parallel to *c* planes of the sapphire substrate, because ABCABC stacking sequence can be altered to ACBACB from any layer if the two available positions on the preceding layer have equal energy. However, in practical, the twin boundaries parallel to the stacking layers are hardly observed, as shown in the orientation maps of Fig. 4.1(d) and (e). Rather, the domains maintain their stacking sequence during the vertical growth of γ-Al_2O_3 layers as previously mentioned. This indicates that conversion of stacking sequences from ABCABC to ACBACB was not energetically favorable process. It may imply that during the growth of γ-Al_2O_3 oxygen stacking positions are influenced

by the lower two layers, not only by the proximate underlying layer, e.g. oxygen atoms stacking in C sites (not in A sites) on the preceding two oxygen layers occupying AB sites. In addition, as indicated by colored rectangles in Fig. 4.4(a) and (f), two adjacent oxygen layers of γ-Al_2O_3 in which the interstitial aluminum ions are positioned only at the octahedral sites shows very similar atomic structure with α-Al_2O_3. Thus, the growth of γ-Al_2O_3 on a sapphire substrate would be energetically similar with the growth procedure on the γ-Al_2O_3 surface with two underlying oxygen layers occupying A and B positions, which have the aluminum ions positioned in the octahedral sites. Therefore, when the γ-Al_2O_3 starts to grow on the α-Al_2O_3 substrate, oxygen ions will be firstly located in the C position on the underlying AB layers of α-Al_2O_3.

If position of the first oxygen layer in γ-Al_2O_3 is fixed to C on the {0001} α-Al_2O_3 substrate, the stacking sequence of the γ-Al_2O_3 will be dependent on the stacking order in the first two underlying oxygen layers of α-Al_2O_3, i.e., two possible α-Al_2O_3 surfaces terminated with AB and BA results in the formation of γ-Al_2O_3 domains with different stacking sequences of ABCABC and BACBAC, respectively, as illustrated in Fig. 4.5. For the c-plane α-Al_2O_3, any two surfaces separated by c/6 (where c is the unit-cell height of α-Al_2O_3) have same total energy since they are symmetrically equivalent to one another.[21] Thus, as shown in Fig. 5, two non-identical surfaces terminated

with AB and BA could be on the stepped terraces with step height of c/6, which correspond to the inter-planar spacing between the {0006} planes. During the growth of γ-Al_2O_3 on the stepped c-plane α-Al_2O_3, the first oxygen layers are positioned in C on the both AB- and BA-terminating α-Al_2O_3 surfaces (terraces on the left and right side, respectively, in Fig. 5) and the subsequent oxygen layers are positioned in A and B on the respective ABC- and BAC-terminating preceding layers. In this order, the successive layer-by-layer growth procedure results in the formation of two kinds of γ-Al_2O_3 domains with difference stacking sequences of ABCABC and ACBACB. Accordingly, existence of the two non-identical terminating layers of α-Al_2O_3 could be the reason for the formation of γ-Al_2O_3 domains rather than two available positions for oxygen ions on the α-Al_2O_3 surface.

The domain boundary of γ-Al_2O_3, which has higher energy than inside of a domain, would be favorable sites for the formation of defects during the atomic rearrangement for the subsequent SPE process into α-Al_2O_3. Therefore, in order to obtain high quality SPE (0001) α-Al_2O_3, the area of domain boundaries in the intermediate γ-phase should be reduced. As described above, it is believed that surface structure of the sapphire substrate should be carefully prepared to reduce the domain boundaries. It was reported that high temperature annealing of the intentionally inclined (0001) sapphire substrate results in the formation of stepped terraces with multiple of unit cell height (even multiple of single step (c/6))[22], which provide

surfaces with identical terminating sequences of the oxygen layer. This implies that the domain structure of γ-Al_2O_3 could be controlled by surface treatment of the sapphire substrate and the optimized pre-process of the substrate can reduce domain boundary area of the SPE γ-Al_2O_3 layer on (0001) sapphire substrate.

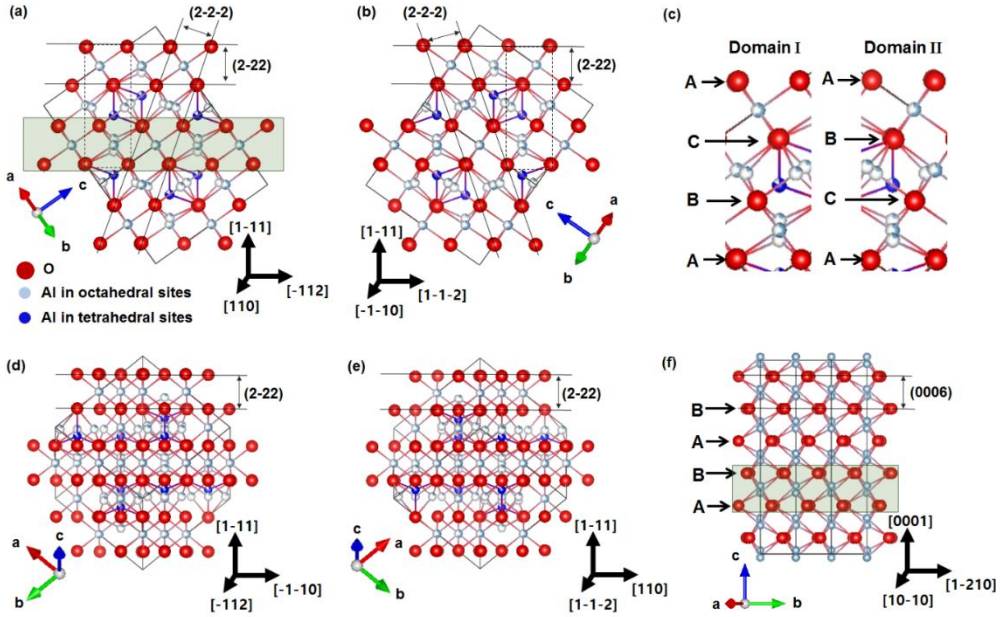

Figure 4.5 (a, b) Atomic projections of the γ-Al_2O_3 corresponding to the Domain (a) I and (b) II viewed at the [110] projection. (c) Atomic projection showing the stacking sequences of oxygen atoms in the Domain I and II. (d, e) Atomic projections of the γ-Al_2O_3 corresponding to Domain (d) I and (e) II viewed at [1-12] and [-112] projections, respectively. These directions correspond to projection directions for the Fig. 2. A fraction of darker color in aluminum ion positions indicates occupancy of the position.

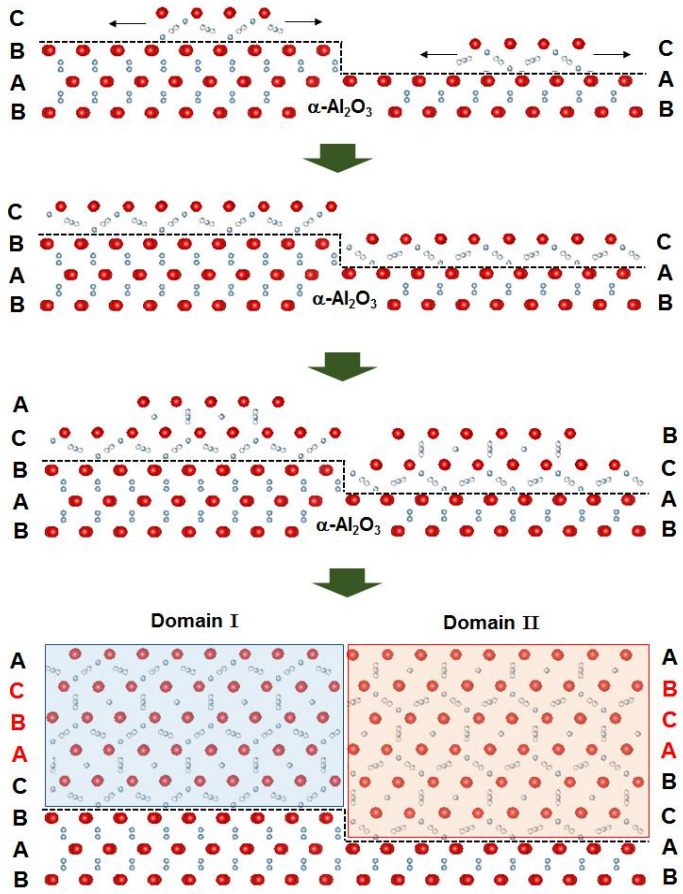

Figure 4.6 Schematic diagram for the SPE procedure of γ-Al_2O_3 on a stepped c-plane sapphire substrate with height of c/6. A, B, and C indicate the stacking positions of the oxygen atoms.

4.5 Summary

We investigated the SPE γ-Al_2O_3 layer on a c-plane sapphire substrate by TEM and computational calculations in order to understand the SPE mechanism of the amorphous Al_2O_3 into the metastable γ-phase. The phase/orientation mapping by an advanced scanning NBD technique of TEM evidently revealed presence of the two stacking-mismatched γ-Al_2O_3 domains in image. Also, we found that the stacking-mismatched γ-Al_2O_3 domains can be distinguishable only at the specific projecting direction; it provides cautions for the analysis of the γ-Al_2O_3 layer, stacking-mismatched domains in particular. More importantly, the distribution the stacking-mismatched domains in the SPE γ-Al_2O_3 layer gives significant information for understanding the formation mechanism of the γ-Al_2O_3 domains. It was found that the growth of SPE γ-Al_2O_3 layers are strongly influenced by at least two stacking steps of oxygen-ion layers of the sapphire substrate near the interface. Accordingly, we suggested that presence of two non-identical surfaces terminated with AB and BA on the stepped {0001} α-Al_2O_3 surface results in the formation of γ-Al_2O_3 domains. The investigation on the SPE mechanism into intermediate γ-Al_2O_3 may provide insights into the improvement direction for achieving greater properties of the subsequent SPE α-Al_2O_3 layer.

4.6 Bibliography

1. G. L. Olson and J. A. Roth, Kinetics of solid phase crystallization in amorphous silicon, Materials Science Reports 3, 1-78 (1988)

2. Hiroshi Ishiwara, Hiroshi Yamamoto, Seijiro Furukawa, Masao Tamura, and Takashi Tokuyama, Lateral solid phase epitaxy of amorphous Si films on Si substrates with SiO2 patterns, Applied Physics Letters 43, 1028 (1983)

3. K. Kusukawa, M. Moniwa, M. Ohkura, and E. Takeda, Enhancement of lateral solid phase epitaxy over SiO2 using a densified and thinned amorphous Si layer, Applied Physics Letters 56, 560 (1990)

4. B. C. Johnson, and J. C. McCallum, Kinetics of arsenic-enhanced solid phase epitaxy in silicon, Journal of Applied Physics 95, 4427 (2004)

5. Jeonghwan Jang, Daeyoung Moon, Hyo-Jeong Lee, Donghyun Lee, Daehan Choi, Dukkyu Bae, Hwankuk Yuh, Youngboo Moon, Yongjo Park, Euijoon Yoon, Incorporation of air-cavity into sapphire substrate and its effect on GaN growth and optical properties, Journal of Crystal Growth **430**, 41–45 (2015)

6. Yoon-Jong Moon, Daeyoung Moon, Jeonghwan Jang, Jin-Young Na, Jung-Hwan Song, Min-Kyo Seo, Sunghee Kim, Dukkyu Bae, Eun Hyun Park, Yongjo Park, Sun-Kyung Kim, and Euijoon Yoon, Microstructured Air Cavities as High-Index Contrast Substrates with Strong Diffraction for Light-Emitting Diodes, Nano Letters (2016)

7. Sung-gyu Kang, Daeyoung Moon, Jeonghwan Jang, Ju-Young Kim, Jin-Yu Suh, Euijoon Yoon, and In-suk Choi, Heung Nam Han, Ultra-Strong Hollow Alumina Nanostructures for High-Efficiency GaN LEDs, submitted

8. C. W. White, L. A. Boatner, P. S. Sklad, C. J. McHargue, and M. J. Aziz, Ion implantation of crystalline oxides and ceramics, Nuclear Instruments and Methods in Physics Research B **32**, 11-22 (1988)

9. P. S. Sklad, J.C. McCallum, C.J. McHargue, and C.W. White, The amorphous-to-gamma transformation in ion implanted Al_2O_3, Nuclear Instruments and Methods in Physics Research B **46**, 102-106 (1990)

10. J. C. McCallum, T.W. Simpson, and I.V. Mitchell, Time resolved reflectivity measurements of the amorphous-to-gamma and gamma-to-alpha phase transitions in ion-implanted Al_2O_3, Nuclear Instruments and Methods in Physics Research B **91**, 60-62 (1994)

11. D. R. Clarke, Epitaxial phase transformations in aluminium oxide, phys. stat. sol. (a) **166**, 183 (1998)

12. Ning Yu, Todd W. Simpson, Paul C. Mclntyre, Michael Nastasi, and Ian V. Mitchell, Doping effects on the kinetics of solid-phase epitaxial growth of amorphous alumina thin films on sapphire, Appl. Phys. Lett. **67** (7) (1995)

13. T. W. Simpson, Qingzhe Wen, Ning Yu, and David R. Clarke, Kinetics of the amorphous $\rightarrow \gamma \rightarrow \alpha$ transformation in aluminium oxide: Effect of crystallographic orientation, Journal of American ceramics society, **81** [1] 61-66 (1998)

14. H. A. Wriedt. The Al-O (Aluminum-Oxygen) System, Bulletin of Alloy Phase Diagrams **6**, 548-552 (1985)

15. M. H. Jacobs and M. J. Stowell, Moiré patterns and coherent double-

positioning boundaries in {111} epitaxial gold films, The Philosophical Magazine: A Journal of Theoretical Experimental and Applied Physics 11, 591-603 (1965)

16. X. W. Zhou and H. N. G. Wadley, Twin formation during the atomic deposition of copper, Acta mater. 47, 1063-1078 (1999)

17. H. S. Kong, B. L. Jiang, J. T. Glass, G. A. Rozgonyi, and K. L. More, An examination of double positioning boundaries and interface misfit in beta-SiC films on alpha-SiC substrates, J. Appl. Phys. 63, 2645-2650 (1988)

18. R.-S. Zhou and R. L. Snyder, Structures and transformation mechanisms of the η, γ, and θ transition aluminas, Acta Cryst. B47, 617-630 (1991)

19. W. E. Lee and K. P. D. Lagerof, Structural and electron diffraction data for sapphire (α-Al_2O_3), Journal of electron microscopy technique 2, 247-258 (1985)

20. N.G. Rudawski, K.S. Jones, and R. Gwilliam, Stressed solid-phase epitaxial growth of ion-implanted amorphous silicon, Materials Science and Engineering R 61, 40–58 (2008)

21. J. Guo, D. E. Ellis, and D. J. Lam, Electronic structure and energetics of sapphire (0001) and (1-102) surfaces, Physical review B 45, 13647-13656 (1992)

22. Y. Shiratsuchi, M. Yamamoto, and Y. Kamada, Surface structure of self-organized sapphire (0001) substrate with various inclined angles, Jpn. J. Appl. Phys. 41, 5719-5725 (2002)

Chapter 5. Characteristics of GaN layer and performances of GaN-based LEDs on CES

5.1 Introduction

In order to enhance the external quantum efficiency (EQE) of GaN-based LEDs, various technical approaches have been reported: epitaxial lateral overgrowth[1-2], patterned sapphire substrate (PSS)[3-5], photonic crystal[6-7], surface texturing[8-9], and embedded nano particles into GaN layers.[10-11] In addition, for reduction of the stress in GaN film and the wafer bow, several techniques such as embedded void structures[12-13], superlattice interlayers[14], and nano-columnar structures[15] have been suggested.

Well-defined void structures inside the GaN layer have been investigated both to improve EQE and to reduce the wafer bow. Kim *et al*. used silica hollow nanospheres to grow a void-embedded GaN layer.[16] The incorporation of uniform-size silica hollow nanospheres at the interface between the GaN layer and the sapphire substrate was revealed to effectively enhance EQE and to reduce the wafer bow. Kim *et al.* reported the formation of an array of air voids in GaN by the wet chemical etching of GaN through pre-formed SiO_2 patterns on a sapphire substrate.[17] Park *et al*. formed voids between PSS and a GaN layer by H_3PO_4-based hot chemical etching of partially-coalesced GaN templates and subsequent GaN regrowth.[18] Sheu *et al*. used an Ar-implanted sapphire substrate and found a void formation at sapphire/GaN interface.[19] However, extra processing steps were needed to form the voids

mostly in the course of GaN growth[17-18]; it was reported that these extra steps often caused the degradation of device performance such as high reverse leakage current[18-19]. In addition, such methods seem to have limitations in varying shape, size, and distribution of voids to optimize the EQE.

For the growth scheme using a cavity engineered sapphire substrate (CES), a two-dimensionally patterned cavity array can be incorporated into the interface between the GaN and sapphire substrate without the additional regrowth step. Also, as mentioned in **Chapter 2**, this scheme enables us to control the shape, size, and distribution of the cavity pattern more easily. Therefore, the CES scheme is easier to optimize the cavity structures for the improvement of LED efficiency and the reduction of the wafer bow than other conventional methods.

In this chapter, the growth and characteristics of GaN epitaxial layer on the CES were investigated. A completely coalesced pit-free smooth surface of GaN layer was obtained on the CES. The threading dislocation density of the GaN layer on the CES was reduced by the lateral overgrowth process compared to that on the planar sapphire substrate. In addition, we demonstrated that the incorporation of cavities can reduce the stress in GaN film and the wafer bow. Finally, LED chips were fabricated on the CES. The output power of a LED on CES at an injection current of 20 mA was measured to be 2.2 times higher than that on a planar sapphire substrate. The detailed investigation on GaN growth and LED performances on the CES will be discussed.

5.2 Experimental details

GaN layers were grown on 2 inch CES using a Thomas Swan 3x2'' metalorganic chemical vapor deposition system. Figure 5.1 shows schematic diagram for the growth condition of the GaN layer. Trimethylgallium and ammonia were used as precursors for Ga and N, respectively. H_2 was used as a carrier gas. The thermal cleaning was performed for 5 min at 1100 ^oC, and the temperature was then decreased to 560 ^oC at which a low temperature GaN buffer layer was grown at 13.3 kPa for 220 s. The high temperature GaN epitaxial layers were grown at 1040 ^oC and 40.0 kPa. An LED structure was grown not only on CES but also on the planar sapphire substrate in the same batch for comparison. For the LED structure, a 3 μm thick un-doped GaN layer was deposited on the substrates, followed by 2.5 μm thick n-type GaN, 5 periods of InGaN (3 nm)/GaN (7 nm) multiple quantum well (MQW) and p-type GaN (150 nm). Trimethylindium was used as a precursor for In. Silane and bis-cyclopentadienyl magnesium were used as the dopants for the n- and p-type layers, respectively. For the fabrication of LED chips, after the mesa etching of 1000 x 1000 μm^2, Au (500 nm)/Ni (25 nm)/Cr (20 nm) and ITO (200 nm) were deposited as an electrode and a transparent conductive layer, respectively. The surface morphology and the cross-section view of the samples were observed by a Hitachi S-4800 field emission scanning electron microscope (FESEM) operated at 15 kV. Cathodoluminescence (CL) was measured using a Gatan MonoCL4 operated at 5 kV. X-ray diffraction rocking curves and high resolution X-ray diffractions were measured by a

PANalytical X'pert Pro XRD operated at 30 kV. Raman measurement was performed using a Horiba Jobin Yvon LabRam Aramis to investigate the stress relaxation of the GaN layers grown on CES. A He-Ne laser with a wavelength of 633 nm was used at a laser power of 1 mW and beam size of the laser was ~ 1 μm. For Raman mappings, resolutions of the spacing and frequency were 0.2 μm and 0.3 cm^{-1}, respectively. Light output powers at various forward voltages were measured on-wafer using EtaMax LIF-AT and Ocean Optics FOIS-1 integrating sphere.

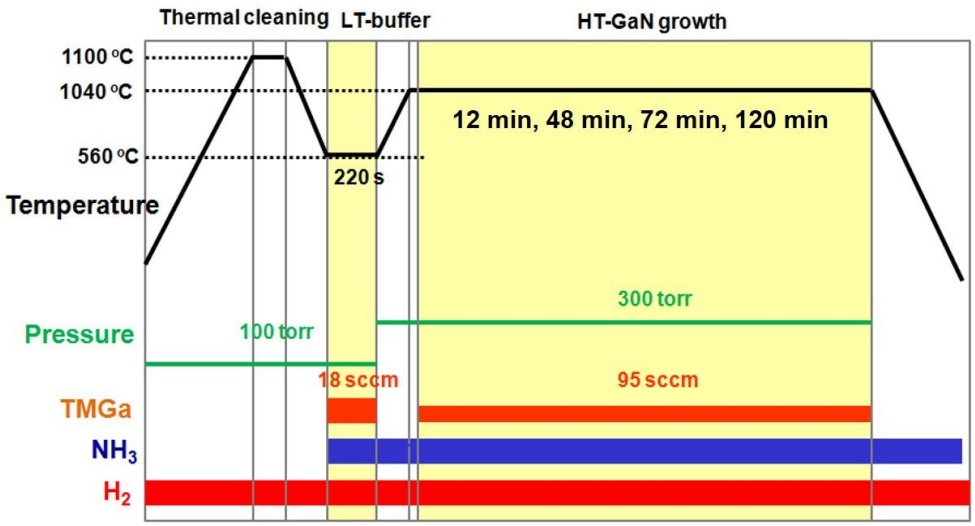

Figure 5.1 Schematic diagram for the growth condition of the GaN layer

5.3. Growth of GaN epitaxial layer on CES

Figure 5.2 (a)–(d) show the morphological evolution of the GaN layer during the growth on CES observed at various growth times. Fig. 5.2 (a) shows that the GaN growth initiated not only on the planar area between the cavities but also on the top planar region of the alumina, which is marked in the inset. It is speculated that the top area of the alumina shell provides a c-plane template for the GaN growth. On the other hand, we found that GaN was not grown on the side wall of the alumina shell. It is worth noting that the c-plane of the film is parallel to that of the sapphire substrate, and the side walls of the shell surface provide high index planes, which may be energetically unfavorable for the GaN growth. The inset in Fig. 5.2 (a), a cross-sectional view along the dotted line, illustrates the GaN layers were grown on both areas. The angle of the side GaN facets developed in the area between the cavities was measured to be 58^{o} with respect to c-plane, corresponding to the {11-22} plane. As the growth time increased, GaN film filled up the space between the cavities, as shown in Fig. 5.2 (b). Then, the GaN layer grew faster in the vertical direction than in the lateral direction until it was surrounded only by {11-22} facets, as shown in the inset of Fig. 5.2 (b). Finally, the GaN {11-22} facet moved laterally, as shown in Fig. 5.2 (c). The inset in Fig. 5.2 (c), a cross-section view of GaN in the region of the cavity, illustrates that the {11-22} facets moved toward the center of the pattern, indicating clearly that the lateral growth was in progress. It was observed that the GaN film grown for 120 min, shown in Fig. 5.2 (d), was completely coalesced and a pit-free smooth surface was obtained after growth of 120 min. It is clear that the well-defined cavity array was maintained at the

interface after the high temperature growth.

In addition to the hemispherical cavity pattern, various cavity structures can be incorporated in GaN layer depending on the cavity design of the CES. Figure 5.3 (a)-(d) show SEM images of the GaN layers grown on the CES with various cavity shapes such as hemisphere, cylinder, stripe, and cone, respectively**.** It is clearly shown that various well-defined cavity structures are incorporated in the interface between the GaN layer and the sapphire substrate.

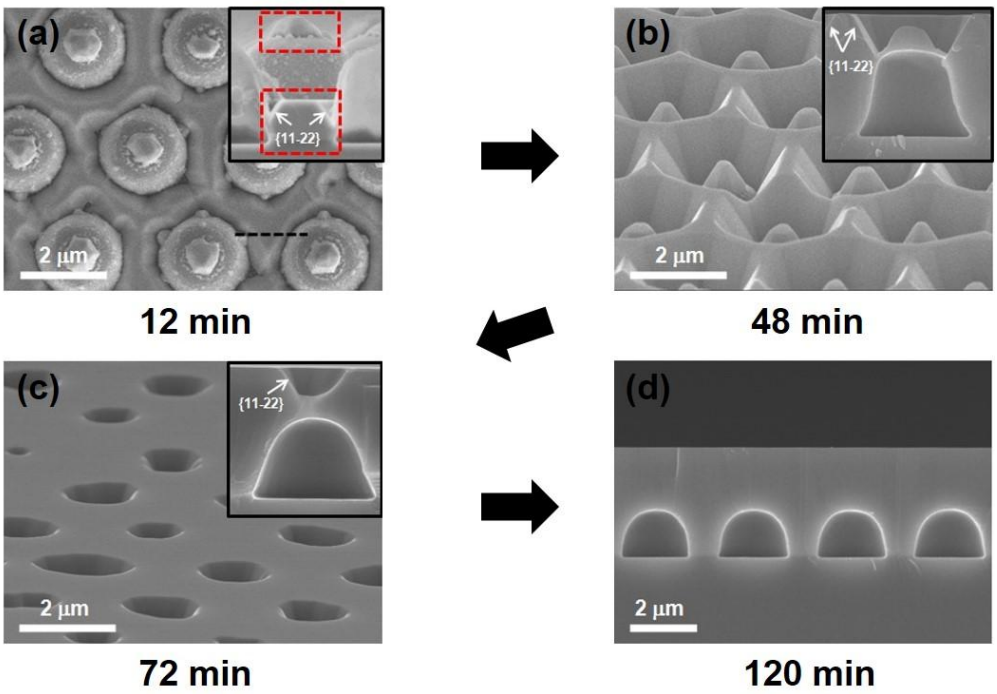

Figure 5.2 SEM images of the morphological evolution of the GaN epitaxial layer grown on CES after (a) 12 min, (b) 48 min, and (c) 72 min at 1040 ^{o}C. The insets in Figs. 3 (a), 3 (b), and 3 (c) show the cross-section images along the dotted line in Fig. 3(a). (d) Cross-section SEM image of the GaN layer grown on the CES for 120 min.

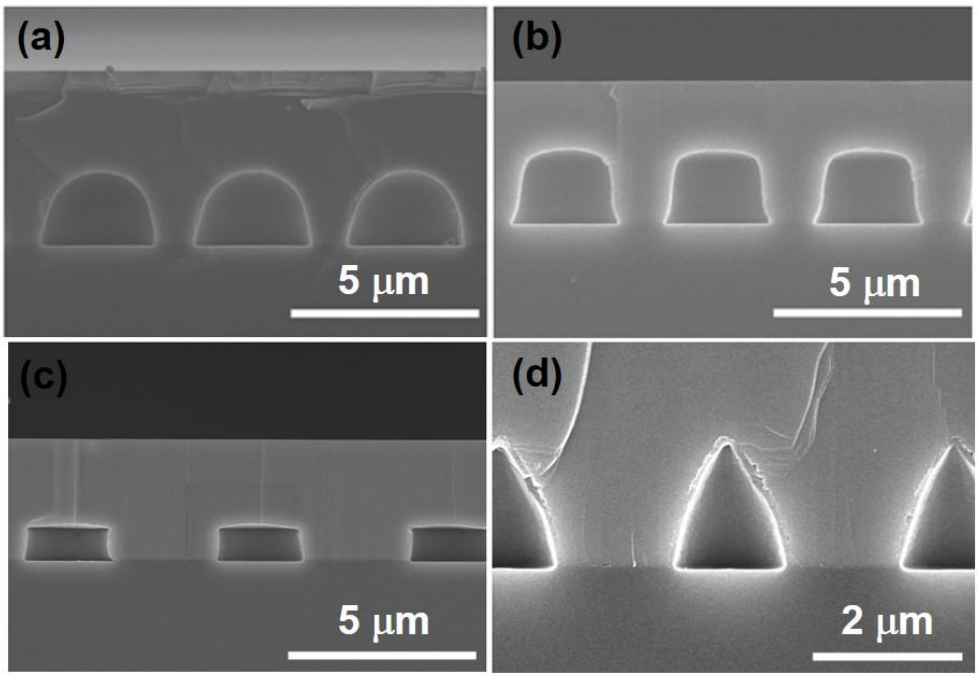

Figure 5.3 Fully coalesced GaN layers grown on the CES with various pattern shapes such as (a) hemisphere, (b) cylinder, (c) stripe, and (d) cone**.**

5.4 Characteristics of GaN epitaxial layer grown on CES

In order to evaluate the crystal quality of the GaN layers, XRD and CL measurements were performed for the GaN layers grown on the CES and planar sapphire substrate. Full widths at half maximum (FWHMs) of XRD rocking curve for (002) and (102) planes of the GaN were 269 arcsec and 289 arcsec, respectively. For reference, FWHMs of the GaN grown on a planar sapphire were 247 arcsec and 352 arcsec for (002) and for (102), respectively. Reduction of FWHM for the (102) plane can be explained by the decrease in edge dislocation density due to the lateral overgrowth of GaN.[20-21] To find out the reduction of threading dislocation density in the GaN layer on the CES, CL measurement was performed on both GaN layers. Fig. 5.4 (a) and (b) show plan-view CL images of the GaN layers on the CES and planar sapphire substrate, respectively. In the CL images, the dark spot densities of the GaN layers grown on CES and planar sapphire substrate were 1.4×10^8 cm^{-2} and 1.9×10^8 cm^{-2}, respectively, demonstrating that the threading dislocation density was reduced by using the CES. The threading dislocation was reduced due to the dislocation bending and annihilation during the lateral overgrowth. Further reduction in threading dislocation density is expected by the optimization of lateral overgrowth on CES.

The high-energy Raman E_2 mode was measured by Raman spectroscopy to evaluate the stress relaxation in the GaN layer on CES as shown in the Fig. 5.5. Among lattice vibration modes in hexagonal GaN, E_2 (high) mode is most sensitive to the in-plane stress of the c-plane GaN. The stress has

influence on the lattice constant of a crystal, resulting in change of vibration energy of a lattice. Under the compressive stress in GaN layer, Raman spectrum of E_2 (high) mode exhibits blue shift. When the compressive stress is relaxed, the phonon frequency is decreased towards the value of stress-free GaN. The in-plane stress in GaN layer can be generally calculated using the following equation[22-23]

$$\sigma(\text{Raman}) = \frac{\Delta\omega}{4.2}\ \text{GPa}, \qquad [3\text{-}1]$$

where $\Delta\omega$ denotes the frequency shift of the GaN high-energy E_2 mode peak relative to the stress-free GaN layer. From Fig. 5.5, the peaks for the GaN layers grown on the CES and planar sapphire substrate were found to be located at 569.7 cm^{-1} and 570.5 cm^{-1}, respectively, which are blue-shifted with respect to the measured value of E_2 mode peak for stress-free GaN substrate, 568.0 cm^{-1}. From the equation [3-1], the stress for the GaN layers grown on CES and planar sapphire substrate were calculated to be 404.8 MPa and 595.2 MPa, respectively, indicating that the incorporation of the cavity structure reduced the stress in the GaN layer by ~30%.

In addition to the stress relaxation in GaN layer on CES, the curvature of the wafers was also evaluated from the separate wafer bow measurement by a laser scanning technique as shown in Fig. 5.6. The curvatures for the GaN layer on CES and the planar sapphire substrate were 97 km^{-1} and 140 km^{-1}, respectively, implying that the stress in GaN was reduced by ~30 %. For this estimation we used Stoney's formula, which tells that the stress in film is proportional to the curvature of a wafer.[24]

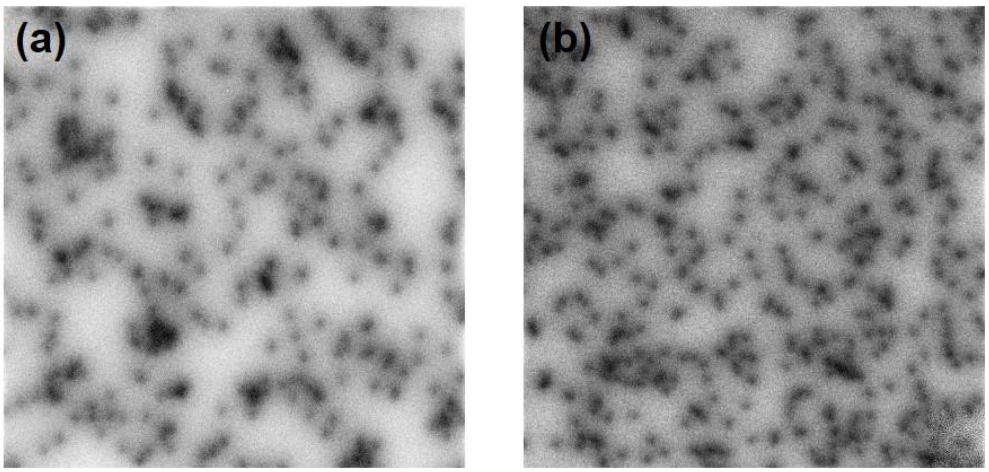

Figure 5.4 Plane-view CL images on the (a) CES and (b) planar sapphire substrate.

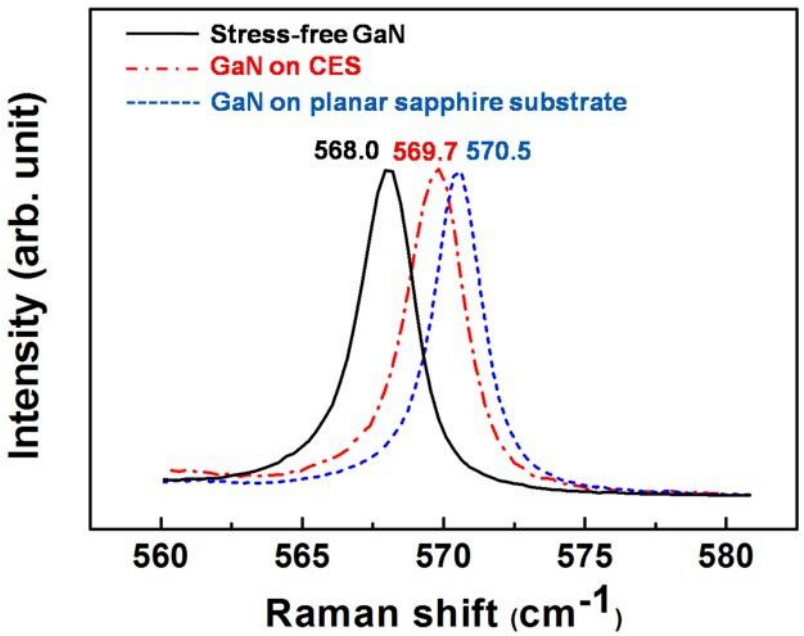

Figure 5.5 Raman spectra of the free-standing GaN substrate, GaN epitaxial layer on the CES and planar sapphire substrate.

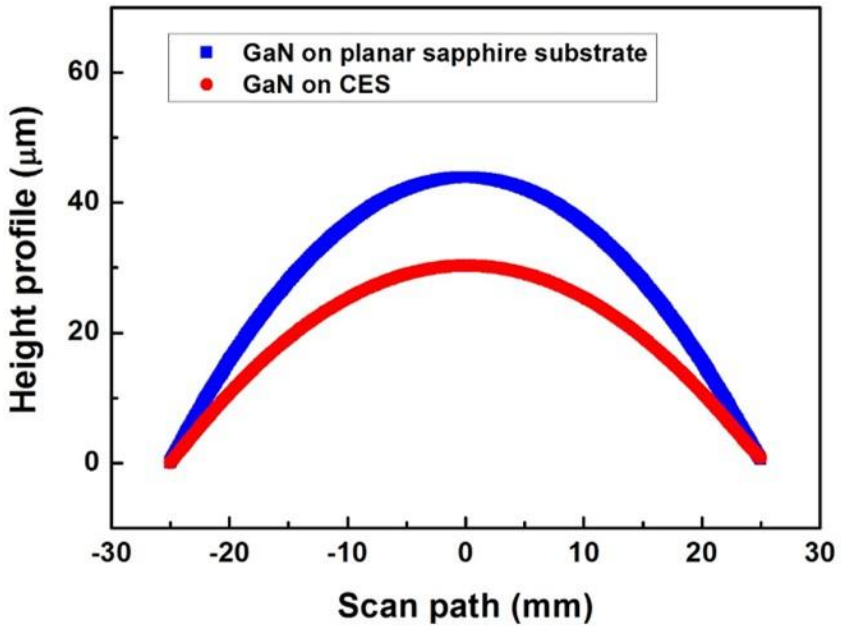

Figure 5.6 Height profile of the GaN wafers on the CES and planar sapphire substrate.

5.5 Fabrication and performances of LEDs on CES

To confirm the effect of incorporation of air cavities on the LED performances, LED chips were fabricated on the CES and planar sapphire substrate. Figure 5.7 shows schematic diagrams of the LED structures. The light output power and forward voltage of the LEDs on CES and planar sapphire substrate were measured on wafer. Figure 5.8 shows the L-I-V curves for the LEDs on CES and planar sapphire substrate. At an injection current of 20 mA, the forward voltage of both samples was measured to be 3.40 V and the output power of LED on CES was found to be 2.2 times higher than that on the planar sapphire substrate. This is due to the improved crystal quality of the GaN layer during the lateral overgrowth and enhanced light extraction efficiency by strong diffraction of the emitted light at the high-index-contrast cavity patterns.[25] Figure 5.9 shows EL spectra of the LEDs on CES and planar sapphire substrate. The EL peak intensity of LED on CES was higher than that on the planar sapphire substrate and the dominant peak wavelength of the LED on CES showed a red shift of 12 nm from 439.0 nm for LED on the planar sapphire substrate to 451.0 nm. The red shift is presumably attributed the higher In incorporation during the growth of InGaN/GaN multi quantum wells (MQWs). To find out the In composition of the MQWs, high resolution omega-two theta XRD was measured for both LED structures as shown in Fig. 5.10. In composition and thickness of well and barrier of InGan/GaN MQW layer were obtained by the measured and fitted scans. The thickness of well and barrier was almost same for both samples. However, In composition of 23.5 % for the LED structure on CES was higher than that of 18.5 % for the reference. This higher In composition

for CES is due to slightly lower surface temperature with less heat conduction from the susceptor. In addition, the degree of wafer bow during MQW growth somewhat differed for CES compared to planar sapphire substrate during the MQW growth, resulting in different surface temperature distributions. The surface of the wafer pockets was typically machined to be non-flat for a certain type of wafer. The CES may not match the wafer pockets, resulting in lower and uneven surface temperatures. Standard deviations of the PL peak wavelength distribution for the LED structure on CES and the planar sapphire substrate were 1.6% and 0.7%, respectively, indicating that the temperature uniformity of CES was inferior to that of the planar sapphire substrate. To improve the surface temperature uniformity of CES, the wafer pockets should be optimized for the wafer bow of CES at growth temperature.

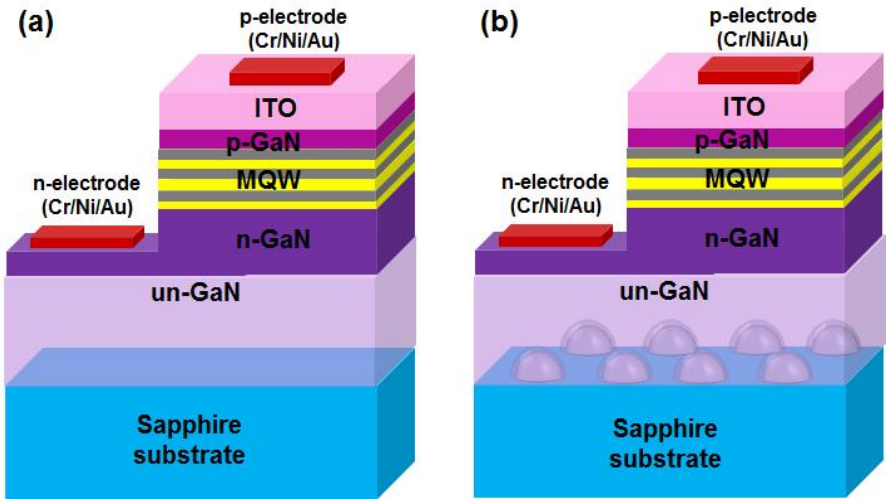

Figure 5.7 Schematic diagram of the LED structure on (a) planar sapphire substrate and (b) CES

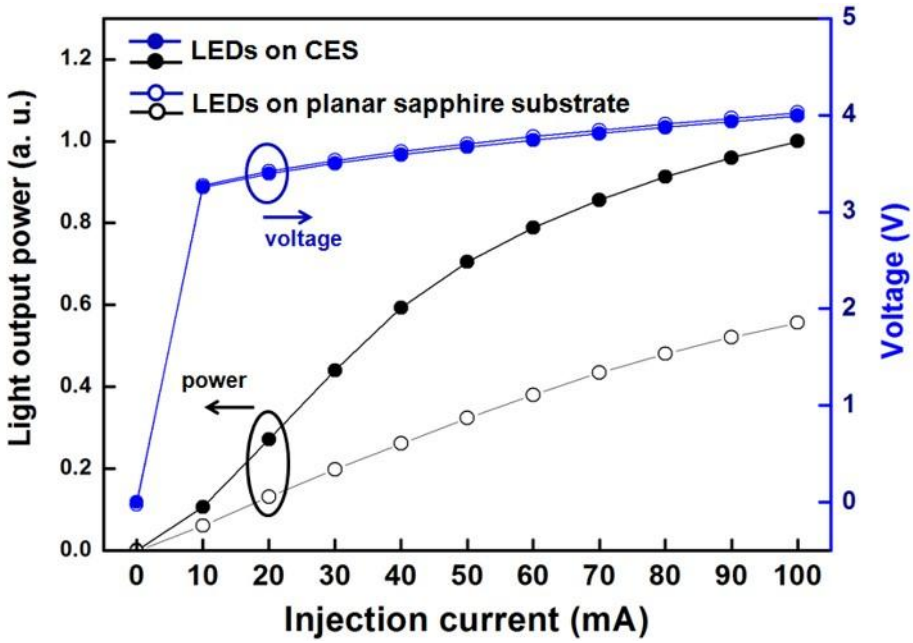

Figure 5.8 Light output power-current-voltage (L-I-V) characteristics of the LEDs on CES and planar sapphire substrate.

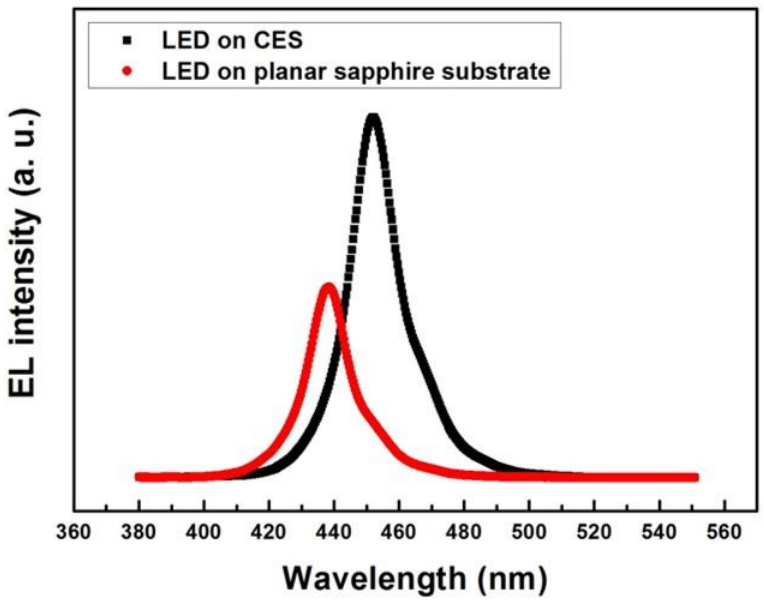

Figure 5.9 EL spectra of the LEDs on CES and planar sapphire substrate.

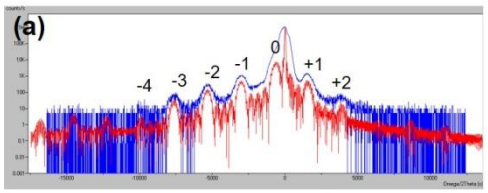

In composition	Well thickness	Barrier thickness
23.5 %	2 nm	5.1 nm

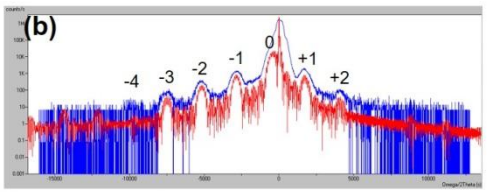

In composition	Well thickness	Barrier thickness
18.5 %	2 nm	5.1 nm

Figure 5.10 Measured and fitted scans of high resolution omega-two theta XRD for the LED structures on (a) CES and (b) planar sapphire substrate.

5.6 Summary

In summary, we investigated growth behavior of GaN on the CES. The GaN film was observed to fill the spaces between the cavities at the initial stage of growth and then grow laterally over the cavities with {11-22} facets, leading to a completely coalesced pit-free smooth surface. Using this new growth scheme, various cavity structure could be incorporated in the GaN epitaxial layers. The HWHMs of XRD rocking curve for (102) planes of the GaN on CES was reduced from 352 acrsec for the GaN on planar sapphire substrate to 289 acrsec by reduction of edge dislocation during the lateral overgrowth. In addition, CL dark spot density was reduced from 1.9×10^8 cm^{-2} to 1.4×10^8 cm^{-2}, demonstrating that the threading dislocation density was reduced using the CES. The incorporation of cavities was observed to significantly reduce the stress in the GaN film by ~30%. The output power of LED on CES at an input current of 20 mA was measured to be 2.2 times higher than that on the planar sapphire substrate. Its dominant peak showed a red shift of 12 nm due to the higher In incorporation during the growth of InGaN/GaN MQWs, presumably associated with the lower surface temperature in the presence of the air-cavity.

5.7 Bibliography

1. T. S. Zheleva, O-H Nam, M. D. Bremser, and R. F. Davis, "Dislocation density reduction via lateral epitaxy in selectively grown GaN structures ," *Appl. Phys. Lett.,* vol. 71, no. 17, pp. 2472-2474, Oct. 1997.

2. P. Gibart, "Metal organic vapor phase epitaxy of GaNandlateral overgrowth," *Rep. Prog. Phys.,* vol. 67, pp. 667-715, Apr. 2004.

3. K. Tadatomo, H. Okagawa, Y. Ohuchi, T. Tsunekawa, T. Jyouichi, Y. Imada, M. Kato, H. Kudo, T. Taguchi, "High Output Power InGaN Ultraviolet Light-Emitting Diodes Fabricated on Patterned Substrates Using Metalorganic Vapor Phase Epitaxy," *phys. stat. sol. (a)*, vol. 188, no. 1, pp. 121-125, Nov. 2001.

4. M. Yamada, T. Mitani, Y. Narukawa, S. Shioji, I. Niki, S. Sonobe, K. Degichi, M. Sano and T. Mukai, "InGaN-Based Near-Ultraviolet and Blue-Light-Emitting Diodes with High External Quantum Efficiency Using a Patterned Sapphire Substrate and a Mesh Electrode," *Jpn. J. Appl. Phys.*, vol. 41, no. 12B, pp. 1431-1433 Dec. 2002.

5. S.J. Chang, Y.C. Lin, Y.K. Su, C.S. Chang, T.C. Wen, S.C. Shei,J.C. Ke, C.W. Kuo, S.C. Chen, C.H. Liu, "Nitride-based LEDs fabricated on patterned sapphire substrates," *Solid-State Electronics*, vol. 47, no. 9, pp. 1539-1542, Sep. 2003.

6. T. N. Oder, K. H. Kim, J. Y. Lin, and H. X. Jiang, "III-nitride blue and ultraviolet photonic crystal light emitting diodes," *Appl. Phys. Lett.*, vol. 84, no. 4, pp. 466-468 Jan. 2004.

7. E. Matioli, E. Rangel, M. Iza, B. Fleury, N. Pfaff, J. Speck, E. Hu and C. Weisbuch, “High extraction efficiency light-emitting diodes based on embedded air-gap photonic-crystals,” Appl. Phys. Lett., vol. 96, no. 3, pp. 031108, Jan. 2010.

8. C. Huh, K-S Lee, E-J Kang and S-J Park, “Improved light-output and electrical performance of InGaN-based light emitting diode by micro roughening of the p-GaN surface,” *J. Appl. Phys.*, vol. 93, no. 11, pp. 9383-9385, Jun. 2003.

9. H-M An, J. I. Sim, K. S. Shin, Y. M. Sung and T. G. Kim, “Increased Light Extraction From Vertical GaN Light-Emitting Diodes With Ordered Cone-Shaped Deep-Pillar Nanostructures,” *IEEE J. Quantum Electron.*, vol. 48, no. 7, pp. 891-896, Jul. 2012.

10. K. Ueda, Y. Tsuchida, N. Hagura, F. Iskandar, K. Okuyama and Y. Endo, “High performance of GaN thin films grown on sapphire substrates coated with a silica-submicron-sphere monolayer film,” Appl. Phys. Lett., vol. 92, no. 10, pp. 101101, Mar. 2008.

11. S. H. Park, J. Park, D.-J. You, K. Joo, D. Moon, J. Jang, D.-U.Kim, H. Chang, S. Moon, Y.-K.Song, G.-D. Lee, H. Jeon, J. Xu, Y. Nanishi and E. Yoon, “Improved emission efficiency of a-plane GaN light emitting diodes with silica nano-spheres integrated into a-plane GaN buffer layer,” *Appl. Phys. Lett.*, vol. 100, no. 19, pp. 191116, May 2012.

12. C.-H. Chiu, C.-C. Lin, H.-V. Han, C.-Y. Liu, Y.-H. Chen, Y.-P. Lan, P. Yu, H.-C. Kuo, T.-C. Lu, S.-C. Wangand C.-Y. Chang, “High efficiency GaN-based light-emitting diodes with embedded air voids/SiO2 nanomasks,” *Nanotechnology*, vol. 23, pp. 045303, Jan. 2012.

13. H.-H. Huang, C.-L. Chao, T.-W. Chi, Y.-L. Chang, P.-C. Liu, L.-W. Tu, J.-D. Tsay, H.-C. Kuo, S.-J. Cheng, W.-I Lee, "Strain-reduced GaN thick-film grown by hydride vapor phase epitaxy utilizing dot air-bridged structure," *J. Crystal Growth*, vol. 311, no. 10, pp. 3029-3032, May 2009.

14. M. Sakai, T. Egawa, M. Hao and H. Ishikawa, "Effect of Various Interlayers on Epiwafer Bowing in AlGaN/GaN High-Electron-Mobility Transistor Structures," *Jpn. J. Appl. Phys.*, vol. 43, no.12, pp. 8019-8023, Dec. 2004.

15. I.-S. Shin, D. Lee, K.-H. Lee, H. You, D. Y. Moon, J. Park, Y. Nanishi and E. Yoon, "Growth of GaN layer with preserved nano-columnar low temperature GaN buffer to reduce the wafer bowing," *Thin Solid Films*, vol. 546, pp. 118-123, Nov. 2013.

16. J. Kim, H. Woo, K. Joo, S. Tae, J. Park, D. Moon, S. H. Park, J. Jang, Y. Cho, J. Park, H. Yuh, G.-D. Lee, I.-S. Choi, Y. Nanishi, H. N. Han, K. Char and E. Yoon, "Less strained and more efficient GaN light-emitting diodes with embedded silica hollow nanospheres," *Scientific Reports, vol.* 3, pp. 3201 Nov. 2013.

17. H. G. Kim, H. K. Kim, H. Y. Kim, H. Jeong, S. Chandramohan, P. Uthirakumar, M. S. Jeong, J.-S. Lee, E.-K. Suh and C.-H. Hong, "Enhanced air-cavity effect of periodically oriented embedded air protrusions for high-efficiency InGaN/GaN light-emitting diodes," *Opt. Lett.*, vol. 35, no. 18, pp. 3012-3014, Sep. 2010.

18. E.-H. Park, J. Jang, S. Gupta, I. Ferguson, C.-H. Kim, S.-K. Jeon and J.-S. Park, "Air-voids embedded high efficiency InGaN-light emitting diode," *Appl. Phys. Lett.*, vol. 93, no. 19, pp. 191103, Nov. 2008.

19. J.-K. Sheu, Y.-H. Yeh, S.-J. Tu, M.-L. Lee, P. C. Chen and W.-C. Lai, "Improved Output Power of GaN-based Blue LEDs by Forming Air Voids on Ar-Implanted Sapphire Substrate," *J. Light wave Technol.*, vol. 31, no. 8, pp. 1318-1322, Apr. 2013.

20. B. Heying, X. H. Wu, S. Keller, Y. Li, D. Kapolnek, B. P. Keller, S. P. Den Baars and J. S. Speck, Role of threading dislocation structure on the x-ray diffraction peak widths in epitaxial GaN films, Appl. Phys. Lett. **68**, 643 (1996).

21. D. S. Wuu, W. K. Wang, K. S. Wen, S. C. Huang, S. H. Lin, S. Y. Huang, C. F. Lin R. H. Horng, Defect reduction and efficiency improvement of near-ultraviolet emitters via laterally overgrown GaN on a GaN/patterned sapphire templat, Applied Physics Letters **89**, 161105 (2006).

22. Z. Zheng, Z. Chen, H. Wu, Y. Chen, S. Huang, B. Fan, Y. Xian, Z. Wu, G. Wang, H. Jiang, Effect of periodic Si-delta-doping on the evolution of yellow luminescence and stress in *n*-type GaN epilayers, J. Crystal Growth **387**, 52 (2014).

23. C. Kisielowski, J. Kruger, S. Ruvimov, T. Suski, J. W. Ager III, E. Jones, Z. Liliental-Weber, M. Rubin, and E. R. Weber, M. D. Bremser and R. F. Davis, Strain-related phenomena in GaN thin films, Phys. Rev. B **54**, 17745 (1996)

24. G. Stoney, Proc. R. Soc. Lond. A **82**, 172 (1909)

25. Yoon-Jong Moon, Daeyoung Moon, Jeonghwan Jang, Jin-Young Na, Jung-Hwan Song, Min-Kyo Seo, Sunghee Kim, Dukkyu Bae, Eun Hyun Park, Yongjo Park, Sun-Kyung Kim, and Euijoon Yoon, Microstructured Air Cavities as High-Index Contrast Substrates with Strong Diffraction for Light-

Emitting Diodes, Nano Letters 16, 3301-3308 (2016)

Chapter 6. Growth of GaN epitaxial layer on partially crystallized cavity engineered sapphire substrate for suppression of parasitic GaN growth on pattern surface

6.1 Introduction

With the advantages in improving not only crystal quality of the epitaxial layers but also light extraction of LEDs, the epitaxial lateral overgrowth (ELO) method using patterned sapphire substrate (PSS) has been an typical approach to obtain highly efficient LEDs.[1-2] As mentioned in previous chapters, we have reported a new growth scheme using a cavity engineered sapphire substrate (CES) in which cavity patterns were arrayed on a sapphire substrate, exhibiting improved output power of the LED at 462 nm by ~9 % compared to that on the PSS.[3-4] As shown in Fig. 5.2, during the growth of GaN layer on the CES, undesired GaN crystals were deposited on top of the cavity patterns. The growth of GaN on the top is caused by the fact that the cavity top area was local c-plane of the fully crystallized single crystalline α-Al_2O_3 (sapphire) by solid-phase epitaxy (SPE).

This undesired growth of GaN was also observed for the PSS in which the GaN growth can occur on a side wall of sapphire pattern, leading to undesired generation of threading dislocations in GaN region above the patterns during the coalescence process of GaN layer.[5-8] It is believed that

threading dislocations can be generated when GaN on flat area between patterns merge with the GaN on top of the patterns and can propagate vertically to the merging surface of GaN layer as shown in Fig. 6.1.[5-6] Also, dislocations themselves in GaN grown on the pattern surface, generated due to the lattice mismatch between the GaN and patterned sapphire, can thread up to the merging surface as shown in Fig. 6.2.[7-8] In order to suppress the parasitic growth of GaN, which generates threading dislocations during the merging process, on the side wall of PSS, several techniques such as controlling the growth rate[5], using sputtered AlN nucleation layer[6], shaping of sapphire pattern as pyramid with a sharp tip[8], and performing ion-implantation on the cone-shaped pattern[9] have been reported.

In this research, to suppress the parasitic growth of GaN on the CES, we proposed growth of GaN layer on a partially crystallized CES (PCCES) in which only the planar region between the patterns was crystallized into single crystalline (0001) α-Al_2O_3 while the alumina shell surrounding the cavities consisted of nanocrystalline γ-Al_2O_3 by controlling the crystallization process of the amorphous alumina cavity structure. It is expected that sufficient area of preferential growth planes for GaN, such as (0001) c-, (11-20) a-, and (11-23) n-plane in α-Al_2O_3[10-12], will not appear on the cavity pattern since the nanocrystalline nature of alumina cavity shell has very short-range crystalline coherency without apparent preferred orientations. Instead of the preferred growth of GaN, nanocrystalline GaN islands were formed on the cavity patterns. Kim et al. reported that during the growth of GaN on selectively N^+ ion-implanted (111) Si substrate, polycrystalline GaN layer grown on the ion-

implanted region acts as a mask for ELO process due to its much slower growth rate compared to that of the laterally grown GaN from the non-implanted regions.[13] Thus, for the PCCES, due to the nanocrystalline GaN islands with limited growth rate, c-plane GaN from the planar region between cavity patterns laterally overgrows the nanocrystalline GaN islands on cavity patterns without interrupting by them. This scheme is expected to further reduce the threading dislocations in GaN layer compared to that grown on the conventional CES in which the undesired GaN was grown on the fully crystallized single crystalline α-Al_2O_3 shell. The morphological evolution and characteristics of the GaN layers on the PCCES were investigated in detail compared to the conventional fully crystallized CES (FCCES).

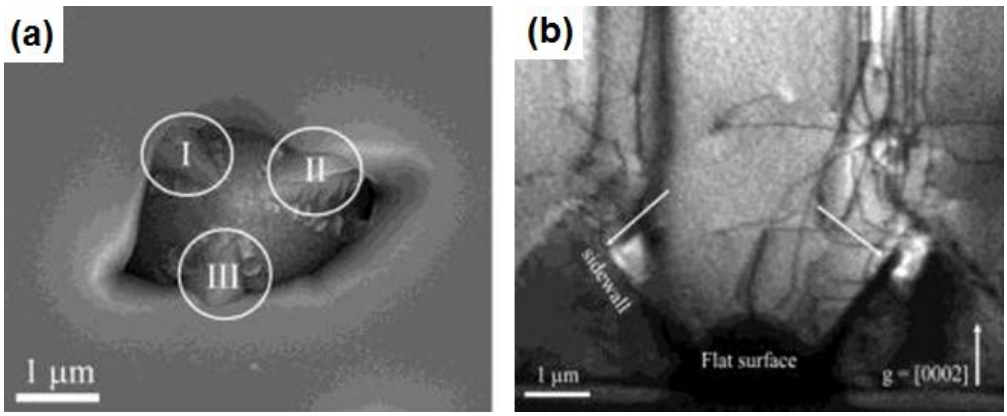

Figure 6.1 (a) SEM image of GaN layer grown on PSS for 30 min with growth rate of 2.2 μm/h. (b) and TEM image of the corresponding fully coalesced GaN layer, which are reported by Huang et al..[5]

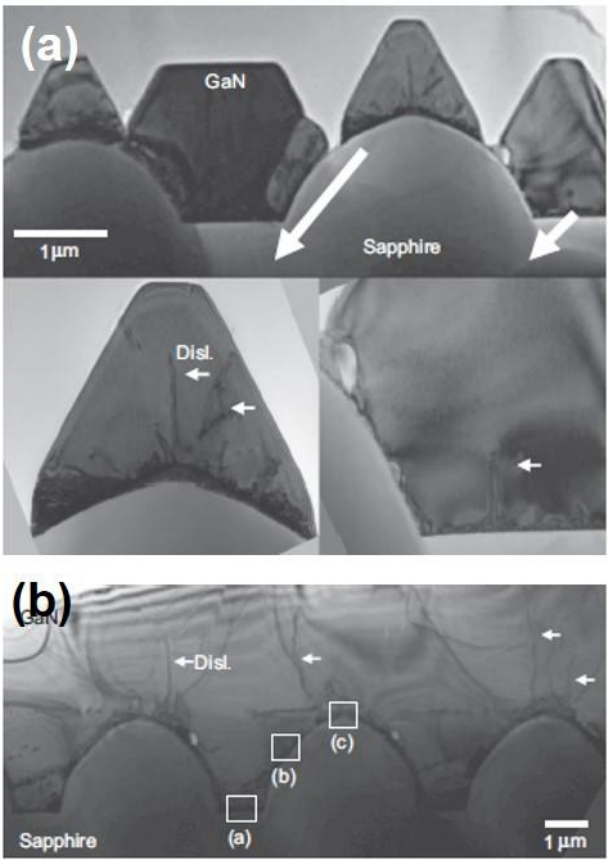

Figure 6.2 TEM images of the (a) middle and (b) final growth stages of the GaN layer grown on cone-shaped PSS, which were reported by Shin et al..[7]

6.2 Experimental details

The schematic diagram for the fabrication of PCCES is shown in Fig. 6.3. The process follows the fabrication procedure of the CES including photo resist (PR) patterning of a hemispherical shape with hexagonal-array on a c-plane sapphire substrate and atomic layer deposition (ALD) of amorphous alumina at 110 ^{o}C for 1000 cycles on the PR patterned substrate. The diameter and spacing of the PR pattern were 2 μm and 1 μm, respectively. During the ALD, amorphous alumina layer was deposited on not only the PR patterns but also the bare sapphire substrate between the PR patterns. Then, an annealing was performed using air ambient furnace to burn out the PR and crystallize the amorphous alumina layer. For the PCCES, the annealing was performed at 850 ^{o}C for 1 hr and subsequently at 1150 ^{o}C for 10 min. For a comparison, the FCCES was also fabricated by performing the annealing at 850 ^{o}C for 1 hr and subsequently at 1150 ^{o}C for 2 hours.

GaN layers were grown on the PCCES and FCCES in a same batch using a Thomas Swan 3x2" metalorganic chemical vapor deposition system. Precursors for Ga and N were Trimethylgallium and ammonia, respectively and H_2 was used as a carrier gas. A thermal cleaning was performed for 5 min at 1100 ^{o}C, and the temperature was then decreased to 560 ^{o}C at which a low temperature GaN buffer layer was grown at 13.3 kPa for 220 s. The high temperature GaN epitaxial layers were grown at 1040 ^{o}C and 40.0 kPa with different growth time. The morphological evolution of the samples was observed by a Hitachi S-4800 field emission scanning electron microscope (FESEM) operated at 15 kV. The microstructure and crystallographic phase

were investigated by transmission electron microscope (TEM), JEM-2100F operated at 200 kV. The TEM specimens were made using a focused ion beam (FIB). During the FIB process, Cr metal and carbon were used as a protective layer, which prevented surface damages from the Ga beam. Cathodoluminescence (CL) was measured using a Gatan MonoCL4 operated at 5 kV. For the measurement of reverse leakage current, circular Schottky diodes was fabricated on un-doped GaN layer using Ni/Au as a Schottky contact and Ti/Al/Ni/Au (annealed at 900 ^{o}C for 60 s) as a ohmic contact. I-V measurement of the Schottky diodes was performed using a KEITHLEY 2636A.

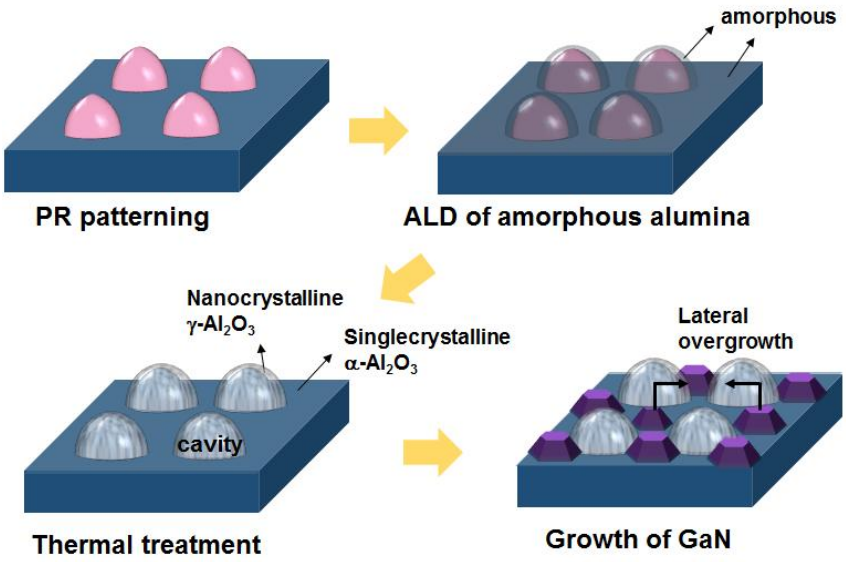

Figure 6.3 Schematic diagram for the formation of PCCES and subsequent lateral overgrowth of GaN.

6.3 Microstructure of the partially and fully crystallized CES

For the fabrication of PCCES, the annealing was performed at 850 ^{o}C for 1 hr and subsequently at 1150 ^{o}C for 10 min. As discussed in **Chapter 3 and 4**, SPE of the amorphous alumina proceeds in two step transformation of amorphous to metastable γ-Al_2O_3 and then subsequently into α-Al_2O_3. During the annealing at 850 ^{o}C for 1 hr, it was found that SPE into the intermediate γ-Al_2O_3 firstly proceeded in the planar area between the cavity patterns from the sapphire substrate and during the SPE, random nucleation of γ-Al_2O_3 also occurs at the upper part of cavity shell, remaining the cavity shell as a nanocrystalline γ-Al_2O_3 as shown in the Fig. 2.13. During the subsequent annealing at 1150 ^{o}C in order to transform the γ-Al_2O_3 into the α-Al_2O_3 through SPE, we could keep the upper area of the alumina shell as the nanocrystalline γ-Al_2O_3 by performing the annealing only for 10 min. Figure 6.4 (a) shows cross-section bright-field TEM image of the PCCES along the zone axis of $<11\text{-}20>_{\alpha\text{-}Al2O3}$. It was found that the SPE into α-Al_2O_3 was proceeded only up to the lower part of the alumina shell as marked by red arrows in Fig. 6.4 (a) while the rest of alumina shell was observed to be nanocrystalline phase. Figure 6.4 (b) and (c) show selected area diffraction patterns (SADPs) obtained at the planar area between cavity patterns and the top area of alumina cavity shell, respectively. The regions where SADPs were obtained are marked by dotted red (planar area) and blue (the top area of alumina cavity shell) circles in Fig. 6.4 (a). For the Fig. 6.4 (b), the SADP

aperture only included the crystallized alumina region through the SPE except for the underlying sapphire substrate. As shown in Fig. 6.4 (b), the SADP revealed that the planar alumina layer was epitaxially crystallized into single crystalline α-Al_2O_3 with c-axis along the surface normal, which showed same crystallographic orientation with the sapphire substrate. In comparison, it was revealed that the upper part of alumna cavity shell was nanocrystalline γ-Al_2O_3 as shown in Fig. 6.4 (c). The electron diffraction spots corresponding to the {440} and {400} plane of γ-Al_2O_3 was dominantly observed.

For a comparison, FCCES was also fabricated by performing the annealing at 850 ^{o}C for 1 hr and subsequently at 1150 ^{o}C for 2 hrs. Fig. 6.4 (d) shows cross-section bright-field TEM image of the FCCES along the zone axis of $<11\text{-}20>_{\alpha\text{-}Al2O3}$. During the annealing at 1150 ^{o}C, random nucleation of α-Al_2O_3 did not occur and resultantly the nanocrystalline γ-Al_2O_3 cavity shell was fully crystallized into the α-Al_2O_3 by SPE. Figure 6.4 (e) and (f) show SADPs obtained at the planar area between cavity patterns and the top area of the alumina cavity shell, respectively, which confirms that the whole cavity structure was crystallized into single crystalline α-Al_2O_3 following crystallographic orientation of the sapphire substrate.

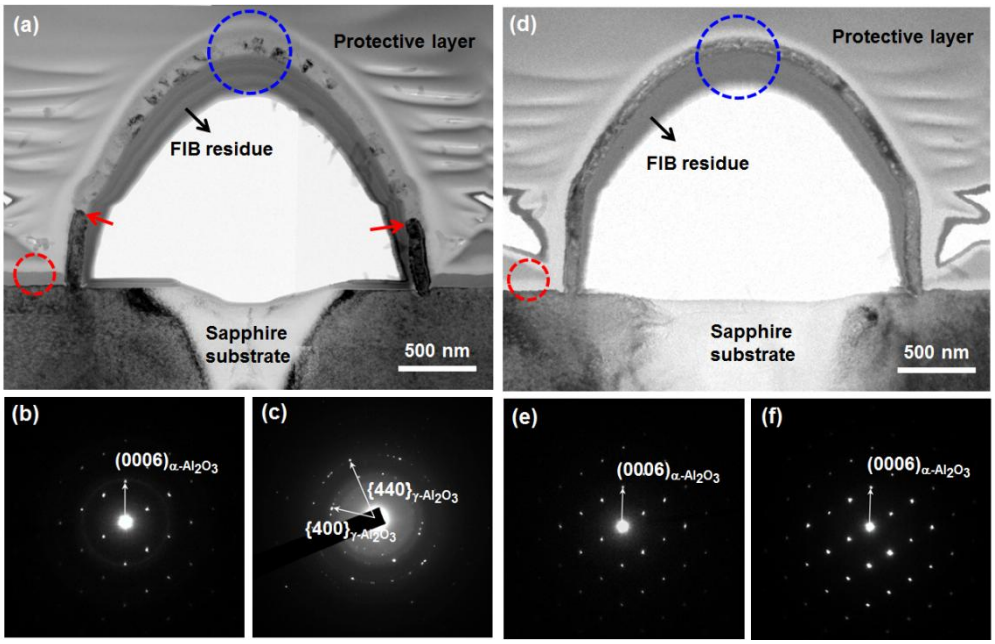

Figure 6.4 Cross-section TEM bright-field image of the (a) PCCES and (d) FCCES recorded at the <11-20>$_{sapphire}$ zone axis. SADPs obtained from the planar area between the cavity patterns for the (b) PCCES and (e) FCCES as marked with dotted red circles in Fig. 2 (a) and (d), respectively. SADPs obtained from the upper part of alumina cavity shell for the (c) PCCES and (f) FCCES marked with dotted blue circle in Fig. 2 (a) and (d), respectively.

6.4 Growth of GaN epitaxial layer on partially and fully crystallized CES

The morphological evolution of the GaN film grown on the FCCES and PCCES was investigated. SEM images of the GaN films grown on FCCES for 30, 45, 60, and 120 min are shown in Fig. 6.5(a), (b), (c), and (d) respectively. The insets in Fig. 6.5(a)-(c) are magnified top views at the apex of cavity patterns. It was observed that GaN crystals were grown on the side wall and the vertex area of the cavity patterns as well as planar area between cavity patterns as shown in the Fig. 6.5(a). Some GaN crystals on the vertex area became larger surrounded by {1-101} facets as shown in the inset in Fig. 6.5(b) and the GaN from the planar region was laterally overgrowing the cavity pattern with {11-22} facets.[14-15] As the growth proceeded, the GaN layer grown from the planar region merges with GaN grown on the vertex area and consequently the lateral movement of {11-22} facet was interrupted, leaving irregular shape of pits at the coalescence points as shown in the inset of Fig. 6.5(c).

Fig. 6.6(a)-(d) show SEM images of GaN film grown on PCCES for 30, 45, 60, and 120 min, respectively. Preferential GaN growth was inhibited on the pattern surface, indicating that the favorable growth planes for GaN did not appear on the surface of nanocrystalline γ-Al_2O_3. Instead, nano-scale GaN islands with irregular polyhedral shape were formed on the pattern surface as shown in the insets in Fig. 6.6(a)-(c), the magnified top views at the cavity patterns, indicating that the nanocrystalline form of GaN was grown on the

cavity shell. Note that growth rate of the nanocrystalline GaN islands was much slower than that of c-plane GaN from the planar region and the progress of lateral overgrowth was not interrupted by them.[13] As a result, the c-plane GaN from the planar region laterally overgrows the whole cavity patterns without disturbance while maintaining symmetry of the {11-22} side facets and then, the GaN film was coalesced at the apex of the pattern as shown in Fig. 6.6 (c). After the growth of 120 min, pit-free smooth surface was obtained for GaN layers both on the FCCES and PCCES as shown in Fig. 6.5(d) and Fig. 6.6(d), respectively.

Figure 6.7(a) shows the cross-section TEM bright-field image of the GaN grown on FCCES for 30 min, which was recorded at the $<11\text{-}20>_{GaN}$ zone axis. To compare the crystallographic orientations between the GaN grown on the planar region between cavity patterns and that grown on the vertex area of cavity patterns, SADPs of corresponding GaN regions (marked with 1 and 2 in Fig. 4 (a), respectively) were obtained as shown in Fig. 6.7(b) and (c), respectively. The both diffraction patterns revealed the c-plane GaN. The arrow in the Fig. 6.7(b) indicates the c-direction at the region 1 and for comparison, the duplicated arrow was presented in the SADP of region 2 as shown in Fig. 6.7(c). It was found that the c-axes of the GaNs were rotated counter-clockwise by ~ 2 ^{o} with respect to each other around the <11-20> zone axis. This implies that the crystallographic orientation between the vertex area and sapphire substrate is not perfectly identical. Fig. 6.7(d) and (e) show SADPs obtained at the sapphire substrate and the vertex area, respectively. The arrow in Fig. 6.7(d) indicates the c-direction of the sapphire substrate and the duplicated arrow is presented in Fig. 6.7(e). We confirmed

that the alumina shell at the vertex area was crystallized following the crystallographic orientation of the sapphire substrate but there is misorientation of ~ 2 ^{o} between the c-direction of the sapphire substrate and that of the vertex area. Fig. 6.7(f) is SADP at the region 3 (marked in Fig. 4 (a)) containing both the side wall of the cavity pattern and GaN grown on it. The c-direction of the GaN was faced towards the surface normal of the side wall and the diffraction spot of $\{0002\}_{GaN}$ was parallel to that of $\{11\text{-}23\}_{Al_2O_3}$, indicating that the c-plane GaN was grown on a {11-23} n-plane pattern surface. It was reported that epitaxial c-plane GaN can be grown on an n-plane sapphire substrate.[12] This result implies that if sapphire planes in which GaN can be grown, such as c-, a-, m-, r-, and n-plane, is exposed on the surface of alumina cavity shell, the undesired GaN growth can occur on the surface as shown in Fig. 6.8. In our growth condition, thermodynamically less favorable non- or semi-polar GaN growth on the pattern surface (e.g., a-plane GaN on r-plane Al_2O_3)[16] was not observed.

Figure 6.9(a) shows the cross-section TEM image of GaN crystals grown on PCCES for 30 min. The TEM image was recorded at the $<11\text{-}20>_{GaN}$ zone axis. Preferential GaN growth occurred only at the planar region between cavity patterns which had been transformed into single crystalline α-Al_2O_3 by SPE. Fig. 6.9(b) shows SADP obtained at the interface region between GaN and the planar SPE α-Al_2O_3 region marked by red dotted circle in Fig. 6.9(a), confirming the epitaxial relationship of $\{0002\}_{GaN}//\{0006\}_{\alpha\text{-}Al2O3}$. On the cavity pattern, no large size GaN crystal on the top but nanocrystalline GaN islands with thickness of ~ 20 nm was found. To

investigate the nanocrystalline GaN islands on the alumina shell, SADP at the top area of the cavity pattern (marked region by dotted blue circle in Fig. 6.9(a)) was obtained as shown in Fig. 6.9(c). The randomly oriented electron diffraction spots indicates the nanocrystalline phase of the GaN and alumina shell. Besides electron diffraction spots from the {400}, and {440} plane of γ-Al_2O_3, those corresponding to {10-10}, {10-12}, and {11-22} planes of hexagonal GaN were found as indicated in Fig. 6.9(c), confirming the nanocrystalline GaN islands.

The nanocrystalline GaN islands were investigated by HRTEM analysis. Figure 6.10(a) shows TEM bright-field image of the GaN layer grown on PCCES for 45 min, showing GaN islands grown on the nanocrystalline cavity shell. Figure 6.10(b) and (c) show HRTEM image and its fast fourier transform (FFT) electron diffraction pattern of the GaN island marked by dotted red squares in Fig. 6.10(a). The FFT electron diffraction pattern revealed that hexagonal GaN island was grown on the γ-Al_2O_3 grain.

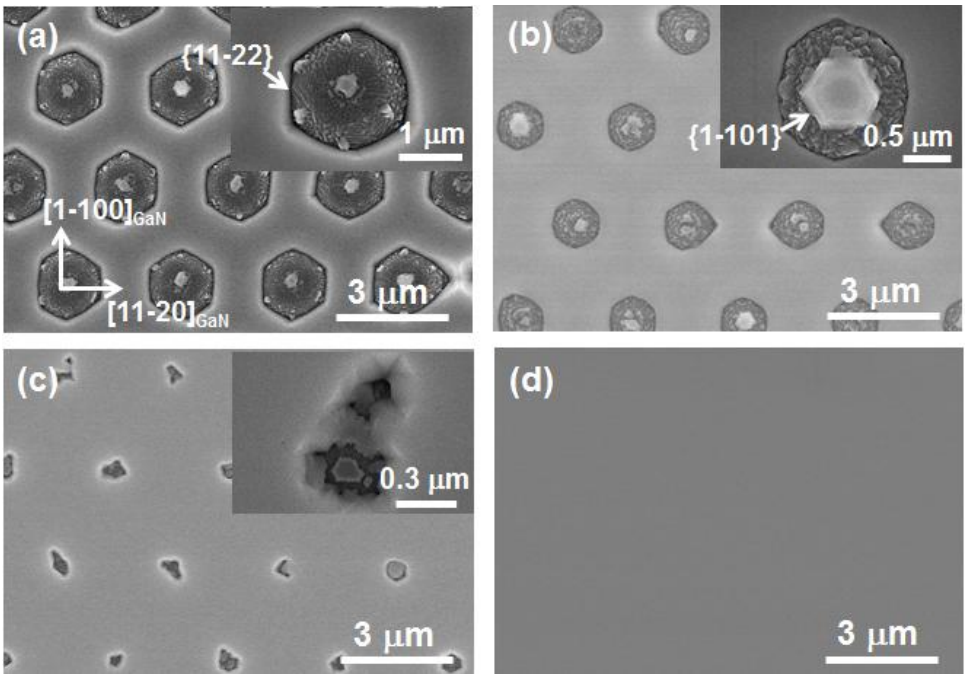

Figure 6.5 SEM images of the morphological evolution of the GaN epitaxial layers grown on FCCES for (a) 30 min, (b) 45 min, (c) 60 min, and (d) 120 min. The insets in Fig. 6.5(a)-(c) show the magnified top views at the apex of cavity patterns.

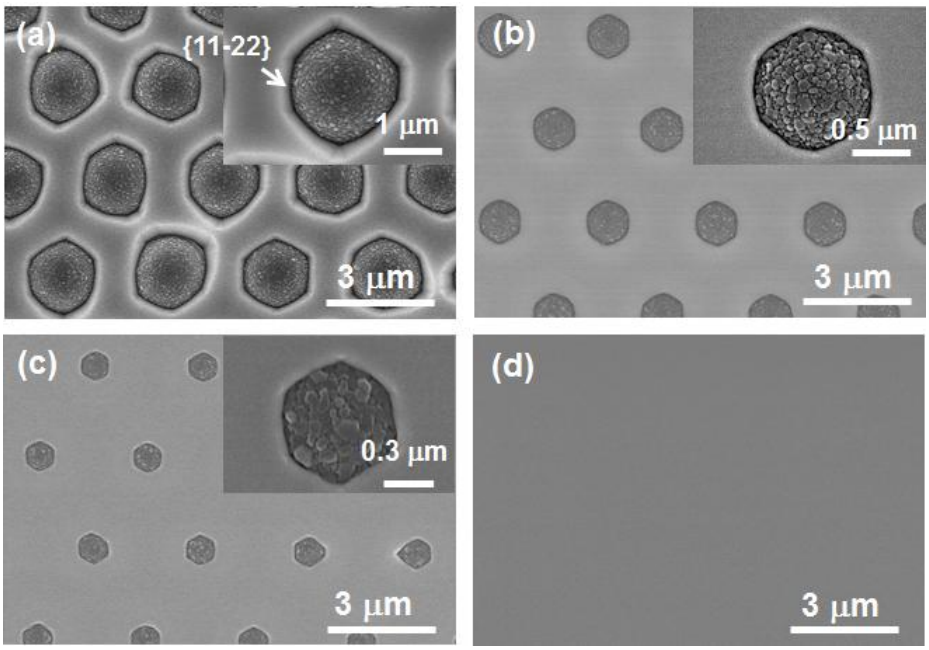

Figure 6.6 SEM images of the morphological evolution of the GaN epitaxial layers grown on PCCES for (a) 30 min, (b) 45 min, (c) 60 min, and (d) 120 min. The insets in Fig. 6.6(a)-(c) show the magnified top views at the apex of cavity patterns.

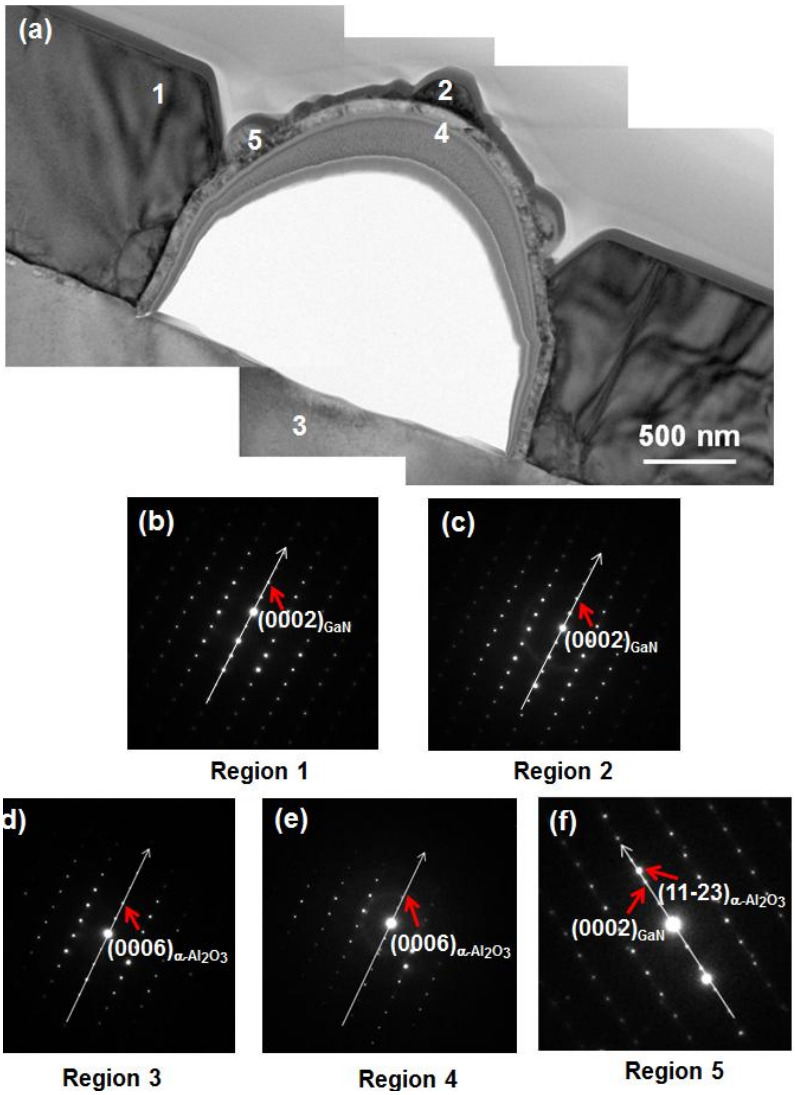

Figure. 6.7 (a) TEM bright-field image of the GaN epitaxial layer grown on FCCES for 30 min recorded at the <11-20>$_{GaN}$ zone axis. SADPs obtained at region (b) 1, (c) 2, (d) 3, (e) 4, and (f) 5 as marked in Fig. 6.8(a).

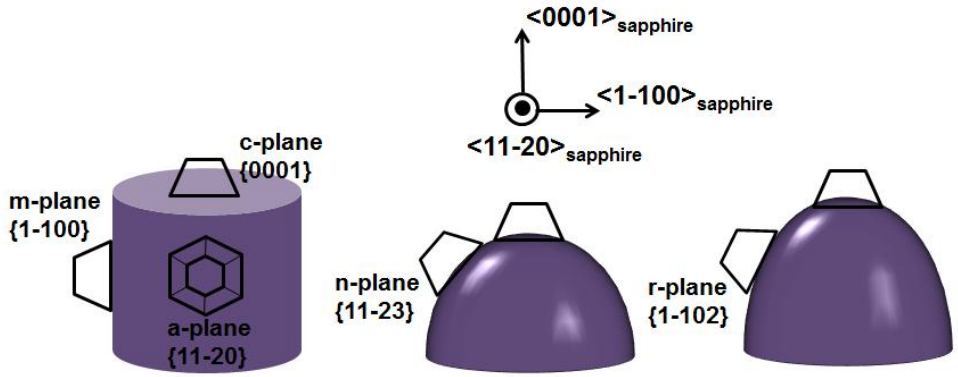

Figure 6.8 Schematic diagram for local surface planes of the fully crystalized alumina cavity pattern where the parasitic GaN can be grown.

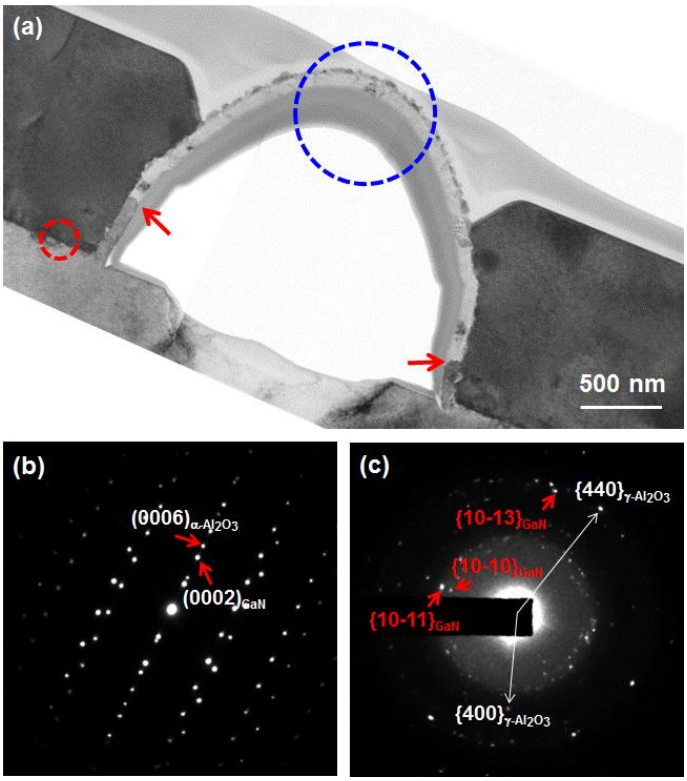

Figure 6.9 (a) TEM bright-field image of the GaN epitaxial layer grown on PCCES for 30 min recorded at the <11-20>$_{GaN}$ zone axis. SADPs obtained at (b) the interface region between the GaN and the planar SPE α-Al_2O_3 layer between the cavity patterns and (c) the vertex area of the cavity pattern containing the alumina cavity shell and nano-scale GaN islands on it.

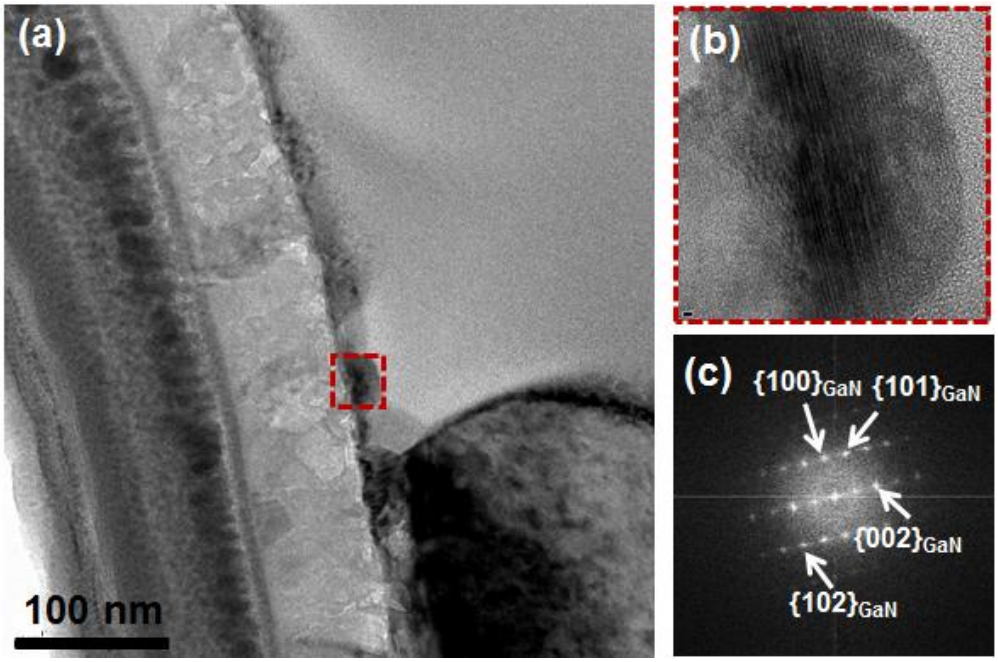

Figure 6.10 (a) TEM bright-field image of the GaN layer grown on PCCES for 45 min, showing GaN islands grown on the nanocrystalline cavity shell. (b) HRTEM images of the GaN islands marked by dotted red square in Fig. 6.10(a) (c) FFT electron diffraction patterns from HRTEM images of the GaN islands in Fig. 6.10(b)

6.5 Characteristics of GaN layers on partially and fully crystallized CES

To investigate the threading dislocations in fully coalesced GaN layers, TEM analysis was performed for the fully coalesced GaN layers grown on the FCCES and PCCES for 2 hours. Figure 6.11 (a) shows TEM bright-field image of the GaN layers on FCCES recorded at the $[11\text{-}20]_{GaN}$ zone axis and more magnified TEM two-beam bright-field images with g = [1-100] and [0002] were obtained above the vertex area of the cavity patterns as shown in Fig. 6.11(b) and (c), respectively. The corresponding TEM images for the GaN layer on PCCES were shown in Fig. 6.12(a), (b), and (c). For the GaN layer on FCCES, it was found that a number of threading dislocations, which are originated from the vertex area of cavity pattern, thread up to the coalesced GaN surface. This indicates that the undesired threading dislocations are additionally generated during the merging process above the vertex area of pattern. The vertex area where the dislocations are generated corresponds to that where the tilted c-GaN was grown (Fig. 6.5(b)). On the other hand, for the GaN layer on PCCES, it should be noted that one threading dislocation with a+c type was observed above the apex of cavity pattern. Since the GaN layer was coalesced right at the apex of the cavity pattern as shown in Fig. 6.6(c), it is inferred that the observed threading dislocation was originated from the coalescence of the GaN layers above the pattern, which is inevitable during the merging process.[17] In other words, no additional threading dislocation was generated during the merging process except for that created at the coalescence point in our observation. For both

GaN layers on FCCES and PCCES, there was no observable generation of threading dislocations for the laterally overgrown GaN region above the side wall of cavity pattern. For the GaN on FCCES, higher population of threading dislocations above the patterns compared to that on PCCES can be comprehended from three reasons. At first, dislocations can be generated when the c-plane GaN growing from the planar region merges with that grown on the vertex area[5-6] because their crystallographic orientations were rotated each other as shown in Fig 6.8(b) and (c). Second reason is that the lateral growth was interrupted by the GaN on the top as shown in the inset of Fig. 6.5(c). In addition, dislocations themselves in GaN grown on the vertex area, generated by the lattice mismatch between the GaN and SPE-alumina shell, can thread up to the merging surface of a GaN layer.[7,8]

CL measurement was performed to study the distribution of the threading dislocations in the fully coalesced GaN layers grown on the FCCES and PCCES for 2 hrs as shown in Fig. 6.13(a) and (b), respectively. The dark spot densities of the GaN layers were 1 ~ 2 x 10^8 cm^{-2} for both samples. Note that a number of dark spots in the GaN layer on FCCES locally distributed in the specific positions. The position of the gathered dark spots corresponds to that of hexagonal-arrayed cavity patterns with period of 3 μm, which is consistent with the TEM results. In contrast, more or less uniformly distributed dark spots were observed at the GaN layer grown on PCCES as shown in Fig. 6.13(b).

In order to investigate the effect of distribution of the threading dislocations on electrical characteristic of the GaN layers, a reverse leakage current was measured for 8 GaN Schottky diodes on FCCES and PCCES.

Figure 6.14 shows the representative plot of current density as a function of reverse bias voltage and the inset is cross-section schematic structure of the circular Schottky diode. At the applied reverse voltage of -3 V, average current densities of the Schottky diodes on FCCES and PCCES were 7.4 x 10^{-3} A/cm^2 and 7.3 x 10^{-4} A/cm^2, respectively. The reverse leakage current for the Schottky diode on PCCES was reduced by one order of magnitude compared to that on FCCES. It has been suggested that threading dislocations are localized leakage current sources in GaN and tunneling through trap states related to dislocation is responsible for the leakage current.[18-22] For the GaN on FCCES, the higher leakage current is susceptible to the local high density of threading dislocations above the cavity pattern shown in Fig. 6.11 and Fig. 6.13.[23] Thus, the improved electrical characteristic of the GaN layer on PCCES was attributed to the suppression of the additional generation of threading dislocations in the top region above the cavity patterns.

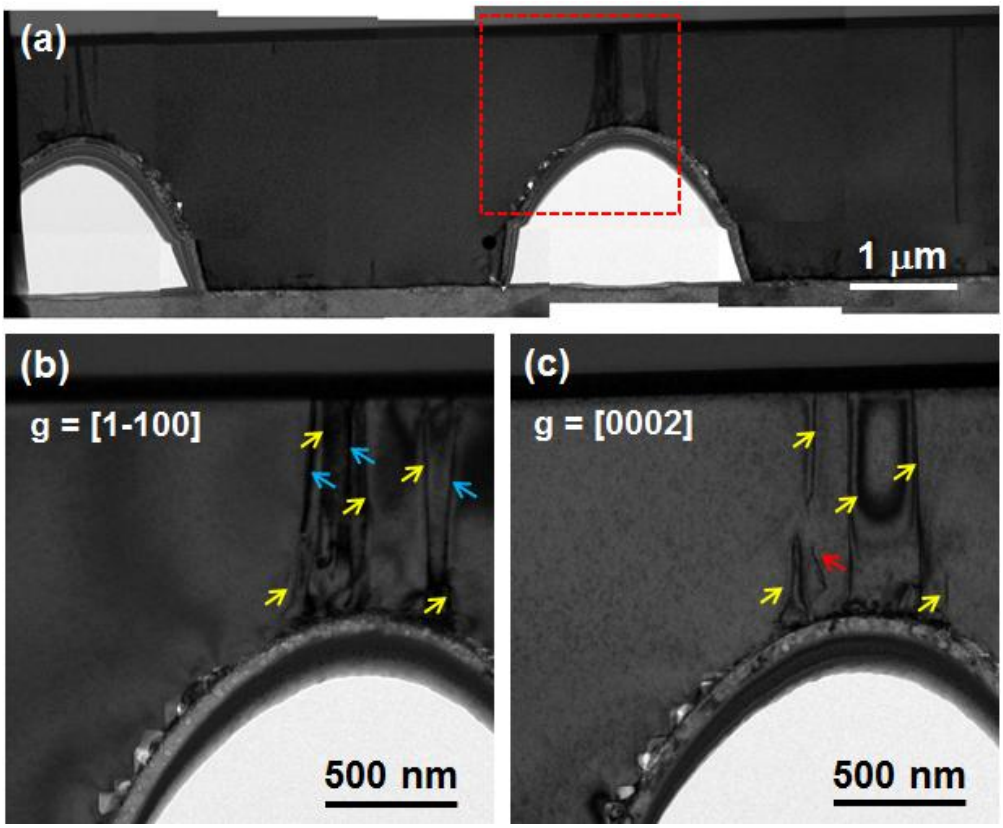

Figure 6.11 (a) TEM bright-field images of the fully coalesced GaN epitaxial layer grown on FCCES for 2 hours, which was recorded at the $[11\text{-}20]_{GaN}$ zone axis. More magnified TEM two-beam bright-field images obtained above the vertex area of the cavity patterns with (b) g = [1-100] and (c) g = [0002]. Yellow, blue, and red arrows in the figure indicate the a+c type (visible both at g = [1-100] and [0002]), a type (visible at g = [1-100]), and c type (visible at g = [0002]) dislocations, respectively.

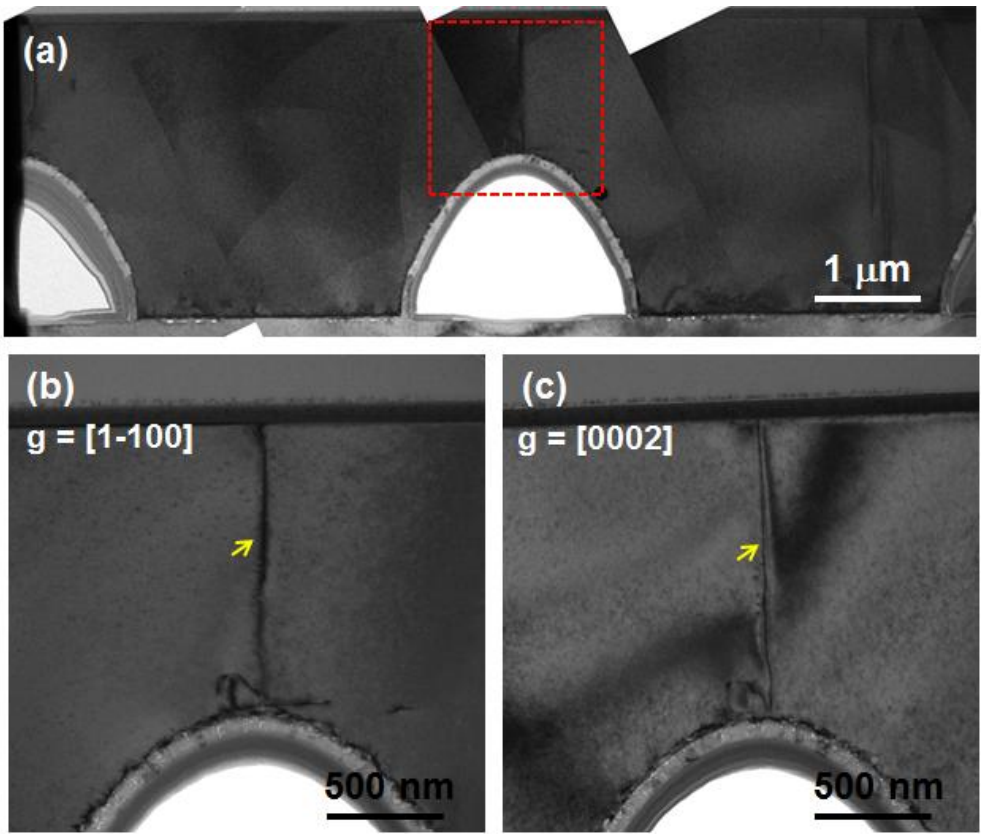

Figure 6.12 (a) TEM bright-field images of the fully coalesced GaN epitaxial layer grown on PCCES for 2 hours, which was recorded at the $[11\text{-}20]_{GaN}$ zone axis. More magnified TEM two-beam bright-field images obtained above the vertex area of the cavity patterns with (b) g = [1-100] and (c) g = [0002]. Yellow arrow in the figure indicate the a+c type (visible both at g = [1-100] and [0002]) dislocation.

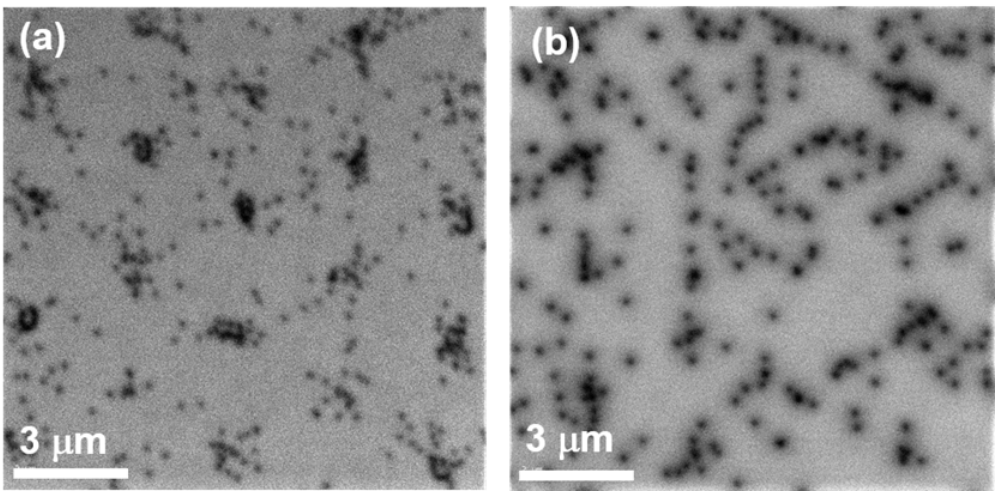

Figure 6.13 Plan-view CL images of the fully coalesced GaN epitaxial layers grown on the (a) FCCES and (b) PCCES for 2 hours.

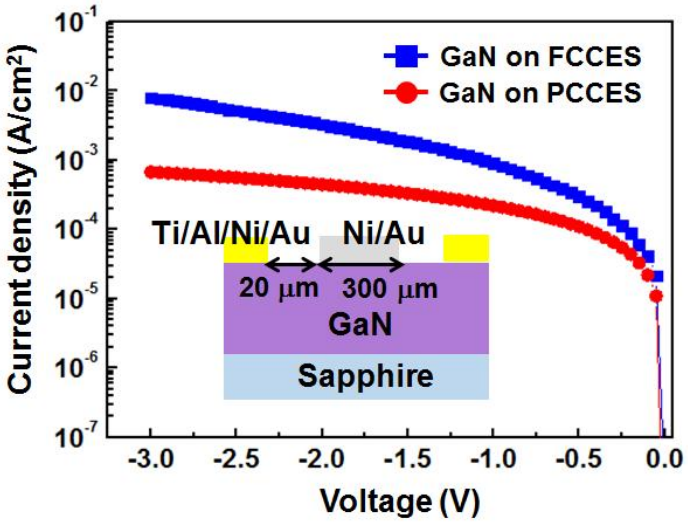

Figure 6.14 Current density vs applied voltage for the GaN Schottky diodes prepared on the FCCES and PCCES. The inset shows cross-section schematic diagram of the circular GaN Schottky diode.

6.6 Summary

We proposed growth of GaN layer on a partially crystallized cavity engineered sapphire substrate (PCCES) in which cavity patterns were arrayed on a sapphire substrate and only planar region between the patterns serves as growth template of c-plane sapphire. Because alumina shell surrounding the cavities consisted of nanocrystalline γ-Al_2O_3, nanocrystalline GaN islands were formed on the pattern surface rather than parasitic growth of GaN, which generates the additional threading dislocations during the merging process above the patterns. Due to the limited growth rate of the nanocrystalline GaN islands, c-plane GaN from the planar region between cavity patterns laterally overgrows the cavity patterns and the additional generation of threading dislocations was not observed during the merging process except for that created at a coalescence point. The TEM and CL analysis revealed that for the GaN layer grown on PCCES there are fewer threading dislocations in the GaN region above the cavity patterns compared to that on the FCCES in which single crystalline alumina shell serves the local growth planes for the parasitic GaN. As a result, reverse leakage current for the GaN Schottky diode on PCCES was reduced by one order of magnitude compared to that on FCCES.

6.7 Bibliography

1. Haiyong Gao, Fawang Yan, Yang Zhang, Jinmin Li, Yiping Zeng, and Guohong Wang, Enhancement of the light output power of InGaN/GaN light-emitting diodes grown on pyramidal patterned sapphire substrates in the micro- and nanoscale, Journal of Applied Physics 103, 014314 (2008)

2. Jae-Hoon Lee, Dong-Yul Lee, Bang-Won Oh, and Jung-Hee Lee, Comparison of InGaN-Based LEDs Grown on Conventional Sapphire and Cone-Shape-Patterned Sapphire Substrate, IEEE TRANSACTIONS ON ELECTRON DEVICES 57,157-163 (2010)

3. Jeonghwan Jang, Daeyoung Moon, Hyo-Jeong Lee, Donghyun Lee, Daehan Choi, Dukkyu Bae, Hwankuk Yuh, Youngboo Moon, Yongjo Park, Euijoon Yoon, Incorporation of air-cavity into sapphire substrate and its effect on GaN growth and optical properties, Journal of Crystal Growth 430, 41–45 (2015)

4. Yoon-Jong Moon, Daeyoung Moon, Jeonghwan Jang, Jin-Young Na, Jung-Hwan Song, Min-Kyo Seo, Sunghee Kim, Dukkyu Bae, Eun Hyun Park, Yongjo Park, Sun-Kyung Kim, and Euijoon Yoon, Microstructured Air Cavities as High-Index Contrast Substrates with Strong Diffraction for Light-Emitting Diodes, Nano Letters 16, 3301-3308 (2016)

5. Xiao-Hui Huang, Jian-Ping Liu, Jun-Jie Kong, Hui Yang, and Huai-Bing Wang, High-efficiency InGaN-based LEDs grown on patterned sapphire substrates, Optics express 19, A949 (2011)

6. Hongpo Hu, Shengjun Zhou, Xingtong Liu, Yilin Gao, Chengqun Gui, and Sheng Liu, Effects of GaN/AlGaN/Sputtered AlN nucleation layers on

performance of GaN-based ultraviolet light-emitting diodes, Scientific reports 7, 44627 (2017)

7. Hui-Youn Shin, S. K. Kwon, Y. I. Chang, M. J. Cho, K. H. Park, Reducing dislocation density in GaN films using a cone-shaped patterned sapphire substrate, Journal of Crystal Growth 311, 4167–4170 (2009)

8. Hung-Cheng Lin, Hsueh-Hsing Liu, Geng-Yen Lee, Jen-Inn Chyi, Chang-Ming Lu, Chih-Wei Chao, Te-Chung Wang, Chun-Jong Chang, and Solomon W. S. Chi, Effects of lens shape on GaN grown on microlens patterned sapphire substrate by metalorganic chemical vapor deposition, Journal of the electrochemical society 157, H304-H307 (2010)

9. Dae-sik Kim, Woo Seop Jeong, Hyungduk Ko, Jae-Sang Lee, and Dongjin Byun, Pretreatment by selective ion-implantation for epitaxial lateral overgrowth for GaN on patterned sapphire substrate, Thin Solid Films, Online publication (2017)

10. N. Grandjean, J. Massies, Y. Martinez, P. Vennegues, M. Leroux, M. Laugt, GaN epitaxial growth on sapphire (0 0 0 1): the role of the substrate nitridation, Journal of Crystal Growth 178, 220-228 (1997)

11. D. Doppalapudi, E. Iliopoulos, S. N. Basu, and T. D. Moustakas, Epitaxial growth of gallium nitride thin films on A-Plane sapphire by molecular beam epitaxy, Journal of Applied Physics **85**, 3582 (1999)

12. Masaki Takami, Akihiro Kurisu, Yuki Abe, Narihito Okada, and Kazuyuki Tadatomo, Growth of semipolar {10-11} GaN from *c*-plane-like sapphire sidewall of patterned *n*-plane sapphire substrate, Phys. Status Solidi C **8**, 2101–2103 (2011)

13. Bumjoon Kim, Kwangtaek Lee, Samseok Jang, Junggeun Jhin, Seungjae

Lee, Jonghyeob Baek, Youngmoon Yu, Jaesang Lee, and Dongjin Byun, Epitaxial lateral overgrowth of GaN on Si (111) substrates using high-dose N+ ion implantation, Chemical Vapor Deposition **16**, 80-84 (2010)

14. Danxu Du, David J. Srolovitz, Michael E. Coltrin, and Christine C. Mitchell, Systematic Prediction of Kinetically Limited Crystal Growth Morphologies, Phys. Rev. Lett. 95, 155503 (2005)

15. Qian Sun, Christopher D. Yerino, Benjamin Leung, Jung Han, and Michael E. Coltrin, Understanding and controlling heteroepitaxy with the kinetic Wulff plot: A case study with GaN, Journal of Applied Physics 110, 053517 (2011)

16. Narihito Okada, Akihiro Kurisu, Kazuma Murakami, and Kazuyuki Tadatomo, Growth of Semipolar (11-22) GaN Layer by Controlling Anisotropic Growth Rates in *r*-Plane Patterned Sapphire Substrate, Applied Physics Express **2**, 091001 (2009)

17. Kyu-Seung Lee, Ho-Sang Kwack, Jun-Seok Hwang, Tae-Moo Roh, Yong-Hoon Cho, Jae-Hoon Lee, Yong-Chun Kim, and Chang Soo Kim, Spatial correlation between optical properties and defect formation in GaN thin films laterally overgrown on cone-shaped patterned sapphire substrates, Journal of Applied Physics **107**, 103506 (2010)

18. J. W. P. Hsu, M. J. Manfra, D. V. Lang, S. Richter, S. N. G. Chu, A. M. Sergent, R. N. Kleiman, and L. N. Pfeiffer, Inhomogeneous spatial distribution of reverse bias leakage in GaN Schottky diodes, Applied Physics Letters 78, 1685-1687 (2001)

19. D. S. Li, H. Chen, H. B. Yu, H. Q. Jia, Q. Huang, and J. M. Zhou, Dependence of leakage current on dislocations in GaN-based light-emitting

diodes, Journal of applied physics 96, 1111-1114 (2004)
20. E. G. Brazel, M. A. Chin, and V. Narayanamurti, Direct observation of localized high current densities in GaN films, Applied Physics Letters 74, 2367-2369 (1999)
21. Bumho Kim, Daeyoung Moon, Kisu Joo, Sewoung Oh, Young Kuk Lee, Yongjo Park, Yasushi Nanish, and Euijoon Yoon, Investigation on leakage current paths in n-GaN by conductive atomic force microscopy, Applied Physics Letters 104, 102101 (2014)
22. E. J. Miller, E. T. Yu, P. Waltereit, and J. S. Speck, Analysis of reverse-bias leakage current mechanisms in GaN grown by molecular-beam epitaxy, Applied Physics Letters 84, 535-537 (2004)
23. Fuxue Wang, Hai Lu, Xiangqian Xiu, Dunjun Chen, Rong Zhang, and Youdou Zheng, Dislocation clustering and luminescence nonuniformity in bulk GaN and its homoepitaxial film, Journal of Electronic Materials **39**, 2243-2247 (2010)

Chapter 7. Conclusion

A new growth scheme using a cavity engineered sapphire substrate (CES), in which a two-dimensionally patterned cavity array is incorporated into the interface between the GaN and sapphire substrate, was studied. At first, the CES was fabricated by following procedure, photoresist patterning on a sapphire substrate, deposition of amorphous alumina layer by atomic layer deposition, and thermal treatment in air ambient furnace. We confirmed that well-defined alumina cavity pattern was successfully formed on a c-plane sapphire substrate. Also, the amorphous alumina layer was crystallized into single crystalline α-phase from the sapphire substrate by solid-phase epitaxy (SPE), indicating that the CES can act as a substrate for the epitaxial growth of GaN. This implies that crystalline quality of the GaN layer could be dependent on the characteristics of the SPE α-Al_2O_3, which arouses the importance of the fundamental understanding on the SPE mechanism.

Accordingly, SPE behavior of the 3-dimensional amorphous alumina membrane structure was investigated using stripe-shaped amorphous alumina membrane structure on a sapphire substrate. It was found that the SPE proceeded through 2 step phase transformation from amorphous to γ-Al_2O_3 and then subsequently into α-Al_2O_3. Beside SPE of γ-Al_2O_3 at the interface between the amorphous alumina layer and sapphire substrate, random nucleation of γ-Al_2O_3 were occurred in the upper part of the membrane, resulting in the nanocrystalline γ-Al_2O_3 shell. However, in our investigation condition, random nucleation of α-Al_2O_3 was not observed during the subsequent phase transformation from γ- to α-phase, resulting that the whole

alumina membrane was transformed into α-Al_2O_3 by SPE. During the phase transformations, the membrane structure was contracted by the density increase of alumina, which induces stresses and deflections in the membrane structure. These resulted in the enhanced SPE ($\gamma \rightarrow \alpha$) at the corner region of the membrane structure and rotation of c-axis in the top layer of the membrane structure with respect to the sapphire substrate. Furthermore, kinetics of the SPE procedure was investigated by precise measurement of the SPE rate using TEM analysis. Activation energy of the SPE from amorphous to γ-phase and that from γ- to α-phase were obtained as 3.09 eV and 3.92 eV, respectively. In addition, SPE mechanism of the amorphous alumina into the intermediate γ-phase was investigated in detail by phase/orientation mapping using a scanning nanobeam diffraction technique of TEM. It was clearly revealed that the SPE γ-Al_2O_3 layer consisted of two stacking-mismatched domains, which can be distinguishable only at the specific projecting direction. More importantly, it was found that the growth of SPE γ-Al_2O_3 layers are strongly influenced by at least two stacking steps of oxygen-ion layers of the sapphire substrate near the interface. Accordingly, we suggested that presence of two non-identical surfaces terminated with AB and BA on the stepped {0001} α-Al_2O_3 surface results in the formation of γ-Al_2O_3 domains.

In order to investigate effect of incorporation of air cavities on the GaN-based LEDs, GaN epitaxial layer was grown and LED device was fabricated on the CES. The GaN film was observed to fill the spaces between the cavities at the initial stage of growth and then grow laterally over the cavities, leading to a completely coalesced pit-free smooth surface. CL dark spot density was reduced from 1.9×10^8 cm^{-2} to 1.4×10^8 cm^{-2}, demonstrating

that the threading dislocation density was reduced using the CES. Also, the existence of cavities was found to reduce the stress in the GaN film and wafer bow by ~30%. To evaluate LED performances, the output power of LED on CES was measured on wafer, showing 2.2 times higher value than that on the planar sapphire substrate at an input current of 20 mA. This indicates that the cavities at the interface significantly enhanced the light extraction efficiency.

Additionally, to suppress the undesired growth of GaN on the pattern surface of CES, we proposed growth of GaN layer on a partially crystallized CES (PCCES) in which only the planar region between the patterns was crystallized into single crystalline (0001) α-Al_2O_3 while the alumina shell surrounding the cavities remained in nanocrystalline γ-Al_2O_3 by controlling the crystallization process of the amorphous alumina cavity structure. Because the growth rate of the nanocrystalline GaN islands grown on the nanocrystalline alumina shells was much slower than that of c-plane GaN from the planar region, the progress of lateral overgrowth was not interrupted by the nanocrystalline GaN islands. For the GaN layer grown on PCCES, there is no additional generation of dislocations during the merging process above the cavity patterns while GaN on the conventional CES shows localized high density of threading dislocations in GaN region above the cavity patterns. As a result, reverse leakage current for the GaN Schottky diode on PCCES was reduced by one order of magnitude compared to that on the existing CES.

국 문 초 록

GaN 기반 발광다이오드 (Light-emitting diodes (LEDs))는 높은 효율과 긴 수명으로 인해 형광등이나 백열등과 같은 기존 조명의 대체품으로 각광받아 왔다. 하지만 이는 LED 조명의 높은 가격으로 인해 제한되고 있다. LED 제작을 위한 GaN 에피층 성장의 경우 대면적 동종기판의 부재로 인해 일반적으로 사파이어 기판을 이용한 헤테로에피택시에 의해 에피층 성장이 이루어지게 된다. 이 때 GaN 박막과 사파이어 기판과의 격자상수 차이에 의해 GaN 박막의 관통전위 밀도가 매우 높으며 또한 열팽창 계수 차이에 의해 에피성장 후 기판 휨 현상이 발생하게 된다. 뿐만 아니라, GaN 박막과 외부와의 높은 굴절률 차이에 의한 발광된 빛의 내부 전반사는 LED 소자의 광추출효율을 저하시키는 주요한 요인이 된다. 따라서 가격 절감을 위한 LED 의 효율 및 생산성 향상을 위해서는 이러한 기술적 문제점들을 해결해야 한다.

본 연구에서는 이러한 문제점들을 극복하기 위해 cavity engineered sapphire substrate (CES)를 이용하여 GaN 에피층과 사파이어 기판계면에 중공구조물을 도입하는 성장방법이 제안되었다. CES 의 제작을 위해 먼저 포토리소그래피를 이용하여 photoresist (PR) 패턴을 사파이어 기판 위에 형성한 후 원자층증착법을 이용하여 비정질 알루미나층을 PR 패턴된 사파이어

기판 위에 증착하였다. 그 후 PR 을 태워 제거하고 비정질 알루미나층을 고상에피택시를 통해 사파이어 기판과 같은 단결정 알파상으로 결정화 시키기 위해 퍼니스에서 열처리를 진행하였다. 그 결과 사파이어 기판 위에 규칙적으로 배열된 알루미나 중공 구조물이 잘 형성되어 있는 것을 확인하였다. 또한, 고상에피택시를 통해 비정질 알루미나층이 모두 단결정 알파상으로 결정화되어 그 위 GaN 에피성장이 가능함을 확인하였다. 그리고 이를 통해 성장될 GaN 에피층의 품질이 고상결정화된 알파상 알루미나의 특성에 의존할 것임을 알 수 있으며 따라서 CES 제작 과정 중 비정질 알루미나 멤브레인 구조물의 고상결정화를 이해하는 것이 필요하다.

이를 위해 stripe 모양의 비정질 알루미나 멤브레인 구조물을 제작한 뒤 열처리를 진행하여 고상결정화 과정을 연구하였다. 비정질 알루미나 구조물이 준 안정한 중간상인 감마상을 거쳐 알파상으로 결정화가 진행 되는 것이 확인되었다. 먼저 감마상으로의 결정화의 경우 사파이어 기판과의 계면에서부터 고상에피택시가 진행되는 도중 위 쪽 멤브레인에서 핵생성이 일어나 나노결정질 감마상이 형성되었다. 하지만 알파상의 경우, 관찰온도에서 핵생성이 발생하지 않아 고상에피택시를 통해 구조물 전체가 사파이어 기판을 따라 단결정 알파상으로 결정화 되었다. 또한 결정화에 따른 알루미나의 밀도증가에 의한 구조물의 수축이 고상에피택시에 미치는 영향을 확인하였다. 뿐만 아니라,

투과주사현미경을 이용하여 정밀하게 고상에피택시의 속도를 측정하여 비정질에서 감마상 그리고 감마상에서 알파상으로의 고상에피택시 과정에서 각각 3.1 eV, 3.9 eV 의 활성화 에너지 값을 얻을 수 있었다. 그리고 나노빔 회절 스캐닝을 통한 phase/orientation mapping 을 이용하여 비정질에서 감마상 알루미나로의 결정화 과정을 상세히 연구하였다. 그 결과 고상에피택시를 통해 결정화된 감마상 알루미나가 적층 순서가 서로 다른 두 개의 도메인 구조로 이루어져 있는 것을 확인하였으며 이들이 특정 방향에서만 구분이 가능하다는 것을 보였다. 그리고 phase/orientation mapping 을 통한 도메인 구조의 분포를 통해 서로 다른 적층 순서를 가지는 스텝된 기판 표면이 도메인 구조의 생성원인이라는 것을 제시하였다.

중공 구조물 도입 효과를 확인하기 위해 CES 위 GaN 에피층 성장 및 LED 소자를 제작하였다. GaN 박막이 초기성장 단계에서 중공구조물 사이 공간을 채우고 중공 구조물 위로 측면 성장을 통해 성장하는 것을 관찰하였다. CL 분석을 통해 dark spot 밀도가 레퍼런스 샘플과 비교해 1.9×10^{8} cm^{-2} 에서 1.4×10^{8} cm^{-2} 로 감소한 것을 확인하였으며 이를 통해 CES 이용한 성장이 관통전위 밀도를 감소 시킴을 입증하였다. 또한 중공 구조물의 도입이 GaN 에피층의 응력 및 기판 휨을 약 30 % 감소시킨다는 사실도 확인하였다. 더불어 CES 위 제작한 LED 소자를 웨이퍼 상태로 광 출력을 측정한 결과 그 값이 레퍼런스 대비 약 2.2 배

증가한 것을 확인하였다. 이는 에피층과 기판 사이 계면에 도입된 중공 구조물이 광추출효율을 크게 향상시킨 다는 것을 보여준다.

추가적으로 패턴 위에서의 GaN 성장을 억제하기 위해 부분 결정화시킨 CES 위 GaN 박막을 성장시키는 방법을 제시하였다. 비정질 알루미나 구조물의 고상에피택시를 제어하여 패턴 사이 영역은 단결정 알파상으로 결정화 시키고 알루미나 중공껍질은 나노결정질 감마상으로 남겨두었다. 나노결정질 알루미나 중공껍질 위 나노결정질의 GaN island 들이 성장되었지만 이들의 매우 느린 성장속도로 인해 패턴 사이 영역에서 성장하는 c 면 GaN 의 측면성장을 방해하지 않아 패턴 위에서 GaN 박막이 합쳐지는 동안 추가적으로 관통전위가 생성되지 않는 것을 입증하였다. 그 결과 기존의 CES 위 제작한 GaN 쇼키다이오드 대비 누설전류가 열 배 이상 감소한 결과를 확인하였다.

주요어:

GaN, 고상에피택시, 알루미나, 사파이어기판, 중공, 감마상 알루미나 도메인, 유기 금속 화학 증착법, 발광다이오드, 광추출효율, 에피택셜 측면성장, 관통전위, 기판 휨

학번:

2010-22759

Publication list

Journal Papers:

1. **Jeonghwan Jang**, Daeyoung Moon, Hyo-Jeong Lee, Donghyun Lee, Daehan Choi, Dukkyu Bae, Hwankuk Yuh, Youngboo Moon, Yongjo Park, Euijoon Yoon, Incorporation of air-cavity into sapphire substrate and its effect on GaN growth and optical properties, Journal of Crystal Growth **430**, 41–45 (2015).

2. **Jeonghwan Jang**, Daeyoung Moon, Daehan Choi, Hye Jin Lim, Dukkyu Bae, Yongjo Park, and Euijoon Yoon, "Study on solid-phase epitaxy of cavity-shaped amorphous Al_2O_3 membrane structure on sapphire substrate", (In preparation).

3. **Jeonghwan Jang**, Seungmin Lee, Daeyoung Moon, Daehan Choi, Hye Jin Lim, Dukkyu Bae, Yongjo Park, and Euijoon Yoon, "Growth of GaN on nanocrystalline Al_2O_3 cavity patterned sapphire substrate for suppression of parasitic GaN on the pattern surface", (In preparation).

4. **Jeonghwan Jang**, Seung-Yong Lee, Hwanyeol Park, Yongjo Park, and Euijoon Yoon, "Investigation on gamma alumina layer formed by solid-phase epitaxy of amorphous alumina layer on c-plane sapphire", (In preparation).

5. Donghyun Lee, Jong Won Lee, **Jeonghwan Jang**, In-Su Shin, Lu Jin, Jun

Hyuk Park, Jungsub Kim, Jinsub Lee,Hye-Seok Noh, Yong-Il Kim, Youngsoo Park, Gun-Do Lee, Yongjo Park, Jong Kyu Kim, and Euijoon Yoon, Improved performance of AlGaN-based deep ultraviolet light-emitting diodes with nano-patterned AlN/sapphire substrates, Appl. Phys. Lett. 110, 191103 (2017).

6. Yoon-Jong Moon, Daeyoung Moon, **Jeonghwan Jang**, Jin-Young Na, Jung-Hwan Song, Min-Kyo Seo, Sunghee Kim, Dukkyu Bae, Eun Hyun Park, Yongjo Park, Sun-Kyung Kim, and Euijoon Yoon, Microstructured Air Cavities as High-Index Contrast Substrates with Strong Diffraction for Light-Emitting Diodes, Nano Letters **16**, 3301-3308 (2016).
7. Daeyoung Moon, **Jeonghwan Jang**, Daehan Choi, In-Su Shin, Donghyun Lee, Dukkyu Bae, Yongjo Park, and Euijoon Yoon, An ultra-thin compliant sapphire membrane for the growth of less strained, less defective GaN, Journal of Crystal Growth **441**, 52-57 (2016).
8. Jonghak Kim, Heeje Woo, Kisu Joo, Sungwon Tae, Jinsub Park, Daeyoung Moon, Sung Hyun Park, **Jeonghwan Jang**, Yigil Cho, Jucheol Park, Hwankuk Yuh, Gun-Do Lee, In-Suk Choi, Yasushi Nanishi, Heung Nam Han, Kookheon Char & Euijoon Yoon, "**Less strained and more efficient GaN light-emitting diodes with embedded silica hollow nanospheres**", *Scientific Reports **3**,* 3201 (2013).
9. S. H. Park, J. Park, D.-J. You, K. Joo, D. Moon, **J. Jang**, D.-U. Kim, H. Chang, S. Moon, Y.-K. Song, G.-D. Lee, H. Jeon, J. Xu, Y. Nanishi, and E. Yoon, "**Improved emission efficiency of a-plane GaN light emitting diodes with silica nano-spheres integrated into a-plane GaN buffer**

layer", *Applied Physics Letter **100**,* 191116 (2012).

Conference presentations:

International conference

1. **Jeonghwan Jang**, Sung Hyun Park, Keun Wook Shin, Daeyoung Moon, Dong-Uk Kim, Hojun Chang, Gun-Do Lee, Heonsu Jeon, Jimmy Xu, Yasushi Nanishi, and Euijoon Yoon, "Evaluation of polarization property of a-plane GaN light emitting diodes by controlled integration of silica nano-sphere", The 16th International Conference on Metal Organic Vapor Phase Epitaxy (2012).

2. **Jeonghwan Jang**, Sung Hyun Park, Daeyoung Moon, Dong-Uk Kim, Hojun Chang, Gun-Do Lee, Heonsu Jeon, Jimmy Xu, Yasushi Nanishi, and Euijoon Yoon, "FDTD simulation of light extraction and polarization property of a-plane GaN light emitting diodes by controlled integration of silica nano-spheres", International Workshop on Nitride Semiconductors 2012 (2012).

3. **Jeonghwan Jang**, Jonghak Kim, Sung Hyun Park, Gundo Lee, Yasushi Nanishi, and Euijoon Yoon, "FDTD simulation for calculation of light extraction in GaN LED with silica hollow nanospheres", The 10th International Conference on Nitride Semiconductors (2013).
4. **Jeonghwan Jang**, Daeyoung Moon, Hyo-Jeong Lee, Donghyun Lee, Daehan Choi, Dukkyu Bae, Hwankuk Yuh, Youngboo Moon, Yongjo Park and Euijoon Yoon, "Growth of high quality and less strained GaN on cavity engineered sapphire substrate", The 7th Asia-Pacific Workshop on

Widegap Semiconductors (2015).

5. **Jeonghwan Jang**, Daeyoung Moon, Hyo-Jeong Lee, Donghyun Lee, Daehan Choi, Dukkyu Bae, Hwankuk Yuh, Youngboo Moon, Yongjo Park and Euijoon Yoon, "Cavity engineered sapphire substrate for less strained and more efficient GaN based LEDs", The 11th International Conference on Nitride Semiconductors (2015).
6. **Jeonghwan Jang**, Daeyoung Moon, Hyo-Jeong Lee, Donghyun Lee, Daehan Choi, Dukkyu Bae, Hwankuk Yuh, Youngboo Moon, Yongjo Park and Euijoon Yoon, "Incorporation of air-cavity patterns into sapphire substrate for less strained and more efficient GaN based LEDs", 14th International Union of Materials Research Societies-International Conference on Advanced Materials (2015).

7. **Jeonghwan Jang**, Daeyoung Moon, Daehan Choi, Hye Jin Lim, Dukkyu Bae, Yongjo Park, and Euijoon Yoon, "Growth of high quality GaN layer on partially crystallized alumina cavity pattern on sapphire substrate", The 20th International Vacuum. Congress (2016).
8. **Jeonghwan Jang**, Daeyoung Moon, Daehan Choi, Hye Jin Lim, Dukkyu Bae, Yongjo Park, and Euijoon Yoon, Study on Solid Phase Epitaxy of 3-dimensional Al_2O_3 Membrane Structure on Sapphire Substrate, International Workshop on Nitride Semiconductors 2016 (2016).

Plus 20 other co-authors presentations.

Domestic conference

1. **장정환**, 문대영, 최대한, 임혜진, 박용조, 윤의준, “고효율 LED 용 기판 제작을 위한 3-D Al2O3 멤브레인의 solid-phase epitaxy 연구”, 2016년도 한국재료학회 춘계학술대회 (2016)

2. **장정환**, 이승민, 최대한, 임혜진, 박용조, 윤의준, “Reduction of threading dislocations in GaN layer using partially crystallized cavity engineered sapphire substrate”, 2016년도 한국재료학회 추계학술대회 (2016)

3. **장정환**, 문대영, 김기웅, 박용조, 윤의준, “Incorporation of air-cavity array into GaN layer for high efficient GaN-based LEDs”, 2016 한국결정성장학회 춘계학술대회 및 산업용 단결정/웨이퍼 기술 심층 심포지엄 (2016)

4. **장정환**, 문대영, 이동현, 최대한, 배덕규, 박용조, 윤의준, “Cavity engineered sapphire substrate for more efficient and less strained GaN based LEDs”, 제 2회 LED반도체조명학회/한국광전자학회 학술대회 (2016)

5. **장정환**, 문대영, 이효정, 이동현, 배덕규, 여환국, 문영부, 박용조,

윤의준, “Cavity 패턴 처리된 기판을 이용한 LED의 내부 응력 감소 및 효율 증가”, 제11회 LED 반도체조명학회 (2015)

6. **장정환**, “Cavity 패턴 처리된 sapphire substrate를 이용한 고효율 LED 제작”, 2014년도 한국광전자학회 제4회 정기학술대회 (2014)

7. **장정환**, 박성현, 이건도, 윤의준, “FDTD 시뮬레이션을 통한 내부에 silica nano-sphere가 삽입된 LED의 광 추출 효율증가 계산, 제 8회 LED 반도체 조명학회 학술대회 (2013)

8. **장정환**, 박성현, Yasushi Nanishi, 윤의준, “FDTD simulation을 이용한 실리카 나노 구체가 포함된 LED의 광 추출 효율 계산”, 제 7회 LED 반도체 조명학회 학술대회 (2013)

9. **장정환**, 박성현, Yasushi Nanishi, 윤의준, “실리카 나노 구체가 포함된 비극성 LED의 광 특성 향상”, 2012년도 제2회 한국광전자학회 학술대회 (2012)

Plus 11 other co-authors presentations.

Patents:

1. 윤의준, 문대영, **장정환**, 박용조, 배덕규, “반도체 적층 구조, 이를 이용한 질화물 반도체층 분리방법 및 장치 (Semiconductor thin film structure, method and apparatus for separating nitride semiconductor using the same)”, 대한민국, 출원 번호: 10-2014-0088503.

2. 김정섭, 이동현, 이진섭, 황경욱, 신인수, 윤의준, 이건도, **장정환**, 반도체 자외선 발광소자, 대한민국, 출원 번호: 10-2015-0116301.

3. 김정섭, 이동현, 이진섭, 황경욱, 신인수, 윤의준, 이건도, **장정환**, “Semiconductor Ultraviolet Light Emitting Diode”, 출원 번호: 15147039)